

Equations of state for hot neutron stars

Adriana R. Raduta · Flavia Nacu · Micaela Oertel

Received: date / Accepted: date

Abstract We review the equation of state (EoS) models covering a large range of temperatures, baryon number densities and electron fractions presently available on the COMPOSE database. These models are intended to be directly usable within numerical simulations of core-collapse supernovae, binary neutron star mergers and proto-neutron star evolution. We discuss their compliance with existing constraints from astrophysical observations and nuclear data. For a selection of purely nucleonic models in reasonable agreement with the above constraints, after discussing the properties of cold matter, we review thermal properties for thermodynamic conditions relevant for core-collapse supernovae and binary neutron star mergers. We find that the latter are strongly influenced by the density dependence of the nucleon effective mass. The selected bunch of models is used to investigate the EoS dependence of hot star properties, where entropy per baryon and electron fraction profiles are inspired from proto-neutron star evolution. The Γ -law analytical thermal EoS used in many simulations is found not to describe well these thermal properties of the EoS. However, it may offer a fair description of the structure of hot stars whenever thermal effects on the baryonic part are small, as shown here for proto-neutron stars starting from several seconds after bounce.

Keywords equation of state · dense matter · hot stellar environments · neutron stars · core-collapse supernovae · binary neutron star mergers

1 Introduction

The composition and structural properties of cold, mature neutron stars (NS) in weak β -equilibrium depend on a one-parameter equation of state (EoS) that relates the pressure to the energy density. On the contrary, dynamics of core-collapse supernovae (CCSN), evolution of proto-neutron stars (PNS), formation of stellar black holes (BH), and the post-merger phase of binary neutron star mergers (BNS) require an EoS depending on three thermodynamic parameters, typically chosen as temperature T , baryon number density n_B , and electron fraction Y_e . These need to cover wide domains: $10^{-14} \text{ fm}^{-3} \leq n_B \leq 1.5 \text{ fm}^{-3}$, $0 \leq Y_e = n_e/n_B \leq 0.6$ and $0 \leq T \leq 100 \text{ MeV}$ [1, 2, 3, 4, 5, 6, 7, 8, 9, 10, 11, 12, 13]. Since a long time, numerous numerical studies of these different phenomena show a considerable sensitivity to the EoS, see e.g. [1, 14, 15, 16, 17, 18].

In the last decades the EoS of cold NS has been intensively studied and constrained by experimental nuclear physics data, astrophysical data from radio/X-ray pulsars, gravitational wave events, and *ab initio* calculations of (neutron) matter. The different data are complementary in the sense that the conditions of each measurement imply that constraints on the EoS can be obtained within a particular density and isospin asymmetry domain. In particular, nuclear experiments are naturally performed for matter with densities below saturation density $n_{sat} \approx 0.16 \text{ fm}^{-3} \approx 2 \cdot 10^{14} \text{ g/cm}^3$ and for a nearly equal number of protons and neutrons and *ab initio* calculations are the most reliable for low density ($\lesssim 1 - 2n_{sat}$) pure neutron matter.

Adriana R. Raduta
National Institute for Physics and Nuclear Engineering (IFIN-HH),
RO-077125 Bucharest, Romania
E-mail: araduta@nipne.ro

Flavia Nacu
National Institute for Physics and Nuclear Engineering (IFIN-HH),
RO-077125 Bucharest, Romania
E-mail: flavia.nacu@nipne.ro

Micaela Oertel
LUTH, Observatoire de Paris, Université PSL, CNRS, Université de
Paris, 92190 Meudon, France
E-mail: micaela.oertel@obspm.fr

On the astrophysical side, NS mass measurements provide lower limits on the maximum gravitational mass of stable configurations M_G^{max} and, thus, constrain the high density range of β equilibrated EoS. Recent observations of pulsars with precisely determined masses around $2 M_\odot$ correspond to PSR J1614-2230 ($M = 1.908 \pm 0.016 M_\odot$, 68.3% credible interval) [19, 20]; PSR J0348+0432 ($M = 2.01 \pm 0.04 M_\odot$, 68.3% credible interval) [21]; MSP J0740+6620 ($M = 2.14^{+0.20}_{-0.18} M_\odot$ with 95.4% confidence level [22] and $M = 2.08^{+0.07}_{-0.07} M_\odot$ with 68.3% confidence level [23]). Even more massive NS have been identified in so-called "spider" systems, *e.g.* PSR J1810+1744 ($M = 2.13 \pm 0.04 M_\odot$ with 68% confidence level [24]) but, in contrast to the above mentioned mass determinations, these mass estimations depend on the companion heating model. These measurements have triggered a large number of studies on the appearance of non-nucleonic degrees of freedom at high densities. In particular, hyperons [25, 26, 27, 28, 29, 30, 31, 32, 33, 34], the lowest spin-3/2 baryonic multiplet [35, 36, 37, 38, 39, 40], meson condensates [41, 42] and a potential phase transition to quark-matter [43, 44, 45, 46, 47, 48, 49, 50] have been considered. All these works indicate that in contrast to the first expectations, maximum NS masses of $\approx 2 M_\odot$ do not exclude these non-nucleonic degrees of freedom to appear in the most massive neutron stars.

Gravitational waves detected from the late inspiral of the binary neutron stars merger event GW170817 [51, 52] have allowed to determine a combined tidal deformability of the two NSs [53]. Due to the estimated masses in GW170817, $1.36 M_\odot \leq M_1 \leq 1.60 M_\odot$ and $1.16 M_\odot \leq M_2 \leq 1.36 M_\odot$, this measurement constrains the intermediate density domain of the EoS and, implicitly, the radii of NSs in this mass range.

The NICER mission has recently provided two simultaneous mass and radius measurements for PSR J0030+0451 with $R(1.44^{+0.15}_{-0.14} M_\odot) = 13.02^{+1.24}_{-1.06}$ km [54] and $R(1.34^{+0.15}_{-0.16} M_\odot) = 12.71^{+1.14}_{-1.19}$ km (68.3%) [55] and J0740+6620 with $R(2.08 \pm 0.07 M_\odot) = 13.7^{+2.6}_{-1.5}$ km (68%) [56] and $R(2.072^{+0.067}_{-0.066} M_\odot) = 12.39^{+1.30}_{-0.98}$ km [57]. Combining the NICER results with the limits on the NS maximum mass as well as the tidal deformability from GW170817 [53] leads to constraints on the β -equilibrated EoS for densities in the range $1.5 n_{sat} \lesssim n_B \lesssim 3 n_{sat}$ [56, 58] and which can be translated into limits for NS radii [56].

Altogether, these recent developments have allowed to considerably narrow down the parameter space for cold β -equilibrated EoS. The situation is more complicated for the finite-temperature EoS potentially out of weak equilibrium where no firm constraint exists so far. The different analysis performed of GW170817 and its electromagnetic counterpart (GRB170817A and AT2017gfo) have formidably confirmed that future multimessenger observations –combining gravitational wave detection with electromagnetic and neutrino signals– from binary neutron star mergers and core-

collapse supernovae with the subsequent PNS evolution have the potential to sample this complementary domains of the dense matter EoS. Among others, a combined analysis of the GW and electromagnetic data for this particular event has been used by several authors to deduce both a lower [17] and an upper bound on M_G^{max} [59, 60, 61, 62]. In [63] the importance of thermal effects on the EoS in this context is demonstrated, relaxing considerably the upper bound.

In contrast to the cold NS EoS, where systematic studies allow to relate data to single nuclear matter parameters, see *e.g.* [32, 64, 65, 66], the dynamic environment implying an interplay of many different factors, as well as the thermal and compositional effects in the EoS render this task difficult for the so-called "general purpose" EoS depending on three parameters. In this context, theoretical developments [67, 68] as well as numerical simulations [69, 70, 71, 72, 73] indicate that properties of hot matter and the corresponding dynamical evolution of the related astrophysical phenomena are very sensitive to the value of the nucleon effective mass due to its predominant role in determining the kinetic energy and thus the strength of thermal effects.

The main motivation of this work is to try to better understand the finite temperature EoS. To that end we perform a comparative study of the general purpose EoS available on COMPOSE, focussing on purely nucleonic ones. The online service COMPOSE [74] provides EoS data in tabular form and among others most of the currently publicly available general purpose EoS. These are delivered as 3D tables as function of n_B , T and Y_e . Entries include primary thermodynamic state variables (energy density, free energy density, chemical potentials, pressure and entropy) and optionally microscopic quantities (Landau effective masses, Dirac effective masses, single particle potentials) as well as relative abundances of different species. Typical ranges of values for which this information is offered are $10^{-15} \leq n_B \leq 1 - 10 \text{ fm}^{-3}$, $0.1 \leq T \leq 100 \text{ MeV}$ and $0.01 \leq Y_e \leq 0.6$. The compose software allows to interpolate or extract data for specific thermodynamic conditions, including constant entropy per baryon and neutrino-less β -equilibrium and to obtain various thermodynamic coefficients via numerical differentiation (specific heats at constant volume and at constant pressure, adiabatic index, adiabatic compressibility, thermal compressibility, tension coefficient at constant volume, speed of sound). In addition to general purpose tables, EoS for cold β -equilibrated NS, symmetric nuclear matter (SNM) and pure neutron matter (PNM) are available, too.

We start by reviewing in Sec. 2 the ensemble of the general purpose EoS models presently available as well as their compliance with various constraints from nuclear physics and NS observations. We then further analyze the behavior of a selection of models. The resulting properties of cold matter are discussed in Sec. 3, followed by a discussion of hot matter properties with various degrees of isospin asym-

metry and different temperatures ($5 \leq T \leq 50$ MeV) in Sec. 4. In many numerical approximations, thermal effects are approximately included by adding to the cold EoS thermal contributions in the form of a Γ -law [75, 76, 77, 78]. Hot matter properties obtained from the full finite-temperature EoS will be compared with the Γ -law ones. The composition and a number of selected thermodynamic quantities of hot stellar matter with subsaturation densities are investigated in Sec. 5 with special focus on the model dependence of the results; the temperature-dependence of the symmetry energy is considered in Sec. 6; the EoS dependence of PNS properties and the performance of the Γ -law approximation for thermal effects are studied in Sec. 7. Conclusions are drawn in Sec. 8.

Throughout this paper, unless otherwise stated, we use natural units $k_B = c = \hbar = 1$. The value of the neutron rest mass in vacuum is used to convert number densities to rest-mass densities.

2 General purpose EoS models on COMPOSE

In this section we provide an overview¹ of models for which general purpose EoS tables are available on the COMPOSE site² [74], before discussing the thermal properties for some selected models in more detail. General purpose tables cover a large range of different baryon number densities n_B , temperatures T , and electron fractions Y_e with the idea to be applicable to CCSN and BNS merger simulations. To that end, in general the contribution of charged leptons (electrons and positrons) as well as photons are included as ideal Fermi or Bose gases, respectively. The available models differ only for the hadronic part, there differences arise from the treatment of inhomogeneous matter containing nuclear clusters, the interactions between nucleons and potentially other baryons, and the particle content considered at suprasaturation densities, *i.e.* which non-nucleonic degrees of freedom (hyperons, pions, kaons, quarks, ...) are included.

For reviews about the underlying nuclear physics, see e.g. [79, 80], here we will only briefly remind the main characteristics of the models on COMPOSE. The standard format for the name of a particular EoS table takes the form XXX(YYY). XXX thereby indicates the initials of the authors in the original publication(s) proposing the corresponding model. In the case of the general purpose tables this allows to identify, for models with nucleonic particle degrees of freedom, the treatment of inhomogeneous matter, see Sec. 2.2. YYY represents the name of the interaction, see Sec. 2.1, and accounts for both nucleonic and exotic sectors. In tables 1, 2 and 3 we list all EoS tables with in-

formation on treatment of inhomogeneous matter, baryonic interactions and particle content.

2.1 Effective interactions between baryons

2.1.1 Energy density functionals

Most available tables employ phenomenological approaches and use effective interactions between nucleons, motivated in terms of energy density functional theory (DFT). The parameters of the interaction are in general fitted to different properties of selected nuclei and nuclear matter properties. Already on the mean-field level these interactions result in a rather precise description of nuclei and nuclear matter. An extrapolation to the highest densities and/or to very neutron rich matter or neutron rich nuclei, *i.e.* far away from the domain where the interaction actually has been fitted, should be regarded with some caution. Nevertheless, due to their technical simplicity, these interactions are the most widely used to construct general purpose EoS tables. Different classes exist:

(Generalized) Skyrme effective interactions: These are based on non-relativistic density functionals with a large variety of different parameter sets. The pool of considered data as well as the relative weight between data that sample isoscalar and isovector channels explain the large number of existing interactions and their wide range of behaviors. For a review, see e.g. Ref. [81]. For neutron star applications it is interesting to note that some parameterisations consider *ab initio* calculations of neutron matter as data for adjusting the parameters, e.g. the SLy4 parameterisation [82].

Covariant density-functional models (CDFT): These are based on (special) relativistic functionals, usually written in terms of a Lagrangian density, where the different interaction channels for the nucleons are often labeled by the meson with the corresponding quantum numbers. In general, baryons are considered to interact in the scalar-isoscalar (σ), the vector-isoscalar (ω), and the vector-isovector (ρ) channel, sometimes a vector-isoscalar (δ) channel is included and, if hyperons are considered, different channels coupling baryons with nonzero strangeness. Several functionals assume non-linear potentials depending on the mean fields; in other models the interaction parameters are assumed density dependent. For a review, see e.g. Ref. [83].

The SU(3) Chiral Mean Field (CMF) model [84, 85] falls in this category, too. However, the structure of the interaction is taken from a non-linear realization of the sigma model incorporating chiral symmetry. In particular, at high densities and/or temperatures, chiral symmetry is restored, which can be seen in a reduction of the effective baryon masses. The model is in good agreement with nuclear physics data and at low densities and/or temperatures, the nuclear liquid-gas first-order phase transition is reproduced.

¹ as of August, 30, 2021

² <https://compose.obspm.fr/>

2.1.2 *Ab initio* calculations

Due to the computational expenses needed to determine the dense matter EoS starting from the basic few body interactions between baryons, no tables from genuinely microscopic calculations exist. However, tables with effective interactions fitted to the results of microscopic calculations wherever they exist, are available. One example is the APR interaction [86], which is a fit to the variational calculations by [87]. The latter employ realistic two-body (Argonne V18 [88]) and the three-body (Urbana UIX [89,90]) nuclear potentials derived from fits of scattering data and that were shown to reproduce a series of atomic nuclei properties. The APR interaction includes a phenomenological extension to correctly describe the effect of three-body forces in dense matter. Due to the three-nucleon interaction, energies of both symmetric nuclear matter (SNM) and pure neutron matter (PNM) manifest a discontinuity in slope such that different analytic forms are required to fit the low and high density domains [86]. This discontinuity is interpreted as a transition to a spin-isospin ordered phase, *i.e.* a neutral pion condensate, and the density where it occurs depends on the isospin asymmetry of the system. The extension to finite temperatures of the APR EoS in [67] was performed assuming that the transition density does not depend on temperature. Note nevertheless that the borders of the phase coexistence region manifest a slight temperature-dependence.

The calculation of Ref. [91] (“KOST”) relies on the same basic two-body (Argonne V18 [88]) and the three-body (Urbana UIX [89,90]) nuclear potentials as APR [86]. Differences to the APR EoS arise from the simplified two-body cluster variational approach and the fact that relativistic boost corrections are not included in [91]. They result in slightly different energies of symmetric nuclear matter and neutron matter at zero temperature. More importantly, at variance with APR, the KOST EoS does not manifest any discontinuity in the energy and, thus, no transition to a spin-isospin ordered phase at high densities. A detailed comparison between these two microscopic EoS was performed in [67]. The description of homogeneous matter in Ref. [92] (“KOST2”) is based on the KOST EoS, additionally corrected for spurious deuteron-like correlations due to the two-body cluster approximation which were shown to introduce nonzero contributions to the energy per nucleon in the low density limit.

2.2 Treatment of inhomogeneous matter

At low densities and temperatures, matter becomes clustered. For the considered conditions, matter is in equilibrium with respect to strong and electromagnetic interaction, determining the abundances of the different nuclei. However, since in particular for the thermodynamic properties of the EoS, the detailed distribution of nuclei has not a large

influence [93], many models approximate the full nuclear distribution by one light (^4He)-nucleus and a representative heavy nucleus within the so-called “single nucleus approximation” (SNA). More recently, among others due to the importance of the detailed distribution for weak interaction rates [94,95,96], extended “nuclear statistical equilibrium” (NSE) models have been developed, including an interaction between the nuclear clusters and the surrounding gas of unbound nucleons, too. Models not only differ by the considered pool of nuclei, but by the considered nuclear masses, the treatment of thermally excited states, the treatment of the transition to homogeneous matter, and the interaction with nucleons, too. Let us now give a brief overview:

2.2.1 SNA models

The *Lattimer and Swesty (LS) model* [97] is the first general purpose EoS which has been made publicly available for use in numerical simulations. For each T, n_B, Y_e the equilibrium configuration is determined by minimizing the total Helmholtz free energy, considering one representative heavy nucleus, α -particles and unbound nucleons. The unique heavy nucleus is treated within the finite-temperature compressible liquid-drop model, α -particles are considered to form an ideal Boltzmann gas and unbound nucleons interact via a Skyrme like momentum independent interaction. The energy functional accounts for shape-dependent surface, Coulomb and translational energy corrections. An excluded volume correction mimics interactions between unbound nucleons, α -particles and the heavy nucleus. The transition from inhomogeneous to homogeneous nuclear matter is performed by a Maxwell construction.

Later on, the model has been extended to very low densities within a noninteracting NSE approach [98] and to include the contribution of Λ -hyperons at high densities, see [98,99].

The SNA models by *Schneider, Roberts and Ott (SRO)* [100, 101] employ essentially the approach by Lattimer & Swesty for inhomogeneous matter. The two main differences are that they consider a variety of Skyrme interactions between unbound nucleons which offer more flexibility, especially at high densities, and that the transition from inhomogeneous to homogeneous nuclear matter is simplified. It is performed at the density where the competing structures provide equal values for the free energy. This obviously implies that there is no phase coexistence region, at variance with the original LS model [97]. Technical improvements with respect to the original LS model include accurate values of α -particle binding energy, neutron and proton masses and treatment of kinetic translational energy. In Refs. [100,101] tables have been computed using a NSE treatment for inhomogeneous matter with 3335 different nuclei. Apart from the NRAPR

model, these are, however, not available on COMPOSE for the moment.

The *model* by *H. Shen* et al. [102, 103] represents the second “standard” general purpose EoS besides the LS [97] one since tables have been made publicly available more than twenty years ago. As LS, they rely on SNA and consider nucleons, α -particles and one heavy nucleus in the inhomogeneous phase. A Thomas-Fermi approximation with parameterized density distributions in spherical Wigner-Seitz cells is used for determining the thermodynamically favorable state by minimizing the free energy density with respect to the cell volume, central densities, spatial extensions and surface diffuseness of protons and neutrons in the nucleus as well as densities of unbound neutrons and protons. The surface energy term is determined by performing Thomas-Fermi calculations of finite nuclei so as to reproduce some gross features of atomic nuclei. Translational degrees of freedom of the unique nucleus are not considered. α -particles are considered to form an ideal Boltzmann gas. Excluded volume corrections for the α -particles, the nucleon gas and the heavy nucleus are implemented. The transition from inhomogeneous to homogeneous nuclear matter is realized by minimizing the free energy density at a given density. In contrast to LS [97], they employ a CDFT effective interaction for unbound nucleons. The original version uses the TM1 parameterisation [104], a more recent version (SNH(TM1e)) is based on TM1e [105, 106], allowing for a different symmetry energy. The TNTYST(KOST2) EoS [92] shares the same Thomas-Fermi theoretical framework for describing inhomogeneous matter but employs a microscopic interaction, KOST2 [91, 92]. This is coherently used for treating unbound nucleons in subsaturated matter, suprasaturation homogeneous matter and the unique heavy nucleus, whose density function is supplemented with a gradient term to account for surface effects.

The original STOS(TM1) model has been extended to include the contributions of hyperons and pions at high densities with different hyperonic interactions [107] or a transition to quark matter modeled with in the MIT bag model [108, 109, 110]. The transition from the hadronic to the quark phase is thereby obtained via a Gibbs construction.

2.2.2 Extended NSE models

In the *Furusawa* et al. *models* [111, 112, 113, 114] inhomogeneous matter is considered to be made of unbound nucleons and a wide distribution of light (here defined as nuclei with $Z \leq 5$) and heavy ($Z \geq 6$) nuclei. Heavy nuclei are considered up to $Z \leq 1000$ and $N \leq 1000$. The binding energies of light nuclei are computed by modifying the experimental data [115] with phenomenological terms accounting for Coulomb screening by the uniform electron gas, Pauli en-

ergy shift [116] by other baryons and, for ${}^2\text{H}$, ${}^3\text{H}$, ${}^3\text{He}$ and ${}^4\text{He}$, interactions with unbound nucleons [112].

Heavy nuclei are computed within the liquid drop approximation with various corrections taking into account dense matter effects: electron screening is implemented in the Coulomb term, and phenomenological temperature and density dependent corrections are added to shell and surface energies [113]. Translational energy of nuclei is calculated as in the ideal Boltzmann gas with a geometrical estimation of the free volume.

For unbound nucleons, the FYS(TM1) model uses CDFT with the TM1 parameterisation, and the FT(KOST2) uses the microscopic variational calculations from Refs. [92].

The *models* by *G. Shen* et al. [117, 118, 119, 120] consider a gas of neutrons, protons, α -particles, and thousands of nuclei with $A \geq 12$. At subnuclear densities nonideal gas behavior is incorporated via the virial expansion. At very low density, this description reduces to noninteracting nuclear statistical equilibrium, whereas at higher densities the results match smoothly a CDFT description of homogeneous matter. Tables with different parameterisations of the CDFT interaction exist: NL3 [121], FSUgold [122] and FSUgold2.1 [120].

The models by *Hempel and Schaffner-Bielich* rely on the extended NSE model developed in Ref. [123]. Inhomogeneous matter at low densities is considered to be made of a gas of unbound self-interacting nucleons and an ensemble of light and heavy nuclei. The gas of unbound nucleons is treated within the CDFT approach, as is also the case of homogeneous matter at high densities. The distribution of nuclei at subsaturation densities is treated within NSE and for the free energy density the Maxwell-Boltzmann expression of a classical ideal gas is used. For the nuclear masses different choices are considered that automatically define the pool of nuclei, for details see Table 3. Coulomb screening by the electron gas, which modifies the nuclear binding energy, is implemented in the Wigner-Seitz cell approximation. A phenomenological temperature dependent description of excited nuclear states is included. Interactions between nuclei and unbound nucleons are mimicked via the excluded volume correction. The transition from inhomogeneous to homogeneous matter is realized under the constraints of local charge neutrality and equal values of proton fraction for the two phases. Pressure equality is determined only in an approximative way: pressures are only compared at the density grid-points of the final EoS table. The two phases are then connected by a thermodynamic consistent interpolation. Tables with a dozen of different parameterisations for the CDFT interaction of unbound nucleons exist, see Table 3.

The original model has been extended to account for Λ -hyperons [124] or the full baryonic octet [125, 126] at high densities or a condensate of K^- -mesons [41]. A transition to

quark matter is constructed in the class of BBKF models [47, 127].

Typel models The generalized relativistic density functional (GRDF) model was developed in Ref. [116]. At sub-saturation densities it accounts for a wide collection of light and heavy nuclei and effective two-nucleon states in the continuum with medium-dependent energies. At variance with other NSE models, where the transition to homogeneous matter takes place because of the excluded volume, in GRDF this transition occurs because nuclei dissolve in the surrounding gas of unbound nucleons. This process is realized via a density and temperature dependent shift of atomic masses accounting for the Pauli principle. Its parametrized form is obtained by fits to predictions from microscopic quantum statistical calculations [128]. GRDF1 and GRDF2 differ in the parametrization of the mass shifts of heavy nuclei as well as the values of the employed nuclear masses. For the level density, temperature dependent expressions are considered. The parametrized form of the mass shift is correlated with the density where the dissociation of massive nuclei occurs; in GRDF1 (GRDF2) this happens at $n_{sat}/3$ ($n_{sat}/2$). Both GRDF1 and GRDF2 employ the DD2 [116] parameterisation for the interaction of unbound nucleons. For more details, see Ref. [129].

The extended NSE model of *Gulminelli and Raduta* [130, 131] takes into account a large set of heavy and light nuclei, including $^2, \dots, ^6\text{H}$, $^3, \dots, ^{10}\text{He}$, $^3, \dots, ^{13}\text{Li}$, $^7, \dots, ^{18}\text{Be}$. At variance with other NSE models, this model also accounts for nuclei beyond drip lines. Their nuclear binding energies are described according to LDM(SLy4) [132] modified in two respects. First, a phenomenological pairing term is added. Then, two correction terms are included such as to smoothly match, for each isotopic chain, the liquid-drop predictions with the limiting values of the DZ10 [133] mass model, employed whenever experimental data are not available. The allowed mass range of clusters is $2 < A < 300$. The full list of low-lying resonances for nuclei with $4 \leq A \leq 10$ has been considered. For the level density a realistic expression fitted on experimental data is used. Unbound nucleons are modeled with the SLy4 Skyrme interaction [82]. Excluded volume effects between nuclear clusters and unbound nucleons are implemented via energy shifts of clusters binding energies.

In order to describe the transition from inhomogeneous to homogeneous matter, for fixed values of Y_q and T the clusterized phase is computed within the NSE approximation up to a maximum density where the NSE procedure converges, typically $4 \cdot 10^{-2} - 9 \cdot 10^{-2} \text{ fm}^{-3}$. Homogeneous matter is supposed to appear, independently of temperature and proton fraction, at $n_t = 10^{-1} \text{ fm}^{-3}$. For intermediate values of density, chemical composition and thermodynamic observables are computed by linear interpolation between the boundary values.

3 EoS of cold matter

Before addressing thermal effects, let us discuss some properties of the different EoS models in cold matter. Actually, most of the tables do not have a zero temperature entry, but the lowest available temperature is in general $T = 0.1 \text{ MeV}$. Except for very low densities $n_B \lesssim 10^{-9} \text{ fm}^{-3}$, the EoS at this low temperature is almost identical to the zero temperature one since the other energies in the system are much higher than T and in particular the chemical potentials $\mu_i \gg T$.

Table 4 summarizes nuclear matter parameters obtained employing the different interactions. These parameters enter a Taylor expansion of the energy per baryon of homogeneous nuclear matter in terms of baryon number density and isospin, taken around saturation density and isospin symmetry (*i.e.* same number of protons and neutrons). Mathematically this expansion is expressed with the variables $\delta = (n_n - n_p)/n_B = 1 - 2Y_p$, where $Y_p = n_p/n_B$ denotes the proton fraction, and $\chi = (n_B - n_{sat})/3n_{sat}$, respectively. The first step in this approach consists in expressing the energy per nucleon at arbitrary values of density n_B and isospin asymmetry δ as a sum between an isoscalar term and an isovector term

$$E(n_B, \delta)/A = E_0(n_B, 0) + \delta^2 E_{sym}(n_B, 0), \quad (1)$$

which implies a parabolic approximation for the isospin dependence. The first term in Eq. (1) represents the energy per baryon of symmetric matter while the second represents the symmetry energy. Note that other works in the literature [157, 158] account for higher order terms in isospin asymmetry. In this case, the symmetry energy is defined as the lowest order coefficient in the expansion of $E(n_B, \delta)/A$ in powers of δ ,

$$E_{sym}(n_B, 0) = \frac{1}{2} \frac{\partial^2 (E/A)}{\partial \delta^2} \Big|_{n_B, \delta=0}. \quad (2)$$

In turn the isoscalar and isovector terms in Eq. (1) are expanded in terms of baryon number density as

$$E_0(n_B, 0) = E_{sat}(n_{sat}, 0) + \frac{1}{2!} K_{sat}(n_{sat}, 0) \chi^2 + \frac{1}{3!} Q_{sat}(n_{sat}, 0) \chi^3 + \mathcal{O}(\chi^4), \quad (3)$$

and, respectively,

$$E_{sym}(n_B, 0) = J_{sym}(n_{sat}, 0) + L_{sym}(n_{sat}, 0) \chi + \frac{1}{2!} K_{sym}(n_{sat}, 0) \chi^2 + \mathcal{O}(\chi^3). \quad (4)$$

We note that the explanation of odd terms missing in the development of $E(n_B, \delta)/A$ in powers of δ resides in the assumed QCD isospin invariance, which is an approximation, and the fact that Coulomb interaction is disregarded.

Table 1 List of general purpose EoS tables based on SNA, available on COMPOSE. For each EoS model we provide information on: nuclear effective interaction; low density extension by NSE; considered degrees of freedom. Also given are the maximum mass of cold β -equilibrated NS (M_G^{max}); radius of canonical $1.4M_\odot$ NS (R_{14}); radius of a $2.072M_\odot$ NS ($R_{2.072}$); limits of combined tidal deformability $\tilde{\Lambda} = 16 [(M_1 + 12M_2)M_1^4 A_1 + (M_2 + 12M_1)M_2^4 A_2] / 13(M_1 + M_2)^5$ corresponding to the GW170817 event with an estimated total mass $M_T = 2.73^{+0.04}_{-0.01}M_\odot$ and a mass ratio range $0.73 \leq q = M_2/M_1 \leq 1$. The last but one column specifies whether tables exist also for purely baryonic matter, in addition to those corresponding to the whole mixture. Present astrophysical constraints on EoS regard: i) the lower limit of maximum gravitational mass; ii) radii of canonical mass NS; iii) radii of a massive NS; iv) range for the tidal deformability obtained from the GW170817 event, see text for details. Models in tension with constraint i) $M \geq 2.01 - 0.04M_\odot$ [21] are marked in bold. Values outside the ranges ii) $11.80 \leq R(1.4M_\odot) \leq 13.10$ km [56], iii) $11.41 \text{ km} \leq R(2.072M_\odot) \leq 13.69$ km [57], iv) $110 \leq \tilde{\Lambda} \leq 800$ [53] are also marked in bold. For M_G^{max} and R_{14} provided are the values on COMPOSE or the original publications. $R_{2.072}$, $\tilde{\Lambda}(q=0.73)$ and $\tilde{\Lambda}(q=1)$ are calculated by using for the crust the EoS models by [134] and [135]. Other notations are: q stands for u, d, s quarks; Λ denotes the Λ -hyperon; Y generically denotes the Λ, Σ and Ξ hyperons; π stands for pions.

class/ model	low dens. extension	d.o.f exotica	M_G^{max} (M_\odot)	R_{14} (km)	$R_{2.072}$ (km)	$\tilde{\Lambda}$ q=0.73	$\tilde{\Lambda}$ q=1	baryonic tables	Ref.
<i>Lattimer and Swesty</i>									
LS(LS220)	n	-	2.06	12.7	-	664	596	-	[97]
no low dens.									
LS(LS220)	y	-	2.06	12.7	-	664	596	-	[97,98]
with low dens.									
GROM(LS220L)	n	Λ	1.91	12.4	-	576	498	-	[97,98]
no low dens.									
GROM(LS220L)	y	Λ	1.91	12.4	-	576	498	-	[97,98]
with low dens.									
<i>Schneider et al.</i>									
SRO(APR)	n	π condens.	2.16	11.3	10.9	299	272	-	[101]
SRO(NRAPR)	y	-	1.94	11.9	-	385	340	-	[100,101]
SRO(SLy4)	n	-	2.05	11.7	-	369	334	-	[100]
SRO(SkAPR)	n	-	1.97	12.0	-	535	490	-	[100]
SRO(LS220)	n	-	2.04	12.7	-	658	593	-	[100]
SRO(KDE0v1)	n	-	1.97	11.7	-	340	303	-	[100]
SRO(LNS)	n	-	1.72	11.0	-	235	196	-	[100]
<i>HShen et al.</i>									
STOS(TM1)	n	-	2.23	14.5	13.7	1376	1279	y	[102,103]
STOS(TM1L)	n	Λ	1.90	14.4	-	1366	1283	y	[102,103]
IOTSY(TM1Y-30)	n	Y	1.63	14.3	-	-	1258	-	[107]
IOTSY(TM1Y0)	n	Y	1.64	14.3	-	1361	1286	-	[107]
IOTSY(TM1Y30)	n	Y	1.64	14.3	-	1362	1286	-	[107]
IOTSY(TM1Y90)	n	Y	1.64	14.3	-	1362	1286	-	[107]
IOTSY(TM1Y-30pi)	n	Y, π	1.66	13.6	-	844	781	-	[107]
IOTSY(TM1Y0pi)	n	Y, π	1.66	13.6	-	858	778	-	[107]
IOTSY(TM1Y30pi)	n	Y, π	1.66	13.6	-	858	778	-	[107]
IOTSY(TM1Y90pi)	n	Y, π	1.66	13.6	-	858	778	-	[107]
SFHPST(TM1B139)	n	q	2.08	12.6	-	n.a.	n.a.	-	[102,103,108,109,110]
SFHPST(TM1B145)	n	q	2.01	13.0	-	n.a.	n.a.	-	[102,103,108,109,110]
SFHPST(TM1B155)	n	q	1.70	10.7	-	n.a.	n.a.	-	[102,103,108,109,110]
SFHPST(TM1B165)	n	q	1.51	9.1	-	n.a.	n.a.	-	[102,103,108,109,110]
SNSH(TM1e)	n	-	2.12	13.1	12.5	793	756	-	[105,106]
<i>Togashi et al.</i>									
TNTYST(KOST2)	n	-	2.21	11.5	11.1	358	332	y	[92]

Table 2 The same as in Table 1 for EoS models accounting only for homogeneous matter. In addition to $R_{2.072}$, $\tilde{\Lambda}(q=0.73)$ and $\tilde{\Lambda}(q=1)$ R_{14} is calculated here by using the NS crust models by [134] and [135]. The matching with the core EoS is performed at $n_{cc} = 0.07 \text{ fm}^{-3}$.

class / model	d.o.f exotica	M_G^{max} (M_\odot)	R_{14} (km)	$R_{2.072}$ (km)	$\tilde{\Lambda}$ q=0.73	$\tilde{\Lambda}$ q=1	baryonic tables	Ref.
<i>Dexheimer et al.</i>								
DNS(CMF)	Y, q	2.1	14.0	12.6	1114	1043	y	[136,85]

Table 3 The same as in Table 1 for EoS models based on NSE. Whenever more than one reference is provided for mass tables, these are used over complementary (A, Z) domains. The mass data are employed using the following hierarchy: experimental data > predictions of mass models (Finite Range Droplet Model (FRDM) [137], Duflo-Zuker (DZ) [133]) > estimations based on the liquid drop model (LDM). Other notations are: nm , np and pp stand for 1S_0 continuum correlations of the mentioned particles. * means that for MBB(DD2K) only tables corresponding to purely baryonic matter are available.

class / model	mass table	d.o.f exotica	M_G^{max} (M_\odot)	R_{14} (km)	$R_{2.072}$ (km)	$\tilde{\Lambda}$ q=0.73	$\tilde{\Lambda}$ q=1	baryonic tables	Ref.
<i>GShen et al.</i>									
SHO(FSU1)	[137]	-	1.75	12.8	-	1182	932	y	[120]
SHO(FSU2)	[137]	-	2.12	13.6	14.2	2604	2307	y	[120]
SHT(NL3)	[137]	-	2.78	14.9	14.9	1639	1555	y	[119]
<i>Furusawa et al.</i>									
FYSS(TM1)	LDM	-	2.22	14.4	13.7	1376	1279	y	[111, 112, 113]
FTNS(KOST2)	LDM	-	2.25	11.5	11.1	360	334	y	[111, 112, 113, 114]
<i>Hempel et al.</i>									
<i>Steiner et al.; Banik et al.</i>									
HS(NL3)	[138]	-	2.79	14.8	14.9	1571	1483	y	[123]
HS(TM1)	[139]	-	2.21	14.5	13.7	1351	1255	y	[123]
HS(TMA)	[139]	-	2.02	13.8	-	1128	1052	y	[123]
HS(DD2)	[140],[137]	-	2.42	13.1	13.1	799	758	y	[123]
HS(FSG)	[141]	-	1.74	12.6	-	539	439	y	[123]
HS(IUF)	[141]	-	1.95	12.7	-	608	570	y	[123]
BHB(DD2L)	[140], [137]	Λ	1.95	13.2	-	787	757	y	[123, 124]
BHB(DD2Lphi)	[140], [137]	Λ	2.10	13.2	12.2	790	757	y	[123, 124]
SFH(SFHo)	[140], [137]	-	2.06	11.9	-	401	366	y	[123, 142]
FOP(SFHoY)	[140],[137]	Y	1.99	11.9	-	401	366	y	[123, 142, 126]
SFH(SFHx)	[140],[137]	-	2.13	12.0	11.3	466	428	y	[123, 142]
OMHN(DD2Y)	[140],[137]	Y	2.03	13.2	-	787	756	-	[123, 125]
MBB(DD2K)	[140],[137]	K^-	2.19	13.2	-	n.a.	n.a.	*	[123, 41]
<i>Typel et al.</i>									
GRDFN_DD2									
PT(GRDF1_DD2)	[115], DZ10[133]	-	2.42	13.2	13.1	781	742	-	[129]
PT(GRDF2_DD2)	[143], DZ31[133]	-	2.42	13.2	13.2	663	636	-	[129]
<i>Bastian et al.</i>									
BBKF(DD2F-SF)1.1	[140], [137]	q	2.13	12.2	10.7	507	467	y	[47, 144, 127]
BBKF(DD2F-SF)1.2	[140], [137]	q	2.15	12.2	11.4	501	473	y	[47, 144, 127]
BBKF(DD2F-SF)1.3	[140], [137]	q	2.02	12.2	-	512	467	y	[47, 144, 127]
BBKF(DD2F-SF)1.4	[140], [137]	q	2.02	12.2	-	516	467	y	[47, 144, 127]
BBKF(DD2F-SF)1.5	[140], [137]	q	2.03	12.2	-	488	467	y	[47, 144, 127]
BBKF(DD2F-SF)1.6	[140], [137]	q	2.00	12.2	-	513	467	y	[47, 144, 127]
BBKF(DD2F-SF)1.7	[140], [137]	q	2.11	12.2	11.2	514	467	y	[47, 127]
BBKF(DD2-SF)1.8	[140], [137]	q	2.06	11.0	-	218	180	y	[47, 127]
BBKF(DD2-SF)1.9	[140], [137]	q	2.17	11.3	11.2	228	196	y	[47, 127]
<i>Gulminelli and Raduta</i>									
RG(SLy4)	[115], DZ10 [133], LDM(SLy4) [132]	-	2.07	11.9	-	369	334	-	[130, 131]

We also note that the approximation in Eq. (1) suggests a second definition for the symmetry energy, as the per-nucleon cost of converting SNM ($\delta = 0$) in PNM ($\delta = 1$)

$$E_{sym}(n_B) = (E/A)_{PNM}(n_B) - (E/A)_{SNM}(n_B). \quad (5)$$

It is obvious that the definitions in Eqs. (1) and (5) only agree if higher order terms in δ are small, thus typically close to saturation density [158].

The caption of Table 4 lists bounds for these nuclear matter parameters obtained from a variety of nuclear experiments.

In the following we analyze the predictions of the different models in the limiting cases of symmetric matter (SM) and neutron matter (NM). Only purely nucleonic models which comply with the constraints on M_G^{max} , L_{sym} and K_{sat} specified in the captions of Tables 1 and 4 are considered. These are LS220, SRO(APR), SRO(SLy4), SRO(SkAPR), SRO(KDE0v1), TNTYST, SHO(FSUgold2.1), HS(DD2), HS(IUF), SFHo. In order to enlarge slightly the pool of models for better comparison, we additionally include SRO(NRAPR), SFHx and SNSH(TM1e). The first one thereby slightly un-

Table 4 List of nucleonic effective interactions on which general purpose EoS tables on COMPOSE are built. For each interaction we list the properties of symmetric nuclear matter at saturation density (n_{sat}): energy per nucleon (E_{sat}); compression modulus (K_{sat}); skewness (Q_{sat}); symmetry energy (J_{sym}); slope (L_{sym}) and curvature (K_{sym}) of the symmetry energy; Landau effective mass of nucleons (m_{eff}). We list in addition the neutron-proton effective mass splitting in neutron matter at n_{sat} (Δm_{eff}). Presently accepted constraints are as follows: $E_{sat} = 15.8 \pm 0.3$ MeV [145]; $n_{sat} = 0.155 \pm 0.005$ fm $^{-3}$ [145]; $K_{sat} = 230 \pm 40$ MeV [146]; $E_{sym} = 31.7 \pm 3.2$ MeV [79]; $L_{sym} = 58.7 \pm 28.1$ MeV [79]. Note nevertheless that the model-dependence inherent to the analyses for obtaining these values explains that other favored domains have been obtained in other works; for L_{sym} see for instance [147, 148, 149]; for K_{sat} see [150], too.

int.	class	n_{sat} (fm $^{-3}$)	E_{sat} (MeV)	K_{sat} (MeV)	Q_{sat} (MeV)	J_{sym} (MeV)	L_{sym} (MeV)	K_{sym} (MeV)	Q_{sym} (MeV)	m_{eff} (m_n)	Δm_{eff} (m_n)	Ref.
LS220	Skymrme	0.155	-16.64	219.85	-410.80	28.61	73.81	-24.04	96.17	1.00	0.00	[97]
SLy4	Skymrme	0.159	-15.97	229.91	-363.11	32.00	45.94	-119.73	521.53	0.695	-0.184	[82]
KDE0v1	Skymrme	0.165	-16.88	227.53	-384.83	34.58	54.70	-127.12	484.44	0.744	-0.128	[151]
LNS	Skymrme	0.175	-15.96	210.76	-382.50	33.43	61.45	-127.35	302.52	0.826	0.228	[152]
NRAPR	Skymrme	0.161	-16.50	225.64	-362.51	32.78	59.64	-123.32	311.60	0.694	0.214	[153]
SkAPR	Skymrme	0.160	-16.00	266.0	-348.3	32.59	58.47	-102.63	420.02	0.698	0.211	[101]
FSUgold	CDFT	0.148	-16.28	229.54	-523.93	32.56	60.44	-51.40	425.72	0.668	0.089	[122]
FSUgold2.1	CDFT	0.148	-16.28	229.54	-523.93	32.60	60.50	n.a.	n.a.	0.668	0.089	[120]
NL3	CDFT	0.148	-16.24	271.53	202.91	37.40	118.53	100.88	181.31	0.659	0.090	[121]
TM1	CDFT	0.145	-16.26	281.16	-285.22	36.89	110.79	33.63	-66.54	0.689	0.085	[104]
TM1e	CDFT	0.145	-16.3	281	-285	31.38	40	3.57	n.a.	0.647	0.086	[154]
TMA	CDFT	0.147	-16.02	318.15	-572.12	30.66	90.14	10.75	-108.74	0.686	0.086	[155]
DD2	CDFT	0.149	-16.02	242.72	168.65	31.67	55.04	-93.23	598.14	0.626	0.097	[116]
DD2F	CDFT	0.149	-16.02	242.72	168.65	31.67	55.04	-93.23	598.14	0.626	0.097	[46]
IUF	CDFT	0.155	-16.40	231.33	-290.28	31.30	47.21	28.53	370.71	0.670	0.093	[156]
SFHo	CDFT	0.158	-16.19	245.4	-467.8	31.57	47.10	-205.5	n.a.	0.811	0.078	[142]
SFHx	CDFT	0.160	-16.16	238.8	-457.2	28.67	23.18	-40.00	n.a.	0.771	0.083	[142]
CMF	CDFT	0.15	-16.0	300	281	30	88	n.a.	n.a.	n.a.	n.a.	[84, 136]
KOST2	micro	0.160	-16.09	245	n.a.	30.0	35	n.a.	n.a.	n.a.	n.a.	[91, 92]
APR	micro	0.160	-16.00	266.0	-1054.2	32.59	58.47	-102.63	1217.0	0.698	0.211	[86]

derestimates M_G^{max} , the second L_{sym} and the last one slightly overestimates K_{sat} . All results reported for cold matter correspond to the lowest available temperature value, typically $T = 0.1$ MeV. Similarly, results reported as neutron matter correspond to the lowest available Y_q value, typically $Y_q = 0.01$, which should be very close to the pure neutron matter case.

3.1 Symmetric matter

The energy per nucleon of cold baryonic SM predicted by the models introduced above is illustrated in the top panels of fig. 1 as function of baryon number density. The contribution of the baryonic sector is obtained by subtracting from the values provided in the tables the respective contributions of leptons and photons as ideal gases. A residual effect of the electron gas nevertheless persists in the cluster binding energies which have been modified in order to account for Coulomb screening. One first notes that for $n_B \lesssim 2n_{sat}$ the predictions of the various models differ only slightly. There are two reasons for that.

First, because of the competing effects of Coulomb and surface energies which get minimized when matter is clustered or uniform, respectively, subsaturation matter possesses an inhomogeneous structure. This structure basically consists of a dense component with a low isospin asymmetry

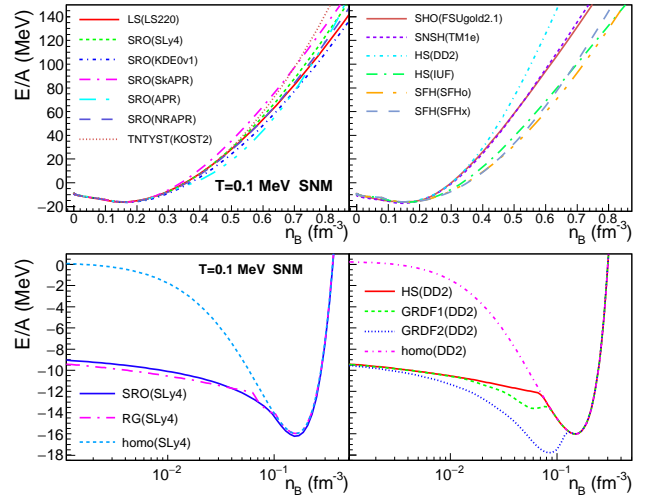


Fig. 1 Energy per nucleon as a function of baryon number density in cold baryonic SM. The bottom panels illustrate the low density behavior for a selection of models which employ the same nucleonic interaction but rely on different modelling of the inhomogeneous phase. The various EoS models are mentioned in the legend.

(a nuclear cluster) and a dilute component with high isospin asymmetry (unbound nucleons). All EoS models discussed in this work account for inhomogeneous structures at subsaturation densities. For symmetric matter, the main components contributing to the energetics in this density domain,

the nuclear clusters, are very well constrained by nuclear data. This explains, too, that $\lim_{n_B \rightarrow 0} E/A \rightarrow -8.5$ MeV (see the bottom panels). This last value corresponds to the maximum binding energy of atomic nuclei, well reproduced by all models. For comparison, the bottom panels show the behavior of homogeneous symmetric nuclear matter, too. It is clear that the energetics are very different, in particular $\lim_{n_B \rightarrow 0} E/A \rightarrow 0$ for homogeneous matter.

Although the predictions are rather similar, there remains some dependence on the treatment of inhomogeneous matter, see the bottom panels of fig. 1, where different EoS models are compared which use the same interaction for unbound nucleons, SLy4 on the left and DD2 on the right. Discrepancies between SRO(SLy4) vs. RG(SLy4) at subsaturation densities are attributable to the use of SNA in SRO(SLy4) and NSE in RG(SLy4). Discrepancies at $\approx n_{sat}$, which make SRO(SLy4) deviate from the values in Table 4, are probably artifacts of the procedure used to describe the transition from inhomogeneous to homogeneous matter [100]. Discrepancies between the GRDF-models and HS(DD2) are due to the fact that the former models implement a phenomenological shift of atomic masses that accounts for the antisymmetrization correlations between the free nucleons and the cluster single particle states and include nucleonic resonances. In addition, the transition from inhomogeneous to homogeneous matter is not yet implemented in a fully consistent way in the GRDF models which might explain the displaced minimum of E/A . An improved version is under construction and should soon be available [159]. Discrepancies between GRDF1(DD2) and GRF2(DD2) are, in turn, due to different parameterisations of the mass shifts.

Second, for higher densities, when nuclear clusters dissolve and matter becomes homogeneous, the energy per baryon of symmetric matter is still well constrained in the vicinity of saturation density by the low order nuclear matter parameters. Indeed, as can be seen from Table 4, the employed interactions show only a small spread for n_{sat} , E_{sat} , and K_{sat} and the differences in the poorly constrained higher order parameters only show up above roughly $2n_{sat}$. Discrepancies between SRO(APR) and TNTYST(KOST2), both employing the same two- and three-body potentials, are due to a slightly different many-body treatment resulting among others in the pion condensed state typical to APR which is absent in KOST2, see Sec. 2.1. For $n_B \gtrsim 0.32$ fm⁻³ KOST2 is stiffer than APR; it actually corresponds to the extension of the low density phase of APR beyond the density at which the transition to the pion condensate takes place. Incidentally, the two microscopic EoS models and those based on Skyrme-like interactions (top left panel), explore a more narrow range in E/A than the EoS models based on CDFT (top right panel).

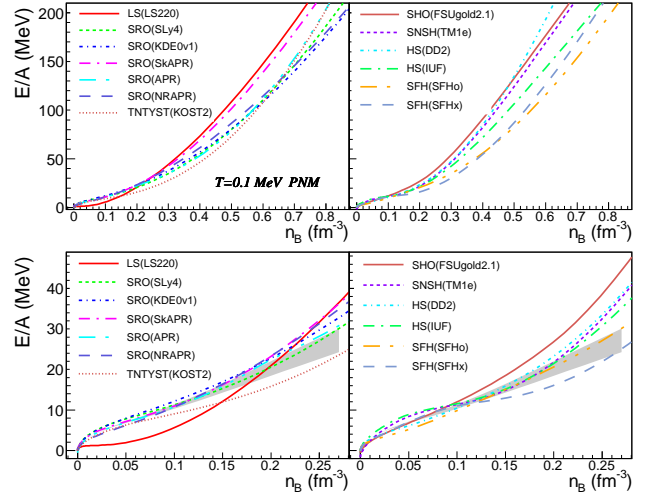


Fig. 2 Energy per neutron as a function of baryon number density in cold NM. The bottom panels represent a zoom in the low density region. The gray area thereby corresponds to predictions of many-body perturbation theory [160]. Various EoS models are considered as mentioned in the legend.

3.2 Neutron matter

The energy per neutron of cold NM predicted by various models introduced in Sec. 2 is illustrated in fig. 2 as function of baryon number density. The bottom panels focus on the low density region, where the model results are compared with predictions of many-body perturbation theory [160], based on a set of Hamiltonians with NN and 3N interactions from chiral EFT. At variance with what happens in matter with $Y_p \neq 0$, NM at subsaturation densities is homogeneous. The fact that the effective interactions in the isovector channel are only weakly constrained by nuclear data is reflected in a significant dispersion among the predictions of the different models over the whole density range. As for SM, this dispersion augments with increasing density. The available models based on Skyrme-like interactions span an uncertainty range comparable to that spun by the available models based on CDFT interactions. For $0.1 \lesssim n_B \lesssim 0.5$ fm⁻³ KOST2 provides lower values than APR, as one would expect based on lower values of J_{sym} and L_{sym} in the first model with respect to the latter; for higher densities, the two EoS models merge. This behavior has been previously commented on in [91, 67]. SLy4 and APR agree best with the microscopic calculations in [160].

3.3 Symmetry energy

The uncertainties in the isovector channel of the effective interactions show up in the symmetry energy, eq. (5), too. It is illustrated in fig. 3 as function of baryon number density for the models introduced in Sec. 2. The constraint at twice saturation density of nuclear matter, $E_{sym}(2n_{sat}) = 51 \pm 13$ MeV,

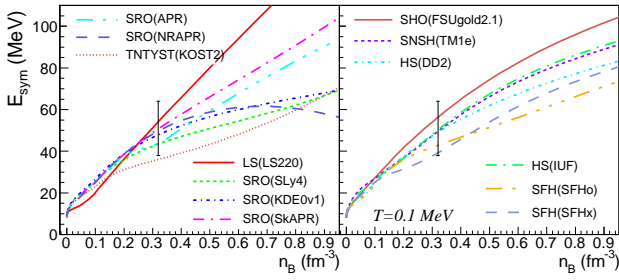


Fig. 3 Symmetry energy per nucleon, defined as $E_{sym}(n_B) = E_{NM}(n_B) - E_{SM}(n_B)$, as function of baryon number density at $T=0.1$ MeV. The vertical error bar corresponds to the constraint $E_{sym}(2n_{sat}) = 51 \pm 13$ MeV [148].

obtained in Ref. [148] from a compilation of recent analyses of NS and heavy ion collision data is shown, too. We note that, in contrast to what happens for uncharged uniform matter where $\lim_{n_B \rightarrow 0} E_{sym} \rightarrow 0$, clusterisation at subsaturation densities for symmetric matter translates into non-vanishing symmetry energies in the limit $n_B \rightarrow 0$ [116,161]. These dishomogenities at subsaturation densities break the approximately quadratic dependence of the energy per baryon on δ in eq. (3), too, such that eqs. (2) and (5) for determining the symmetry energy are no longer equivalent [161,162]. We also note that, similarly to what we have seen for SM, the occurrence at subsaturation densities of a dense phase with a density close to saturation, results in a reduced sensitivity to the underlying nucleon effective interaction of the symmetry energy [161].

Except SRO(NRAPR), which provides a non-monotonic $E_{sym}(n_B)$, the qualitative behavior of the other EoS models considered here is the same at suprasaturation densities, *i.e.* E_{sym} increases with n_B . Quantitative differences nevertheless exist: LS220 provides the stiffest evolution, while KDE0v1, KOST2, SLy4 and SFHo provide much softer ones. For $n_B \gtrsim 0.1 \text{ fm}^{-3}$ KOST2 and APR differ also in what regards the symmetry energy. At densities smaller than 0.2 fm^{-3} , which corresponds to the density where PNM computed by APR [86] exhibits the transition to pion condensed state, this is due to the differences between the predictions of the two variational calculations. At higher densities the discrepancies are more important and they are mainly due to the pion-condensed state in APR. All models are compatible with the constraint on $E_{sym}(2n_{sat})$ derived in Ref. [148]. KOST2 thereby predicts values slightly below the given range, but the deviation remains well compatible within errors.

The influence of the density dependence of the symmetry energy, expressed in terms of L_{sym} and K_{sym} , has been intensively discussed in the context of cold NSs. The most noteworthy correlations have been found between radii and tidal deformabilities of intermediate-mass NS [163,153,32,64,101,164,165,166] and L_{sym} . Since the proton fraction Y_p in β -equilibrated matter strongly depends on the symmetry energy, the density threshold for nucleonic dUrca pro-

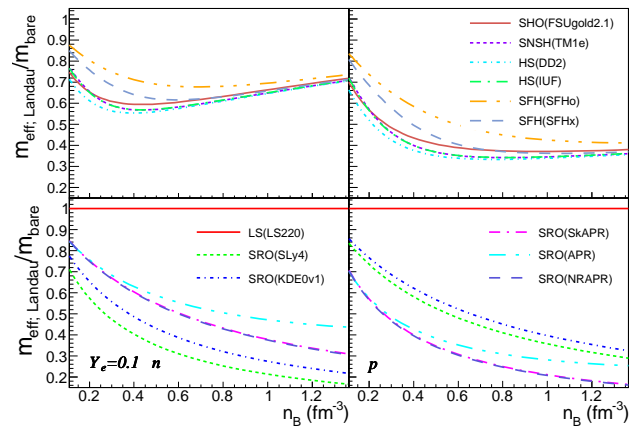


Fig. 4 Normalized neutron (left) and proton (right) Landau effective masses in cold asymmetric matter with $Y_e = 0.1$ as a function of baryon number density. Only considered are densities above the transition from inhomogeneous to homogeneous matter. Predictions of different models as mentioned in the legend.

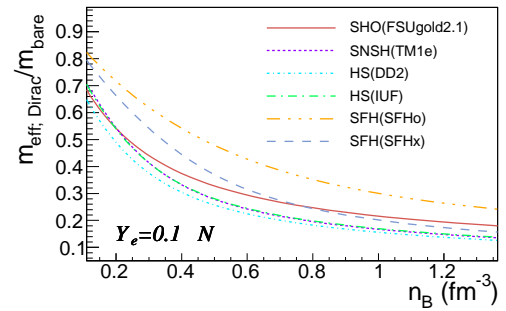


Fig. 5 Same as fig. 4 for the Dirac effective masses within the different CDFT models.

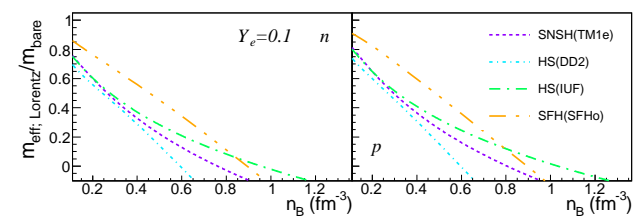


Fig. 6 Same as fig. 4 for the Lorentz effective masses within a selection of CDFT models.

cess [32], too, shows a strong correlation with L_{sym} . By controlling the radial density profiles of different species, L_{sym} and K_{sym} have been also shown to determine the magnitude and density dependence of the pairing gaps of fermions and, thus, modify the neutrino emission from compact star interiors [167]. This observation equally applies to purely nucleonic stars as hyperonic stars.

3.4 Effective masses in isospin asymmetric matter

An important ingredient of the nuclear EoS are the nucleonic effective masses. The concept of effective mass was introduced in order to describe the motion of particles in a momentum dependent potential similarly with the motion of quasi-particles in a momentum-independent potential. Later on it has been generalized to account for momentum and/or energy dependence of the single particle potential [168]. In the most general case effective masses reflect the space and time non-locality of the interaction and the Pauli exclusion principle.

There are three types of effective masses considered usually for the models under consideration in this paper: the Dirac mass, the Landau mass and the Lorentz mass. The Dirac mass is a genuine relativistic quantity. It is defined through the scalar self-energy Σ_i^S in the Dirac equation,

$$m_{eff; \text{Dirac}; i} = m_i + \Sigma_i^S, \quad (6)$$

where $i = n, p$ denotes neutrons and protons and m_i stands for the bare mass of the particle i .

The Landau mass is defined in terms of the single particle density of states $d\varepsilon_i/dp_i$ at the Fermi surface at zero temperature,

$$m_{eff; \text{Landau}; i} = p_i \left[\left(\frac{d\varepsilon_i}{dp_i} \right)_{p=p_{F;i}} \right]^{-1}, \quad (7)$$

and characterizes the momentum dependence of the single-particle potential. In eq. (7) p_i and ε_i denote particle's momentum and single particle energy and $p_{F;i}$ stands for the Fermi momentum. In Skyrme-like non-relativistic models as well as in APR, the Landau effective mass allows one to cast the single particle energies,

$$\varepsilon_i = \frac{p^2}{2m_i} + U_i(n_n, n_p, \tau_n, \tau_p), \quad (8)$$

where τ_i and U_i are the kinetic energy densities and single-particle momentum-dependent potentials in

$$\varepsilon_i = \frac{p^2}{2m_{eff; \text{Landau}; i}} + V_i(n_n, n_p), \quad (9)$$

with the potentials V_i depending only on particle densities.

In CDFT models at zero temperature the Landau effective mass relates to the Dirac mass via

$$m_{eff; \text{Landau}; i} = \sqrt{p_{F;i}^2 + m_{eff; \text{Dirac}; i}^2}. \quad (10)$$

The Lorentz mass characterizes the energy dependence of the Schrödinger-equivalent potential and at $T = 0$ is defined as [169]

$$m_{eff; \text{Lorentz}; i} = m_{eff; \text{Landau}; i} + m_i - \varepsilon_i(p_{F;i}), \quad (11)$$

If the nucleon self-energies are independent of momentum, as it is the case of the models considered hereby, the single-particle energies read

$$\varepsilon_i = \Sigma_i^V + \sqrt{p^2 + m_{eff; \text{Dirac}; i}^2}, \quad (12)$$

where Σ_i^V stands for the nucleon vector self-energy. As such eq. (11) becomes

$$m_{eff; \text{Lorentz}; i} = m_i - \Sigma_i^V. \quad (13)$$

According to [169] it is the Lorentz mass that should be compared with the nonrelativistic effective mass.

The thermal effects we are discussing here are determined by the mass entering the kinetic energy term, that is the Dirac mass in CDFT models and the Landau mass in non-relativistic models.

Naturally, the effective masses are correlated with the nuclear matter parameters characterizing the EoS around saturation density, the symmetry energy playing a dominant role in the effective mass difference of protons and neutrons. For a recent review on the interplay between nucleon effective mass and the symmetry energy as well as experimental constraints, compliance with *ab initio* calculations and the role on thermal and transport properties of neutron rich matter, see [168].

Fig. 4 illustrates the density dependence of neutron (left) and proton (right panels) Landau effective masses (eq. (7)) as function of density at $T = 0.1$ MeV and $Y_e = 0.1$ for the different interactions³. With the exception of LS220, which considers a momentum-independent interaction, all models predict a complex density dependence of the effective masses. Models with Skyrme-like effective interactions and the microscopic APR model provide for both neutrons and protons effective masses that decrease with density. Note that, despite the fact that NRAPR [153] was designed to reproduce the effective masses in APR along with some nuclear data, notable differences exist between the predictions of these models in neutron-rich matter. The reason is that the complex density dependence of the effective masses in APR cannot be reproduced with the functional form of Skyrme-like interactions [101]. In this context let us mention that the density dependence of effective masses in KOST/TNTYST qualitatively resembles those of Skyrme models, see fig. 9 in Ref. [91]. As it was the case with energies, discrepancies among APR and KOST/TNTYST arise from differences in the variational procedures. In contrast, the predictions of NRAPR are nearly identical to those of SkAPR, which might serve to highlight the effects of other EoS ingredients, without interference from $m_{eff; \text{Landau}}$ comparing these two EoS. For the CDFT models the Landau effective masses first decrease and then starting from roughly $2n_{sat}$ increase again. This feature is a relativistic effect: at high densities momentum dominates over mass. SLy4 (SFHo) provides the strongest (most limited) density dependence of $m_{eff; \text{Landau}; i}(n_B)$ as well as the lowest (highest) values at high densities.

With the exception of SRO(SLy4) and SRO(KDE0v1) that lead to $m_{eff; \text{Landau}; p} > m_{eff; \text{Landau}; n}$, all models predict

³ The TNTYST table on COMPOSE does not provide that data, see fig. 9 in [91] for that model.

$m_{eff; \text{Landau};n} > m_{eff; \text{Landau};p}$ in neutron-rich matter. We recall that the magnitude of the neutron-proton mass splitting is proportional to the isospin asymmetry and that its sign depends upon isoscalar and isovector contributions to the effective masses, with the latter loosely constrained by experimental data on isovector giant dipole resonances [168]. Microscopic calculations that include three body forces converge in predicting $m_{eff; \text{Landau};n} > m_{eff; \text{Landau};p}$ in neutron-rich matter [170, 171, 172, 173].

The Dirac effective masses, eq. (6), typical to CDFT models are shown in fig. 5 for zero temperature and $Y_e = 0.1$. They monotonically decrease with density. Please note that there is no difference in proton and neutron effective masses here, since the considered CDFT models have no isovector contribution (δ -channel) to the effective masses.

The density dependence of the Lorentz mass, eq. (11), is depicted for a selection of CDFT models in Fig. 6. As before, $T = 0$ and $Y_e = 0.1$. It comes out that the density-dependence of this quantity is stronger than those of Landau and Dirac effective masses. Moreover, for $n_B \gtrsim 4 - 7n_{sat}$ it vanishes. These results agree with those in [174], where a much larger collection of CDFT models has been considered.

Finally we note that the density-dependence of nucleon effective masses may be constrained by the results of *ab initio* calculations. For instance, such calculations, based on a set of commonly used Hamiltonians including two- and three-nucleon forces derived from chiral effective-field theory, are available in [175]. They show that the density-decrease of the nucleon (neutron) Landau effective mass in SM (NM) saturates at $n_B \approx 0.2 \text{ fm}^{-3}$ ($n_B \approx 0.10 - 0.17 \text{ fm}^{-3}$), where $m_{eff; \text{Landau}}/m_{bare} \approx 0.65$ (0.85). It is clear that none of the models considered here agrees with this behavior.

The density dependence of nucleon effective masses at temperatures of the order $T \ll 1 \text{ MeV}$ has been shown to significantly impact the thermal evolution of isolated and accreting NS through the reduction by a factor of up to two or three of the superfluid pairing gaps in the 1S_0 and 3PF_2 channels [176]; the emissivities of different neutrino emitting processes [177, 172]; magnitude of thermal conductivity [178] and specific heats [179].

The role of nucleonic effective masses in finite temperature environments has been discussed in connection with the dynamics of CCSN, contraction of the PNS and the neutrino and GW signals [69, 71, 73]; evolution of PNS in failed CCSN and subsequent formation of BH [70]; post-merger strain of GW [72]. All these works employed parametrized EoS models which allow independent tuning of various NM parameters. In some cases also phenomenological EoS models widely used in the community have been employed. Finite temperature effects have been implemented consistently [100] or via the so-called M^* -approximation [180], see Sec. 4.1. Ref. [69] shows that large effective masses result in higher

temperatures of the neutrinospheres as well as lower values of the neutrinosphere density and radius. These effects are visible for all flavor neutrinos but the largest effect is obtained for electron neutrinos and antineutrinos. Modifications of the neutrinosphere obviously impact the electron neutrino and antineutrino energies at a few hundreds ms after bounce and the neutrino luminosity: high effective masses lead to larger neutrino energies and luminosities. For post-bounce times between roughly 100 ms and 1 s the central density, temperature and PNS radius manifest strong dependence on m_{eff} , too [69, 71], larger m_{eff} values leading to higher values of $n_{B;c}$ and lower values of T_c and R_{PNS} . While [69, 71, 73] agree that m_{eff} also impacts the evolution of the shock radius, they put forward opposite correlations. Ref. [73] shows that shock revival is stronger and occurs at earlier times after bounce when m_{eff} is large, in agreement with what one would expect from an increased neutrino heating. Due on its influence on turbulence and convection in the gain region, these impact the gravitational wave emission, too. Higher effective masses lead thereby to larger amplitude gravitational waves for postbounce times $t \gtrsim 0.1s$ [73]. By performing numerical simulations [70] show that m_{eff} also determines the onset of collapse into a BH for failed CCSN. According to these simulations, the collapse starts immediately after the mass of PNS exceeds the maximum gravitational mass of hot NS, with the latter being strongly dependent on m_{eff} . Large values of the effective masses lead to low values of $M_G^{max}(PNS)$ and, thus, fast collapse. The effect of m_{eff} in hot stellar environments is remarkable as it largely dominates the effects of all other nuclear matter parameters [69, 70, 73].

4 Thermal quantities

In the following section we shall analyze a series of thermal quantities, including thermal energy and pressure and thermodynamic coefficients. Thermal effects on thermodynamic state variables will be estimated by looking at the difference between the finite temperature and the zero temperature quantity

$$X_{th} = X(n_B, Y_e, T) - X(n_B, Y_e, 0) . \quad (14)$$

The values reported for baryons alone are obtained by subtracting from the values provided by the `compose` code, and which correspond to the mixture baryons+leptons+photons, the corresponding leptonic and photonic contributions.

4.1 Energy density and pressure

fig. 7 and fig. 8 illustrate the density dependence of the baryonic thermal energy density and pressure, respectively. Temperature and charge fraction have been fixed to ($T=5$

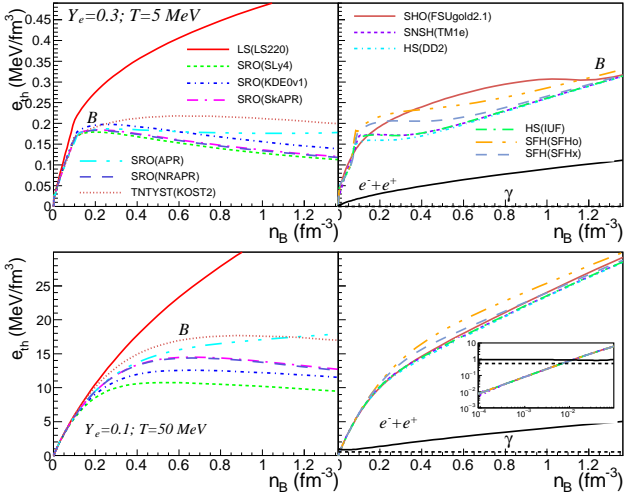


Fig. 7 Baryonic contribution to the thermal energy density e_{th}^B , eq. (14), as function of baryon number density for ($Y_e = 0.3, T = 5$ MeV) (top) and ($Y_e = 0.1, T = 50$ MeV) (bottom). The results are depicted for various EoS models. In the right panels the contributions of leptons (black solid line) and photons (black dashed line) are shown, too. The insert in the right bottom panel shows the results at low densities.

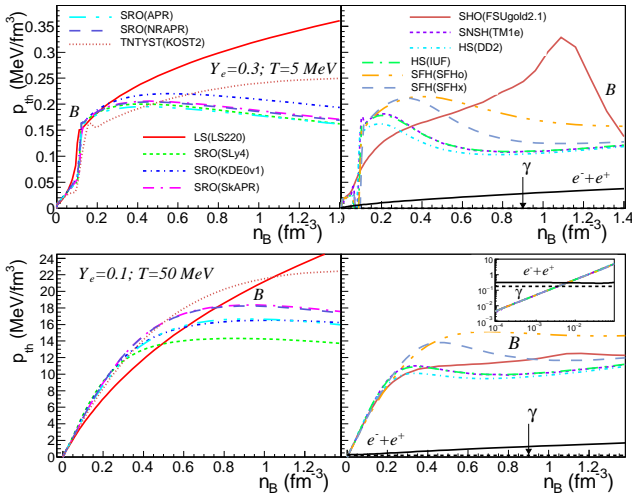


Fig. 8 Same as fig. 7 for the thermal pressure.

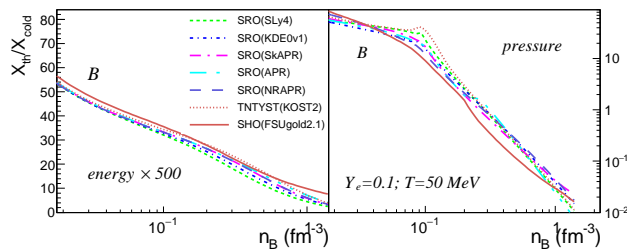


Fig. 9 Ratio of thermal ($T = 50$ MeV) to cold baryonic energy density (left) and pressure (right) as function of baryon number density for a selection of EoS models. An electron fraction of $Y_e = 0.1$ is considered. In the left panel e_{th}/e_{cold} is multiplied by 500.

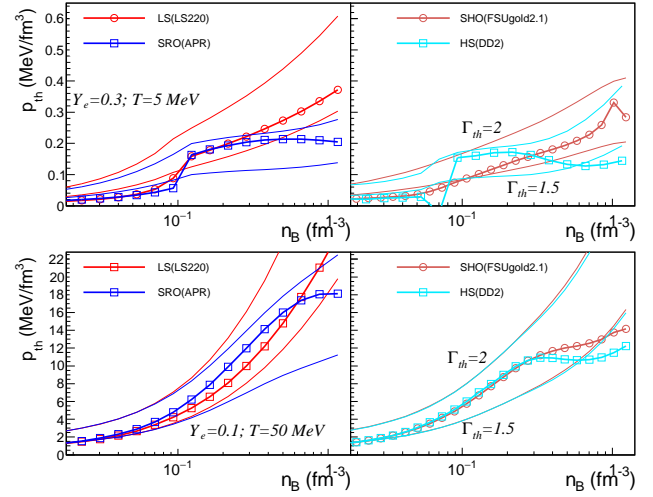


Fig. 10 Predictions of eq. (14) for total thermal pressure (thick lines and symbols) are confronted with predictions of eq. (15) with $\Gamma_{th}=1.5$ (lower thin lines) and 2 (upper thin lines). The considered models are specified in the legend.

MeV, $Y_e = 0.3$) (top panels) and ($T = 50$ MeV, $Y_e = 0.1$) (bottom panels). For low densities, $n_B \lesssim 0.1 \text{ fm}^{-3}$, and high temperatures both e_{th} and p_{th} behave linearly, have no EoS model dependence and approach zero for vanishing density. These features are characteristic of ideal gases and are obtained whenever the interactions are weak enough. Though not visible in the figures, at low temperatures the behavior depends on the effective interaction as well as on the approach adopted to model inhomogeneous matter and, for NSE based models, depart from linearity, too. These obviously means that the ideal gas limit is violated. $p_{th}(n_B)$ predicted by HS(DD2), HS(IUF), SFHo, SFHx and SNSH(TM1e) for ($T = 5$ MeV, $Y_e = 0.3$) manifest discontinuities at $n_B \approx n_{sat}/2$. These are due to the way in which the transition from inhomogeneous to homogeneous matter is dealt with. For $0.1 \lesssim n_B \lesssim 0.2 - 0.5 \text{ fm}^{-3}$, e_{th} still increases with density while p_{th} manifests a complex behavior. For both quantities the values become EoS-dependent. Correlations between the magnitude of thermal effects and values of the nucleonic Landau effective masses are straightforward to establish for non-relativistic models. We remind that in APR and Skyrme-line models the Landau effective mass does not depend on temperature. Indeed, in these models $m_{eff;Landau;i}$ exclusively depend on particle densities. Fig. 7 and fig. 8 show that the largest values of e_{th} correspond to models with large nucleonic Landau effective masses, and the largest values for p_{th} are obtained with small $m_{eff;Landau}$. The first correlation is easy to understand: large values of $m_{eff;Landau}$ result in low single particle energies, easy to populate by thermal excitation. The latter correlation is less trivial. Though, based on the thermodynamic relation $p = n^2 \partial(e/n) / \partial n|_T$, it is clear that, in addition to $m_{eff;Landau;i}$ the pressure will depend on $\partial m_{eff;Landau;i} / \partial n_j$, with $i, j = n, p$, too. This is-

sue was previously discussed in Refs. [67] where analytical expressions have been worked out for Hamiltonian models. For higher densities a diversity of behaviors is obtained. LS220, for which effective masses are equal to bare masses, predicts that both e_{th} and p_{th} increase with n_B ; this result is qualitatively similar to what happens for free gases. TNTYST and non-relativistic models, all showing monotonic density decreases of $m_{eff;Landau;n/p}(n_B)$, predict thermal effects that have a maximum. For $T = 5$ MeV ($T = 50$ MeV) the maxima occur at $n_B \approx 1 - 5n_{sat}$ ($n_B \approx 4 - 6n_{sat}$). For APR, the flattening of $m_{eff;Landau;n/p}(n_B)$ for $n_B \gtrsim 1 \text{ fm}^{-3}$ leads to thermal effects intermediate to those predicted by LS220 and non-relativistic models. More precisely, $p_{th}(n_B)$ and $e_{th}(n_B, 5 \text{ MeV})$ have a maximum while $e_{th}(n_B, T = 50 \text{ MeV})$ increases. Except $e_{th}(n_B)$ at $T = 50$ MeV, for which the results resemble those of LS220, CDFT models predict curves that show a complex behavior and a strong EoS dependence at high densities. Correlations with nucleonic Dirac effective masses are nevertheless difficult to extract, since within CDFT the $m_{eff;Dirac}$ -dependence of single particle energies is rather weak, see eq. (12).

The significance of thermal effects can be judged considering the modifications brought to "cold" quantities. Fig. 9 illustrates the ratios of thermal energy density and pressure relative to their cold counterparts for $T = 50$ MeV and $Y_e = 0.1$. For both quantities naturally the higher the density the smaller the thermal effects. Modifications induced on the pressure are important and depend on the EoS model, those on energy density are insignificant. The ratio of thermal to cold pressure can reach about 100 at a tenth of saturation density, whereas it decreases to a few 1/10 for densities above $2 n_{sat}$. Thus the outer shells of a NS will be more affected than the inner ones and finite temperature will modify more NS radii than masses. Similarly thermal effects will be stronger in low mass NS.

The right panels in Figs. 7 and 8 show contributions of lepton and photon gases, too. As expected, the latter are dominant only at high temperatures and low densities.

Due to the limited number of available finite temperature EoS models, many numerical simulations have been performed with phenomenological extensions of cold EoS, generally using a Γ -law for the thermal part [75, 76, 77, 78]. The total pressure is then written as

$$P(n_B, e) = P_{cold}(n_B) + (\Gamma_{th} - 1) e_{th}(n_B), \quad (15)$$

where Γ is a constant factor with values taken in the range $1.5 \leq \Gamma \leq 2$. No dependence on temperature, density or chemical composition of the Γ -factor is considered.

Fig. 10 compares the total thermal pressure calculated by eq. (14) with the estimation provided by the Γ -law, eq. (15). It is obvious that the monotonic behavior of eq. (15) is far from accounting for the complex density dependence of $p_{th}(n_B)$, due to the complex density dependence of the

Landau (for non-relativistic models) and Dirac (for CDFT models) effective masses. Moreover at extreme density values the predictions of eq. (14) are situated out of the domain limited by eq. (15) with $\Gamma_{th}=1.5$ and 2. The inability of the Γ -law to correctly account for the thermal pressure was recently noticed in Ref. [180], who proposed an alternative solution. The so-called M^* -approximation allows to calculate the pressure of stellar matter at arbitrary values of proton fraction and temperature using analytic expressions whose parameters account for the symmetry energy and the density dependence of the effective mass. The functional dependence proposed in [180] based on CDFT calculations is Table to account within a few percent for the thermal pressure of the respective CDFT EoS. Nevertheless it performs modestly for non-relativistic EoS models. This suggests that different density dependence of the effective mass have to be employed in the different formalisms to reproduce the same finite temperature phenomenology, because the quantities are not the same and are not expected to behave in the same way as a function of density.

4.2 Thermal index

To complete the discussion in the preceding section, we can compute the Γ -factor from our different EoS models as

$$\Gamma_{th} = 1 + \frac{p_{th}}{e_{th}} \quad (16)$$

and compare it with the range of values usually assumed. In addition, we will be able to see the importance of its density, temperature and charge fraction dependence and thus check the validity of this approximation of thermal effects.

The left panels in fig. 11 illustrate the evolution of Γ_{th} as function of n_B at ($T = 5$, $Y_e = 0.3$) (top), ($T = 20$, $Y_e = 0.1$) (middle) and ($T = 50$ MeV, $Y_e = 0.1$) (bottom). The same EoS models as in Figs. 7 and 8 are considered. Again, as in Figs. 7 and 8, we focus on the baryonic sector. The low density behavior is common for all models. For the highest temperature considered $\lim_{n \rightarrow 0} \Gamma_{th;B} \rightarrow 5/3$ while progressively lower values are obtained for $\lim_{n \rightarrow 0} \Gamma_{th;B}$ when the temperature decreases. The value $5/3$ corresponds to the classical limit for a dilute gas. Deviations from this value at lower temperatures are attributable to the clusterized component and show that in these situations the plotted densities are not low enough for the classical limit to be reached. We nevertheless note that the curves show little sensitivity to the EoS model. At high densities the various EoS models behave differently: i) passing from inhomogeneous to homogeneous matter, in LS220 it smoothly goes from the low density value to a constant value of $5/3$; ii) models based on Skyrme-like effective interactions and, for temperatures exceeding a certain value, also TNTYST(KOST2) provide Γ_{th} increasing monotonically with n_B ; iii) SRO(APR) provides a complex

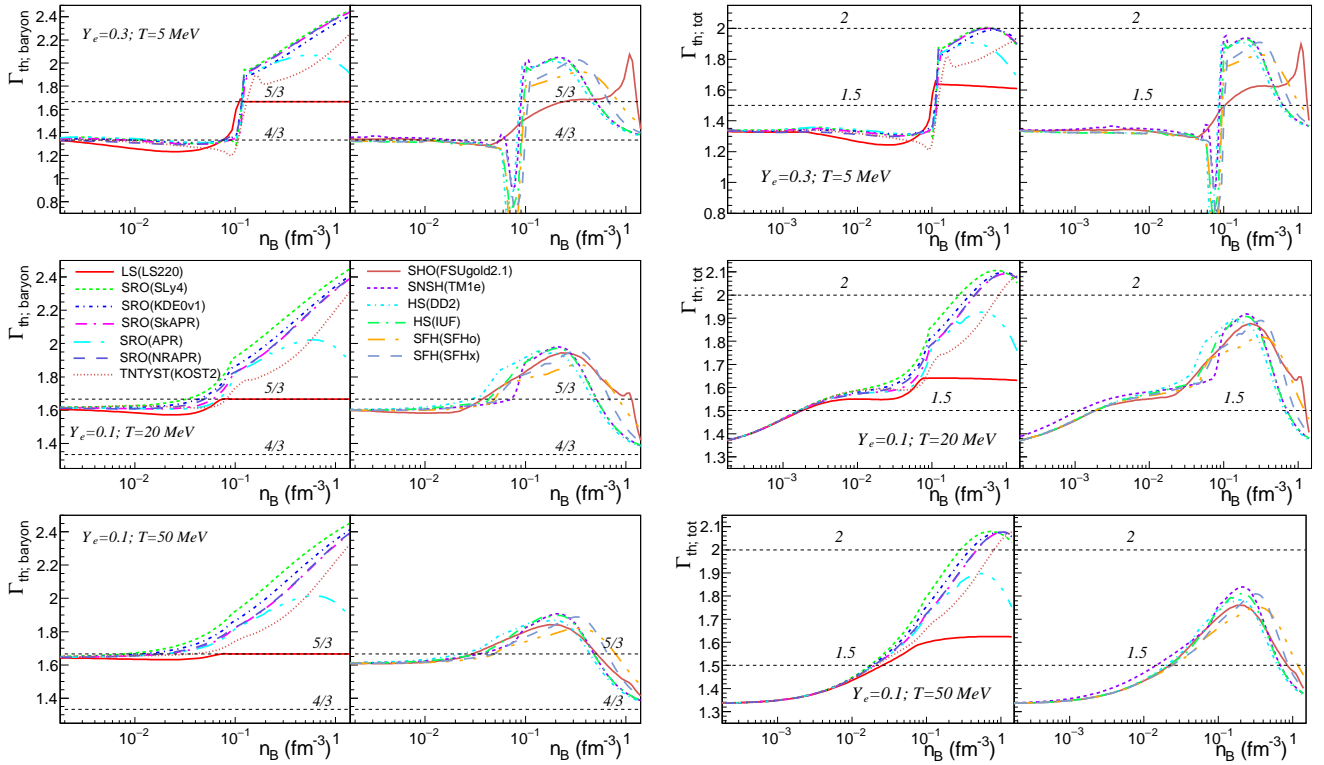


Fig. 11 Γ_{th} as a function of baryon number density at $(T=5 \text{ MeV}, Y_e = 0.3)$, $(T=20 \text{ MeV}, Y_e = 0.1)$, $(T=50 \text{ MeV}, Y_e = 0.1)$. Left panels: results corresponding to the baryonic sector; right panels: contributions of lepton and photon gases are also included. The same EoS models as in fig. 3 are considered. Dashed horizontal lines mark the values $\Gamma_{th} = 4/3$ and $5/3$ (left panels) and, respectively, $\Gamma_{th} = 1.5$ and 2 (right panels).

and non-monotonic evolution of $\Gamma_{th}(n_B)$, with a maximum value at $n_B \approx 3n_{sat}$; iv) $\Gamma_{th}(n_B)$ predicted by CDFT models has a maximum at $n_B \approx 0.2 - 1 \text{ fm}^{-3}$ and then decreases smoothly; some models manifest a sudden drop of Γ_{th} at n_t which arise due to the particular way in which the transition from inhomogeneous to homogeneous matter has been constructed and is non physical. We note that the high density limit of Γ_{th} in CDFT, $4/3$, corresponds to ultra-relativistic gases. This can be understood from the small Dirac effective masses at high densities within these models. We attribute the qualitatively different behaviors of $\Gamma_{th}(n_B)$ in non-relativistic versus CDFT models to the functionally different dependence of single particle energies on Landau/Dirac masses. The occurrence of a maximum in $\Gamma_{th}(n_B)$ within CDFT was previously linked to the minimum in $m_{eff;Landau}(n_B)$, for a derivation in the limit of low temperatures, see [68].

Each of these behaviors corresponds to a certain density-dependence of the effective masses $m_{eff}(n_B)$ which can qualitatively be understood as follows. In the limiting case of degenerate matter without electrons, Γ_{th} writes [68]:

$$\Gamma_{th}(n_B) = \frac{5}{3} - \frac{n_B}{m_{eff;Landau}} \frac{dm_{eff;Landau}}{dn_B}. \quad (17)$$

Models with constant values of Landau effective masses (LS220) will provide $\Gamma_{th}(n_B) = 5/3$; models with decreasing $m_{eff}(n_B)$ will provide $\Gamma_{th}(n_B)$ increasing with n_B (Skyrme models and

TNTYST); models with non-monotonic evolution of $m_{eff}(n_B)$ will provide non-monotonic evolution of $\Gamma_{th}(n_B)$ (APR and CDFT). Finite-temperature calculations of nuclear matter within the many-body self-consistent Green's function method [181] showed that eq. (17) is satisfied even beyond the degenerate regime. Our CDFT calculations at low temperatures indicate that eq. (17) is valid also for this category of models and for any n_B . This implies that, in principle, estimations of the nucleon Landau effective mass in PNM and SNM may be obtained by integrating eq. (17) for any EoS model. The limiting condition for this integration is $\lim_{n_B \rightarrow 0} m_{eff;Landau} = m_N$.

Concerning the temperature dependence, we note that for low temperatures, $\Gamma_{th}(n_B)$ shows strong dependence on T , which becomes more moderate with increasing T .

The values of Γ_{th} in Figs. 11 (left panels) can nevertheless not be compared with those assumed when cold EoS are phenomenologically supplemented with thermal effects $1.5 \leq \Gamma \leq 2$ [76] because we have disregarded the contributions of leptons and photons. Therefore in the right panels in fig. 11 we display the total thermal index. It turns out that while leptons and photons do not modify the qualitative features of the various EoS models, they significantly alter the values. We note in particular that: i) at low densities, all considered EoS models give $\Gamma_{th;tot} < 1.5$, ii) at high densities and high temperatures, models based on Skyrme-like interactions and TNTYST provide $\Gamma_{th;tot} > 2$, iii) at high

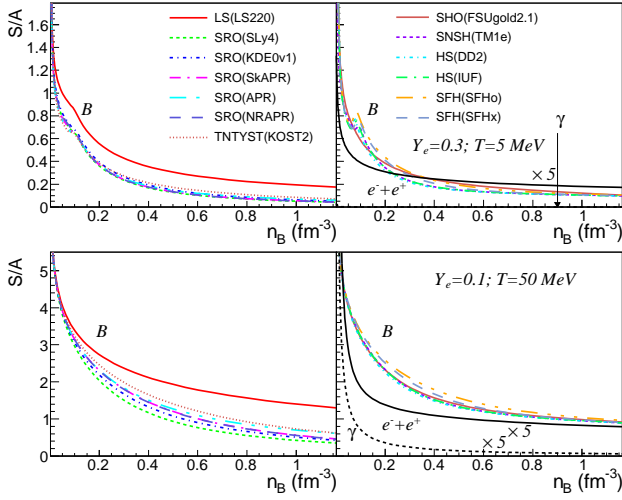


Fig. 12 Baryonic contribution to the entropy per baryon as function of baryon number density for $(T=5 \text{ MeV}, Y_e = 0.3)$ and $(T=50 \text{ MeV}, Y_e = 0.1)$. Contributions of leptons and photons, multiplied by five, are depicted in the right panel (solid and dashed lines, respectively).

densities, CDFT models provide $\Gamma_{th;tot} < 1.5$ irrespective of temperature. For $T > T_C$, where T_C represents the critical temperature of the liquid-gas phase transition of subsaturated nuclear matter, $\Gamma_{th;tot}$ is weakly-dependent on T . We have found that the dependence on Y_e is weak, too.

4.3 Entropy, specific heats, adiabatic index and speed of sound

Further insight into the impact of the chosen EoS model on thermodynamic quantities is offered in fig. 12. It shows the baryonic contribution to the entropy per baryon for $(T=5 \text{ MeV}, Y_e = 0.3)$ and $(T=50 \text{ MeV}, Y_e = 0.1)$. At fixed T , S/A obviously decreases with n_B within all models. However, as seen before, quantitatively, a large dispersion is observed. Non-relativistic models show that the larger $m_{eff;Landau}$ the larger S/A . This correlation among Landau effective masses and entropy is valid at all densities, temperatures and proton fractions and can be easily understood from the role of the Landau effective masses in the kinetic energy. For any $T < T_C$, all EoS models manifest a kink or a discontinuity at $n_B \approx n_{sat}/2$. These are artifacts of the procedures employed for the transition between clusterized and homogeneous matter and will manifest in the behavior of most thermodynamic quantities, e.g. the Γ factor discussed before.

For the thermodynamic conditions considered here, contributions of leptons and photons are quantitatively important only for low densities, with increasing weight for increasing temperature.

Specific heats at constant volume and constant pressure are defined as

$$C_V = T \frac{\partial(S/A)}{\partial T} \Big|_{V, \{N_i\}}, \quad (18)$$

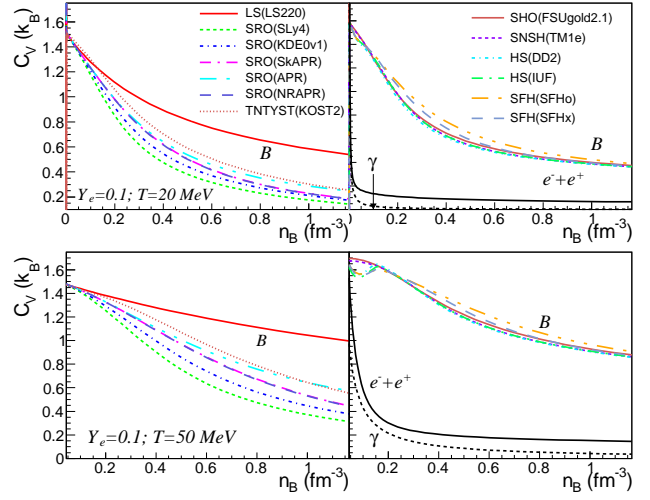


Fig. 13 Specific heat at constant volume, C_V , as function of baryon number density for baryonic matter with $T=20 \text{ MeV}$ and $T=50 \text{ MeV}$ at $Y_e = 0.1$. In the right panels for comparison C_V of the corresponding lepton and photon gases are shown, too.

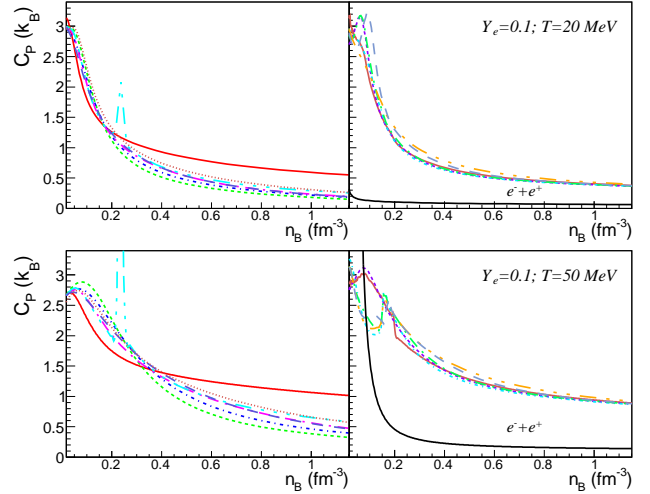


Fig. 14 Same as in fig. 13 for the specific heat at constant pressure, C_P . Line-types are the same as in fig. 13. The photon contribution is not shown here as it is ill defined.

and, respectively,

$$C_P = T \frac{\partial(S/A)}{\partial T} \Big|_{P, \{N_i\}} = C_V + \frac{T}{n_B^2} \left(\frac{\partial P}{\partial T} \Big|_n \right)^2, \quad (19)$$

where $A = \sum_i N_i$ is the total number of particles of the system.

Figs. 13 and 14 illustrate the evolution of C_V and C_P as function of baryon number density for $T=20 \text{ MeV}$ and $T=50 \text{ MeV}$ at $Y_e=0.1$. Contributions of baryons, leptons and, in the case of C_V , also photons are reported separately.

Concerning C_V , except the CFDT models at $T = 50 \text{ MeV}$ and low densities, all models behave similarly. More precisely they replicate the behavior seen in fig. 12 for $S/A(n_B)$. The maximum value is reached in the limit of low densities

and the higher the density the smaller C_V . $\lim_{n_B \rightarrow 0} C_V = 3/2$, which corresponds to the classical value of a Boltzmann gas. According to [67,68] all dilute homogeneous Fermi gases with local interactions comply with this limit. Our results show that this is also the case of dilute inhomogeneous nuclear matter, though for the considered temperature values the amount of matter bound in clusters is negligible, see Sec. 5.

At $T=50$ MeV and low densities the CFDT models present one or two maxima in $C_V(n_B)$ and their values exceed $3/2$. SHO(FSUgold2.1) and SNSH(TM1e) models have a maximum at $n_B \approx 0.1 \text{ fm}^{-3}$; models belonging to the HS [123] family reach the highest C_V value in the limit $n_B \rightarrow 0$ and have a second maximum at $n_B \approx 0.2 \text{ fm}^{-3}$. According to [68] the maxima in C_V at non-vanishing densities are typical for non-local interactions. The second maximum, present only in models based on [123], is likely a numerical artifact with still some nuclear clusters present. In the high density range, the dispersion in the values of $C_V(n_B)$ as well as the ordering of the models replicate the behavior of the entropy per baryon, see fig. 12. It is again the impact of the effective masses which is recovered here.

Except some specific and local structures that appear for APR and the HS [123] CDFT models, the qualitative behavior of the specific heat at constant pressure as a function of density is the same for all models. In the limit $n_B \rightarrow 0$ all curves converge to a unique, but temperature dependent, value. At high temperatures $\lim_{n_B \rightarrow 0} C_P \rightarrow 5/2$, which corresponds to Boltzmann gases. At low densities $C_P(n_B)$ features a short peak; its structure is better shaped at high temperatures. For the analytic derivation of the onset of this peak in the case of homogeneous matter in the non-degenerate limit, applicable to low densities and high temperatures, see [67]. Finally, at large densities $C_P(n_B)$ decreases. Dependence of pressure on both effective masses and their derivatives with respect to density [67] leads to a more complex evolution of $C_P(n_B)$ than for $C_V(n_B)$. The specific feature of APR resides in the spike at $\approx 0.2 \text{ fm}^{-3}$, which signals the transition to the pion condensed state. The models based on [123] present a double peaked structure, as it was also the case with $C_V(n_B)$, which is again probably due to the presence of some nuclear clusters in this region.

Finally, for the thermodynamic conditions considered here, lepton and photon contributions are dominant at low densities and negligible at supranuclear densities.

The behavior of the adiabatic index, defined as

$$\Gamma_S = \left. \frac{\partial \ln P}{\partial \ln n_B} \right|_S = \frac{C_P}{C_V} \frac{n_B}{P} \left. \frac{\partial P}{\partial n_B} \right|_T, \quad (20)$$

is illustrated in fig. 15 for stellar matter, *i.e.* including baryons, leptons and photons. The predictions by various EoS models at different thermodynamic conditions are considered. Γ_S gives an indication about the stiffness of the EoS in all processes occurring at constant entropy.

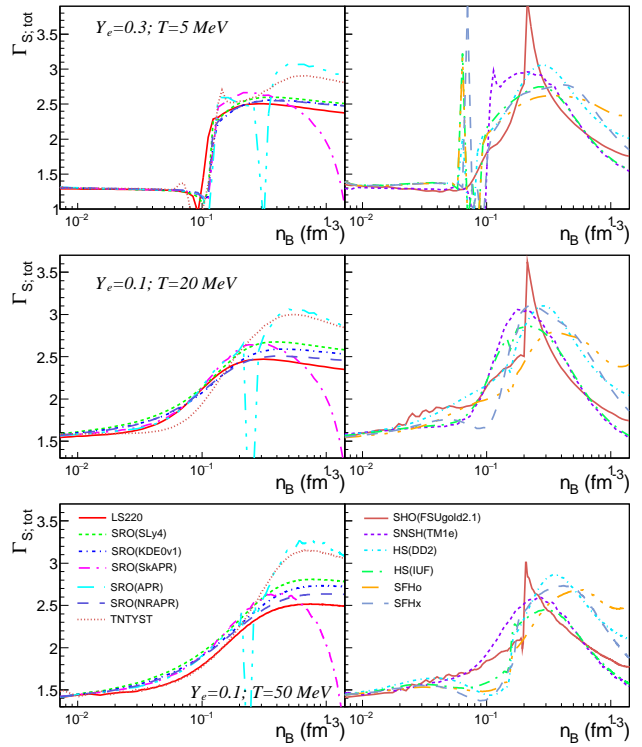


Fig. 15 Γ_S , eq. (20), as function of baryon number density for ($T=5$ MeV, $Y_e = 0.3$), ($T=20$ MeV, $Y_e = 0.1$) and ($T=50$ MeV, $Y_e = 0.1$). Results corresponding to stellar matter, as predicted by various EoS models.

Qualitatively, all EoS models behave rather similarly: at low densities Γ_S tends to a constant value, Γ_S is then increasing with density, reaching a maximum around a few times nuclear matter saturation density and decreasing again at high densities. It is not straightforward to interpret the quantitative differences between the EoS models at high densities, for instance in terms of effective masses. However, we note that the spike present in the curve corresponding to SRO(APR) is due to the transition to pion condensed phase and that the irregularities present at $T < T_C(Y_p)$ and $n_B \approx n_t$ in the curves predicted by models based on the HS NSE approach [123] are related to the transition from inhomogeneous to homogeneous matter. For $T = 5$ MeV and $n_B < n_t$, where the liquid-gas coexistence might manifest, $\Gamma_S \neq 0$. Two alternative explanations can be put forward. First, because of the electron gas, the phase coexistence might be suppressed [182]. Alternatively, if the phase coexistence persists, deviations from $\partial P / \partial n_B|_T = 0$ may stem from the fact that the transition from inhomogeneous to homogeneous matter was not realized via a Maxwell construction, as it should, but by minimizing the free energy for fixed value of Y_p . Indeed, for numerical convenience many EoS models have adopted this solution, see Sec. 2.2. Γ_S depends strongly on the EoS model and density. On the contrary, the dependence on Y_e and temperature is weak, especially at $T > T_C$.

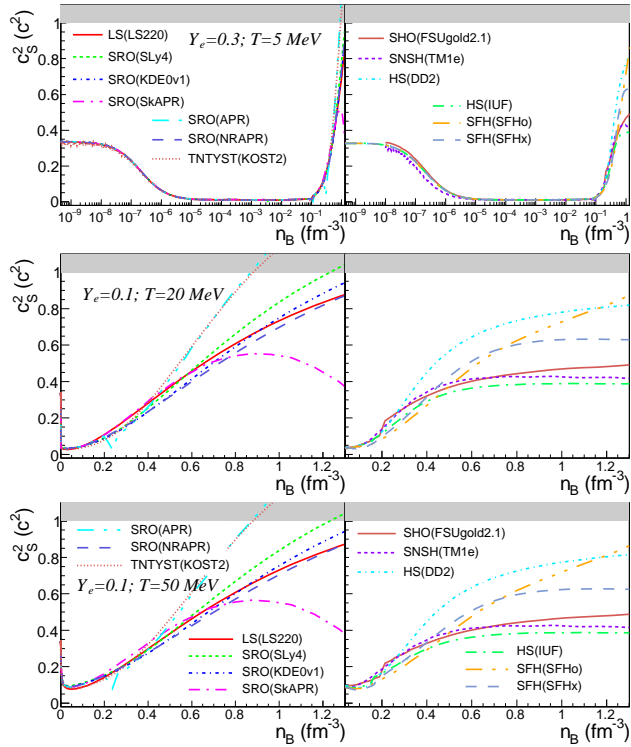


Fig. 16 Speed of sound squared, eq. (21), as function of baryon number density in stellar matter for various EoS models. The considered thermodynamic conditions are: ($T=5$ MeV, $Y_e = 0.3$), ($T=20$ MeV, $Y_e = 0.1$) and ($T=50$ MeV, $Y_e = 0.1$). The shaded area marks the domain $c_s^2 > 1$ forbidden by causality.

A key quantity in dynamical numerical simulations is the speed of sound c_s . In units of c , the speed of light, it is given by

$$c_s^2 = \frac{dP}{de} \Big|_{S,A,Y_e} = \Gamma_S \frac{P}{e+P}. \quad (21)$$

Fig. 16 illustrates its behavior as function of baryon number density within the different EoS models. Different thermodynamic conditions, indicated in the figures, are considered. We note that for the lowest considered temperature and a model-independent density range, $10^{-5} \text{ fm}^{-3} \lesssim n_B \lesssim n_t$, c_s^2 has a small but non-vanishing value. This domain roughly corresponds to the domain of coexistence between the liquid and gas phases of pure baryonic matter. As for Γ_S , to which c_s^2 is related, the non-vanishing values may be attributed either to the quenching of the coexistence region or, if this is not the case, to the way in which the transition from the clusterized phase to the homogeneous one was performed. As such the small value of c_s^2 should be regarded as a consequence of the dominance of energy density over pressure. We also note that the transition to the pion condensate phase in SRO(APR) is signalled by a spike. The density where this spike occurs ranges from $\approx 0.2 \text{ fm}^{-3}$ to $\approx 0.32 \text{ fm}^{-3}$, as Y_e increases from 0 to 0.5 [86]. At high densities, the models incorporating relativistic kinematics reach a saturation, whereas it is obvious that for the non-relativistic models c_s

continues to increase and some models reach the causal limit below a density of 1 fm^{-3} . SkAPR singles out by c_s decreasing with density over $n_B > 0.8 \text{ fm}^{-3}$. This behavior is the consequence of the condition to reproduce the pressure of SNM and PNM at $4n_{sat}$ calculated by APR, imposed to SkAPR [101], and the stiffer evolution of $p(n_B)$ in SkAPR with respect to APR up to $4n_{sat}$, see also Figs. 1 and 2. Concerning the temperature dependence, it turns out that for $T > T_C$, c_s only weakly depends on T . c_s weakly depends on Y_e , too, though not shown here.

5 Composition and thermodynamic quantities of subsaturated matter at finite temperature

For given thermodynamic conditions, the nuclear distribution in stellar matter depends on the modelling (NSE vs. SNA, mass and isospin asymmetry distributions of cluster degrees of freedom, shape degrees of freedom, nuclear binding energies, excited states and level densities, in-medium and temperature modification of nuclear energy density, density dependence of the symmetry energy, evolution of shell effects far from stability, etc.) and on the employed effective nucleonic interaction [123, 79, 183, 131, 184].

Figs. 17 and 18 illustrate the evolution with temperature and baryon number density of the (average) particle fractions of different species (neutron, protons, ^2H , ^3H , ^3He , ^4He , "light" and "heavy" clusters) for $n_B = 3 \cdot 10^{-2} \text{ fm}^{-3}$ and, respectively, $T=5$ MeV at $Y_e = 0.1$ and $Y_e = 0.3$. We recall that among the considered models SRO(SLy4) and STOS(TM1) rely on SNA while GRDF1(DD2), GRDF2(DD2), HS(DD2), RG(SLy4) and FYSS(TM1) rely on extended NSE. In addition to the light species whose abundances are explicitly considered in Figs. 17 and 18, RG(SLy4) accounts for exotic isotopes of light nuclei like $^4 \leq A \leq 14 \text{H}$, $^5 \leq A \leq 17 \text{He}$, $^8 \leq A \leq 17 \text{Li}$, etc.; for $n_B - T - Y_e$ domains where some of these neutron-rich light nuclei are copiously produced, see [131]. Inclusion of unstable states in the NSE pool is motivated by the high temperature and neutron-richness of the environment. GRDF1(DD2) and GRDF2(DD2) account for $nn(^1S_0)$, $np(^1S_0)$, $pp(^1S_0)$ as effective resonances with medium dependent properties. Apart from differences in the considered pool of nuclei, there are differences in modelling, see the discussion in Sec. 2.2.

Despite these many differences, some common features are observed. Among others, in fig. 17 it can be seen that the abundances of unbound nucleons increase with temperature in all models and light nuclei survive beyond the critical temperature of the nuclear matter liquid-gas phase transition, for which the maximum value $T_C \approx 16 - 18$ MeV, is reached in SM. Similarly, increased isospin symmetry of the mixture favors nuclear clusters at the cost of unbound nucleons. Differences in modelling mostly impact the density domain where a significant amount of matter is bound in mas-

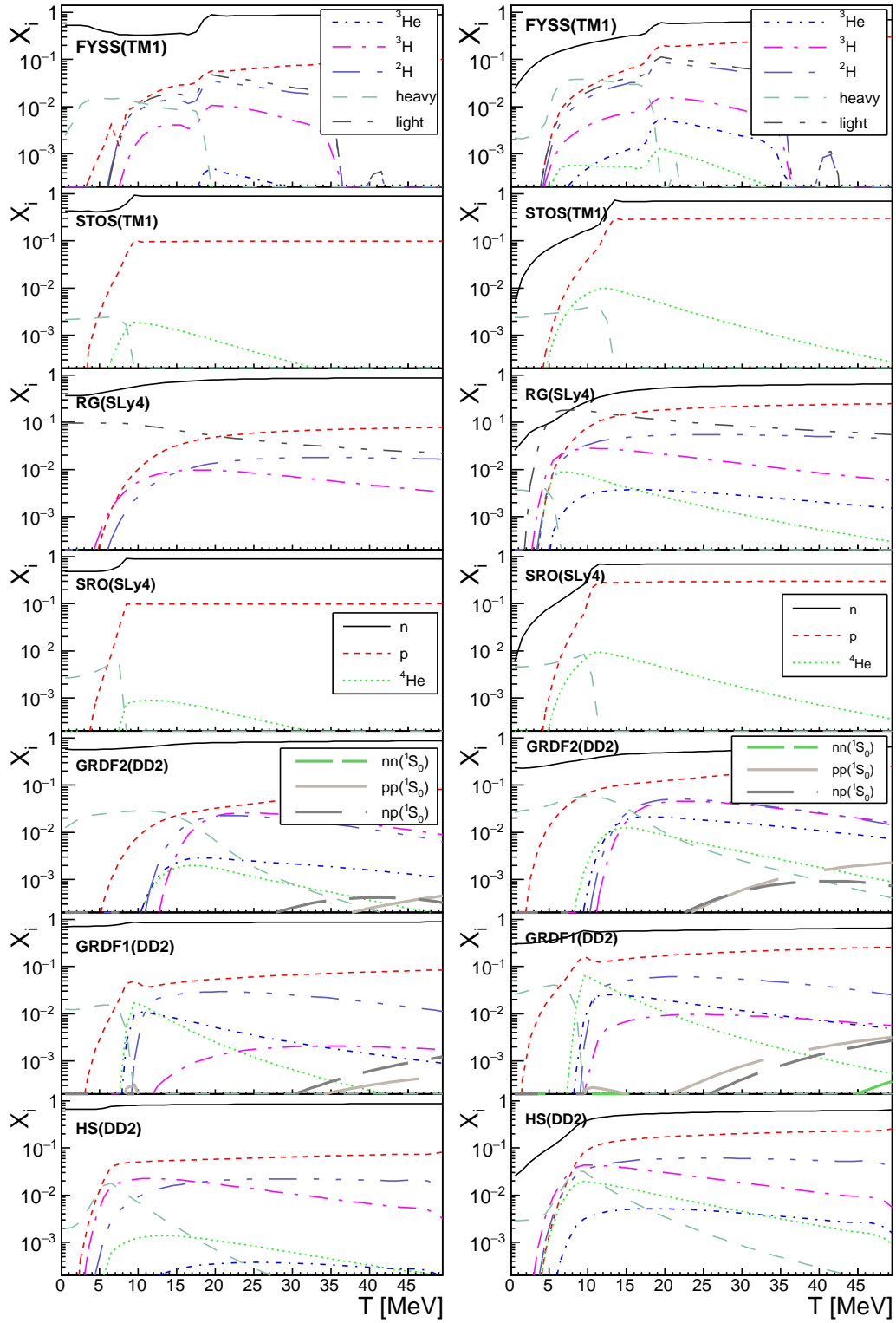


Fig. 17 Composition of stellar matter in terms of (average) particle fractions as function of temperature at $n_B = 3 \cdot 10^{-2} \text{ fm}^{-3}$ for $Y_e = 0.1$ (left) and $Y_e = 0.3$ (right) for various EoS models. "Light" clusters refer to nuclei with $2 < A \leq 20$ (RG(SLy4)) or $Z \leq 5$ (FYSS(TM1)); "heavy" clusters refer to nuclei with $A \geq 20$ (RG(SLy4)) or $Z > 5$ (FYSS(TM1)) or all nuclei other than (${}^2_1\text{H}$, ${}^3_1\text{H}$, ${}^3_2\text{He}$, ${}^4_2\text{He}$) (HS(DD2), GRDF1(DD2), GRDF2(DD2)) or all nuclei other than ${}^4_2\text{He}$ (STOS(TM1) and SRO(SLy4)). For GRDF1(DD2) and GRDF2(DD2) the fraction of ${}^2_1\text{H}$ includes contributions from the deuteron bound state and continuum correlations in the $np({}^3S_1)$ channel.

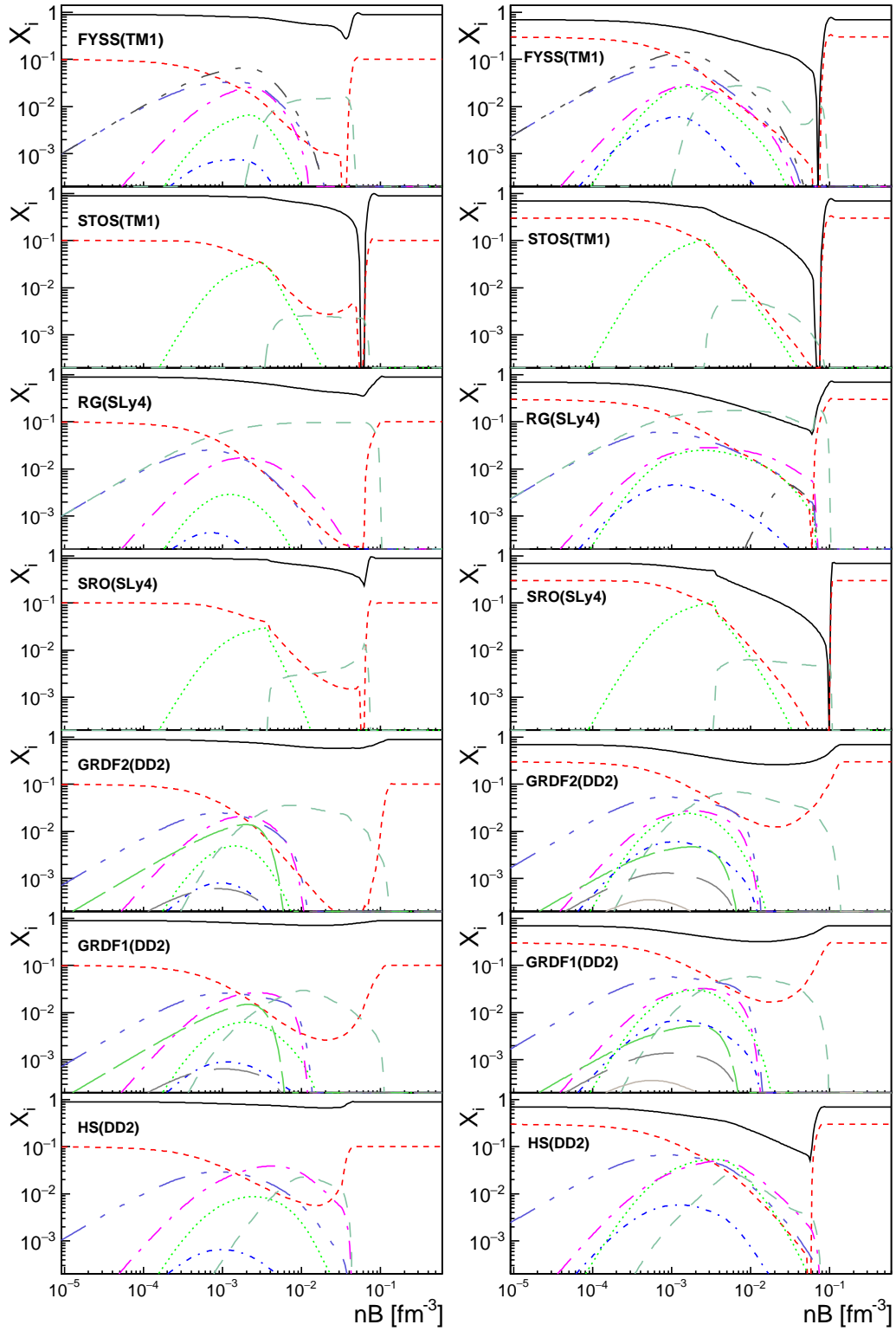


Fig. 18 Composition of stellar matter in terms of (average) particle fractions as function of baryon number density at $T=5$ MeV for $Y_e = 0.1$ (left) and $Y_e = 0.3$ (right panels) for various EoS models. Line types and nuclear clusters are defined as in fig. 17.

sive clusters. Implementation of a temperature-dependent surface tension that vanishes at $T_C(Y_p)$ in SRO(SLy4), STOS(TM1) and FYSS(TM1) results in the sudden disappearance of the "heavy" nucleus at $T = T_C(Y_p)$. Differences in the estimation of excluded volume, nuclear level density, maximum allowed excitation energy and, in the case of GRDF1(DD2), GRDF2(DD2) and FYSS(TM1), in-medium and/or temperature modifications of the nuclear binding energies along with the definition of "heavy" nuclei are reflected in a variety of behaviors for $X_{heavy}(n_B)$, including the density where $X_{heavy} < 10^{-4}$, the lower limit in the figure.

Fig. 18 shows that clusters, light and heavy, exist in significant amounts only over limited domains of baryon number density and, similarly to what we have seen in fig. 17, their abundances increase with Y_e . In very dilute matter unbound nucleons dominate. For $n_t(T)/100 \lesssim n_B \lesssim n_t(T)$ matter composition is strongly model dependent. A few other points should be mentioned: i) in-medium modifications of binding energies in GRDF1(DD2) and GRDF2(DD2) result in the dissolution of light clusters at a baryonic number density one order of magnitude lower than the one corresponding to the transition to homogeneous matter; at variance with this heavy clusters survive up to larger densities in GRDF models than in HS; ii) in models where the transition to homogeneous matter is determined by excluded volume most light clusters survive up to this transition density.

Both Figs. 17 and 18 show that, except for neutron-rich matter near the transition density, SNA based models show the same pattern under specific thermodynamic conditions; at moderate isospin asymmetries mass sharing in RG(SLy4) and HS(DD2) is similar whereas it differs at large asymmetries; predictions of these two models which do not account for in-medium and thermal modifications of the cluster energy are very different than those of FYSS(TM1); mass sharing is significantly different in the two GRDF models; only a small fraction of unbound nucleons features correlations and their importance increases with temperature and proton fraction.

As a remark of caution, let us remind that for $10^{-2} \text{ fm}^{-3} \lesssim n_B \lesssim n_t$ and temperatures of the order of a few MeV the strongly discontinuous surface contribution of the nuclear free energy due to nuclear shell effects results in multi-modal cluster distributions [185, 79]. This means, that the compositional information provided in COMPOSE in terms of one average heavy nucleus cannot correctly describe the actual distribution. Among others, this prevents a realistic calculation of weak interaction rates [186, 185].

Despite significant effects on composition, there is consensus that the details of the nuclear distribution at subsaturation densities has only a small impact on the thermodynamics of the system [187, 93, 100, 131].

In the following discussion we shall investigate to which extent this assertion is true. We shall first confront results

corresponding to models based on the same effective interaction but relying either on SNA or NSE. The consequences of accounting for the cluster's in-medium surface energy modification and particle correlations in the continuum will be further analyzed by comparing the results of HS(DD2) with those of GRDF1(DD2) and GRDF2(DD2). Thermodynamic conditions, in particular the value of Y_e , are chosen such as to maximize the effects.

The results of extended NSE models versus SNA approximations are addressed in Figs. 19 and 20. The models RG(SLy4) and FYSS(TM1) rely on extended NSE while the models SRO(SLy4) and STOS(TM1) employ the SNA approximation. At the lowest considered temperature, $T = 1$ MeV, where the nuclear distribution is well described by a unique nucleus embedded in a sea of unbound nucleons, the discrepancies between SNA and NSE originate from differences in the employed nuclear binding energies and are small for all considered quantities. The minimum in the free energy density per nucleon as function of n_B occurring at $n_{sat}/2$ within RG(SLy4) is probably an artifact of the way in which the transition between clusterized and homogeneous matter was realized. RG(SLy4), which implements the experimental mass table in [115], and FYSS(TM1), which accounts for shell effects, provide oscillatory behavior of the charge chemical potential μ_Q as function of density, while the two SNA models which employ a liquid-drop approximation (SRO(SLy4)) or the extended Thomas-Fermi approximation (STOS(TM1)) lead to a smooth behavior. In-medium modifications of the cluster surface energy in FYSS(TM1) explain the damping of these oscillations as the density increases. At $T = 5$ and 9 MeV a significant dispersion is obtained between the predictions of various models for all quantities except the baryonic pressure. At low densities, NSE-based models provide lower values of the baryonic free energy density than their SNA counterparts. Because of the chosen electron fraction value, $Y_e = 0.5$, the charge chemical potential μ_Q is small over the whole density range. At low baryon number densities as well as for $n_B > n_t$, where unbound nucleons are dominant or the only constituents of matter, $\mu_Q = 0$. Over the density domain where a significant amount of matter is bound in clusters, μ_Q has non vanishing values. Most often $\mu_Q > 0$, meaning that the gas of unbound nucleons is slightly proton rich. This is due to the slight neutron enrichment of nuclear clusters. Among the considered cases, for $T = 9$ MeV and $3 \cdot 10^{-2} \text{ fm}^{-3} \lesssim n_B \lesssim n_t$ RG(SLy4) provides $\mu_Q < 0$. This means that, on the contrary, clusterized matter is proton rich and the gas neutron rich. It turns out that for both, chemical potentials and free energy, the results depend more on cluster modelling than on the effective interaction. For all considered conditions pressure is found to be negligibly affected by modelling.

Fig. 21 and 22 investigate the modifications brought by cluster surface energy modifications and particle correlations

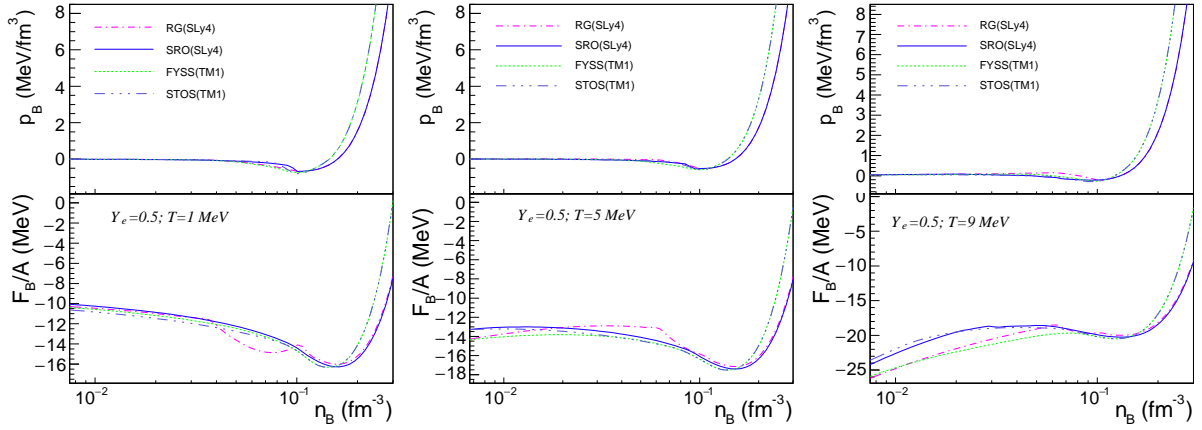


Fig. 19 Baryonic contribution to the free energy per nucleon and pressure as function of baryon number density for $T = 1, 5, 9$ MeV and $Y_e = 0.5$ for models which employ the same effective interaction but adopt different models for inhomogeneous matter at sub-saturation densities. SRO(SLy4) and STOS(TM1) rely on SNA while RG(SLy4) and FYSS(TM1) employ extended NSE.

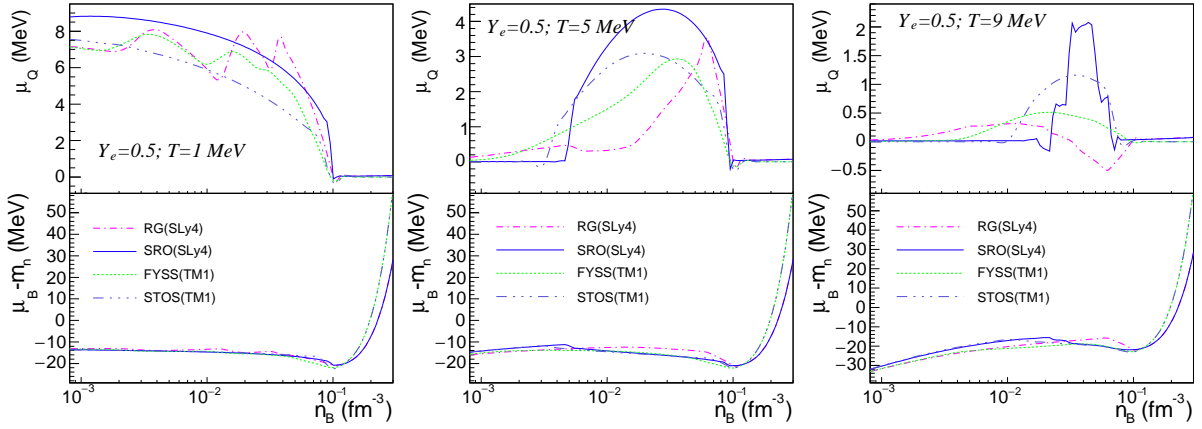


Fig. 20 The same as in Fig. 19 for baryon μ_B and charge chemical potentials $\mu_Q = \mu_p - \mu_n$. In the latter case the contribution of neutron and proton rest masses is not included in the corresponding chemical potentials.

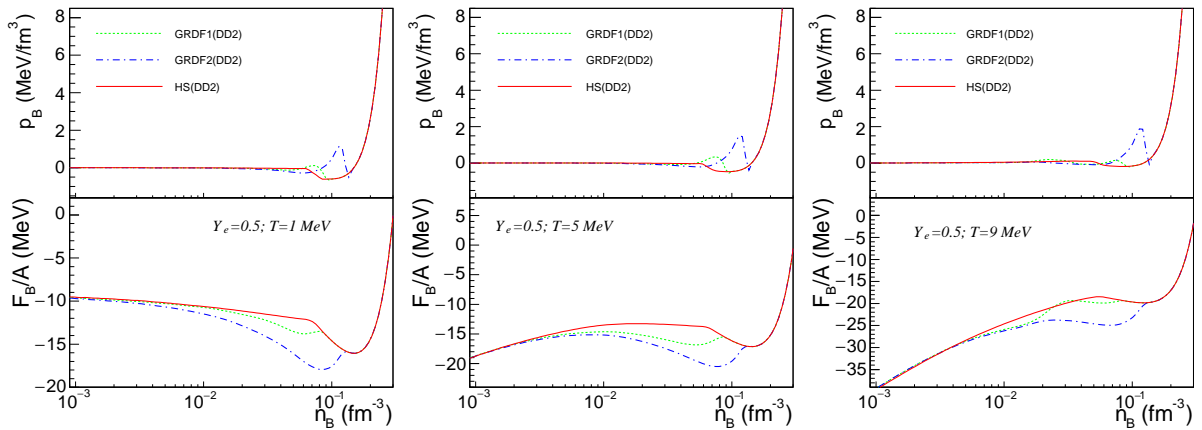


Fig. 21 The same as in Fig. 19 but for models which use different cluster energy functionals and, in the case of GRDF models, additionally account for particle correlations in the continuum. All considered models employ extended NSE and the DD2 [116] effective interaction.

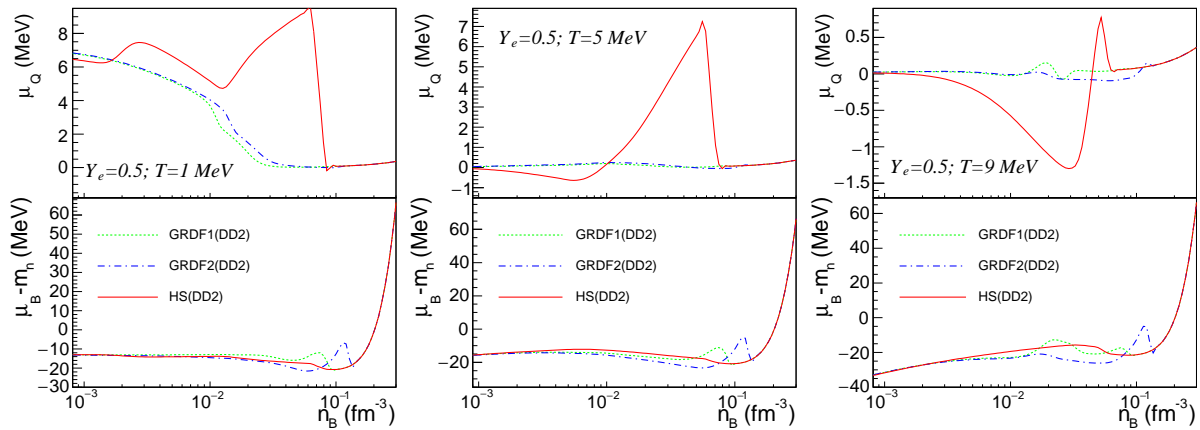


Fig. 22 The same as in Fig. 21 for baryon μ_B and charge $\mu_Q = \mu_p - \mu_n$ chemical potentials. In the latter case the contribution of neutron and proton rest masses is not included in the corresponding chemical potentials.

in the continuum by comparing the results of HS(DD2), GRDF1(DD2) and GRDF2(DD2). The same quantities and thermodynamic conditions as previously discussed are considered. For all thermodynamic quantities and conditions the effects are stronger than those in Figs. 19 and 20. Under specific model-dependent conditions the most stable state predicted by GRDF models corresponds to $n_B \approx n_{sat}/2$. This situation is similar to what has been previously observed for $T = 0$ in Fig. 1. Similarly to RG(SLy4), the charge chemical potential in HS(DD2) has a complex structure at low temperatures and negative values at high temperatures. The former feature is due to shell effects in the binding energies while the second is due to the slight neutron enrichment of the gas of unbound nucleons. Information on matter composition for these models is provided in Appendix A, see Fig. 27. Given that, under all circumstances considered here, particle resonances are subdominant deviations between GRDF and HS can only be attributed to the cluster's energy functional, for which every model assumes a different density-dependence.

At least for SNA and NSE models which disregard in-medium and temperature effects on clusters energy functionals the gross of the dynamics neither of CCSN, PNS evolution nor BNS mergers is affected by modelling. There is nevertheless some influence on particular phenomena, such as those pointed out for instance for the evolution of the shock radius, the accretion rate and the properties of matter above the shock in CCSN [142,100]. The main influence of the nuclear distribution is indirect via the nuclear structure dependence of the weak interaction rates. Among others, it determines the EC capture rate during infall in a CCSN and has thus a strong impact on bounce properties [94,95,96] and early post-bounce (anti)-neutrino luminosities and spectra [183]. Light and neutron-rich nuclei were also shown to play important roles in the production of seed nuclei and r -process elements in supernovae [188]. According to [189] light nuclei in the outer layers of PNS also impact the anti-

neutrino average energies. At early moments the opacity is reduced, which results in larger average energies of the anti-neutrinos; at late moments the appearance of light nuclei has the opposite effect and it is expected to modify the nucleosynthesis occurring in neutrino-driven winds.

6 Symmetry energy at finite temperature

We have seen so far that finite temperature effects impact all thermodynamic quantities and the nucleon effective masses play a key role. This is expected to be the case of the symmetry energy, too. Symmetry energy in homogeneous matter within non-relativistic mean field models was thoroughly addressed in Ref. [190], which highlighted a number of correlations among the symmetry energy at finite temperature and the density dependence of nucleonic Landau effective masses, including the neutron-proton mass splitting. The case of warm inhomogeneous subsaturated matter was considered in Ref. [161], who have shown that - similarly to what happens in cold matter (see Sec. 3) - density dishomogeneities break the isospin invariance of the interaction and the equivalence of the two definitions of E_{sym} . Ref. [162] investigated the modifications of the (free) symmetry energy due to cluster formation, liquid-gas phase transition and Coulomb and electron corrections for $T \leq T_C$. Refs. [190] and [161] employed non-relativistic Skyrme type models for the nucleonic interactions; Ref. [162] a density-dependent CDFT model. The widest density domain, $0 < n_B \leq 1.5n_{sat}$, was considered in [190], for $5 \leq T \leq 20$ MeV. In this section we shall address the temperature dependence of the symmetry energy in stellar matter over wide ranges of temperature and density considering EoS models belonging to various classes.

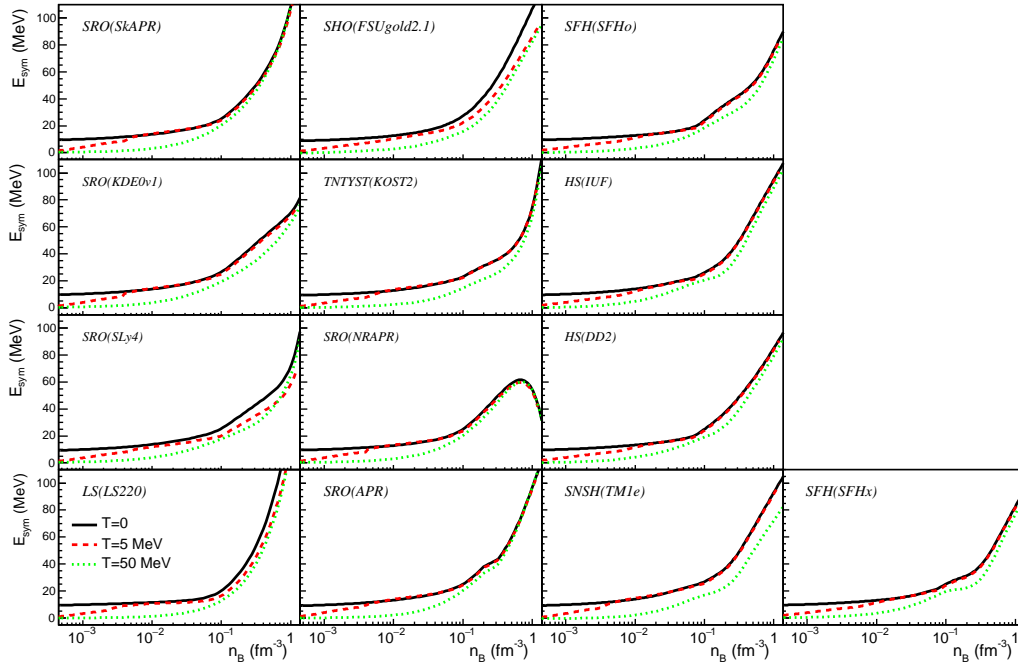


Fig. 23 Symmetry energy per baryon, defined as $E_{sym}(n_B, T) = E_{NM}(n_B, T)/A - E_{SM}(n_B, T)/A$, as function of baryon number density comparing results at $T=5$ and 50 MeV with those at $T=0$. The baryonic part of various EoS models is considered.

Fig. 23 displays the symmetry energy as function of baryon number density confronting the predictions of various EoS models at $T=5$ and 50 MeV with results at $T=0$. Two features are worth to be noticed. First, at variance with what happens in cold matter, which is inhomogeneous at sub-saturation densities (see Sec. 3.3), sufficiently hot matter is homogeneous at low densities, thus $\lim_{n_B \rightarrow 0} E_{sym} \rightarrow 0$ [161]. This implies that, for $n_B < n_t$, the symmetry energy diminishes as T increases. Second, the T -dependence of E_{sym} at high densities is not necessarily monotonic, see for instance SRO(SLy4) which, for $n_B > 0.6 \text{ fm}^{-3}$, predicts $E_{sym}(T=0) > E_{sym}(T=50 \text{ MeV}) > E_{sym}(T=5 \text{ MeV})$. Overall, the magnitude of thermal effects depends on density, temperature and EoS model, in agreement with previous conclusions in [190].

The discussion above suggests that is not straightforward to establish correlations between the parameters characterizing the symmetry energy in cold symmetric nuclear matter and the evolution of environments where hot dense matter is populated. Naturally, situations dominated by the high density part of the EoS should be more favorable to find such correlations. Indeed, in CCSN simulations as a consequence of the slower PNS contraction in EoS models with large symmetry energies, lower average neutrino energies are obtained [142,69]. In addition, convection in the new born PNS is sensitive to the symmetry energy with faster stabilisation for lower symmetry energies [191,192,193]. Loose correlations between the symmetry energy and

bounce properties have been found, too [142,69], but it should be stressed that the uncertainty on weak interaction rates from electron capture on nuclei during infall is the dominant source of uncertainty in bounce properties [95,96].

Ref. [194] investigates the possible signatures of L_{sym} in BNS mergers. They find that while the properties of the merger remnant manifest a strong sensitivity on the EoS model, GW emission and post-merger dynamics do not show any clear correlation with L_{sym} , whereas large values of L_{sym} lead to systematically enhanced ejecta, which would result in increased EM emission.

7 Properties of hot compact stars and the role of EoS

Though significant dependence on the dense matter EoS and particle degrees for freedom, in addition to initial conditions and weak interaction rates, was put forward for PNS evolution since decades [1,195], only a limited pool of EoS models has yet been considered within full numerical simulations which require a combined solution of hydrodynamics equations and neutrino transport, see e.g. [195,1,196,197,192,193]. The situation is rather similar for studies of the post-merger remnant of a BNS merger, where full-fledged hydrodynamics simulations are computationally very expensive. Many studies of the EoS and composition dependence therefore focus on stationary solutions of hot compact stars which among others can give hints on maximally supported masses and internal structure, see e.g. [198,199,200,201,

Table 5 Properties of the maximum mass configuration of spherically-symmetric non-rotating PNS with constant profiles of $(S/A, Y_e)$. Predictions of different EoS models. Listed are central baryon number density and temperature; baryonic and gravitational masses; radius.

model	$S/A = 1, Y_e = 0.4$					$S/A = 2, Y_e = 0.2$					$S/A = 1, Y_e = 0.1$				
	$n_{B,c}$ [fm $^{-3}$]	T_c [MeV]	M_B [M_\odot]	M_G [M_\odot]	R [km]	$n_{B,c}$ [fm $^{-3}$]	T_c [MeV]	M_B [M_\odot]	M_G [M_\odot]	R [km]	$n_{B,c}$ [fm $^{-3}$]	T_c [MeV]	M_B [M_\odot]	M_G [M_\odot]	R [km]
LS(LS220)	1.17	23.5	2.16	1.95	10.9	1.09	60.1	2.33	2.04	11.1	1.10	30.4	2.44	2.08	10.7
SRO(SLy4)	1.11	57.1	2.26	2.02	11.1	0.97	125.2	2.45	2.16	11.7	1.11	92.2	2.47	2.09	10.4
SRO(KDE0v1)	1.17	53.9	2.19	1.96	10.9	1.03	120.9	2.37	2.09	11.4	1.20	88.0	2.36	2.01	10.2
SRO(NRAPR)	1.13	57.7	2.23	2.00	11.1	1.01	119.7	2.38	2.10	11.6	1.20	81.7	2.32	1.99	10.2
SRO(SkAPR)	1.03	52.8	2.22	2.00	11.9	0.91	109.9	2.47	2.17	12.2	1.04	70.5	2.44	2.09	11.0
SRO(APR)	1.16	49.3	2.42	2.13	10.4	1.05	108.7	2.54	2.20	10.9	1.12	62.7	2.65	2.20	10.2
TNTYST(KOST2)	1.09	41.9	2.43	2.14	10.9	1.02	99.8	2.58	2.23	11.0	1.09	60.3	2.69	2.23	10.3
SHO(FSUgold2.1)	0.89	31.2	2.30	2.08	12.9	0.81	70.6	2.44	2.17	13.1	0.88	40.4	2.48	2.14	12.0
SNSH(TM1e)	0.86	31.7	2.33	2.10	13.0	0.79	74.0	2.49	2.20	13.2	0.87	41.8	2.52	2.16	12.1
HS(IUF)	0.96	33.0	2.12	1.93	12.5	0.89	75.4	2.26	2.02	12.7	0.98	43.5	2.28	1.98	11.5
HS(DD2)	0.83	31.3	2.69	2.37	12.7	0.79	72.2	2.79	2.42	12.8	0.84	41.1	2.89	2.42	12.0
SFH(SFHo)	1.09	32.9	2.25	2.01	11.3	1.04	75.9	2.36	2.08	11.3	1.13	43.4	2.43	2.06	10.4
SFH(SFHx)	1.04	33.7	2.32	2.07	11.6	0.96	76.6	2.45	2.15	11.7	1.03	43.8	2.53	2.14	10.9

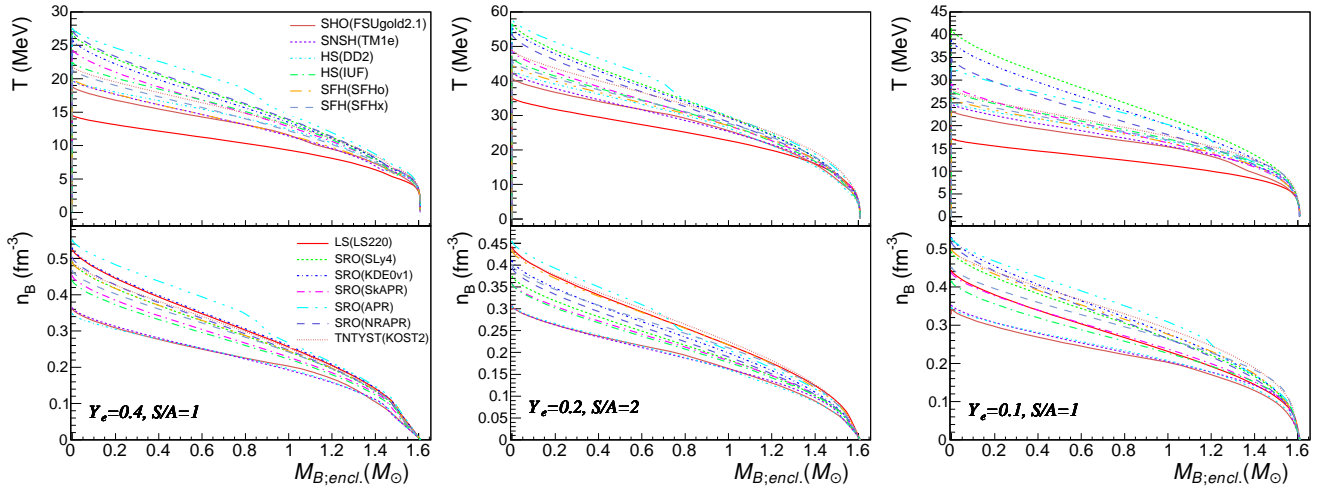


Fig. 24 Radial profiles of baryonic particle number density and temperature in spherically-symmetric non-rotating PNS with $M_B = 1.6M_\odot$ within different EoS models. The assumed constant profiles of $(S/A, Y_e)$ are representative for different instances in the evolution, see the text.

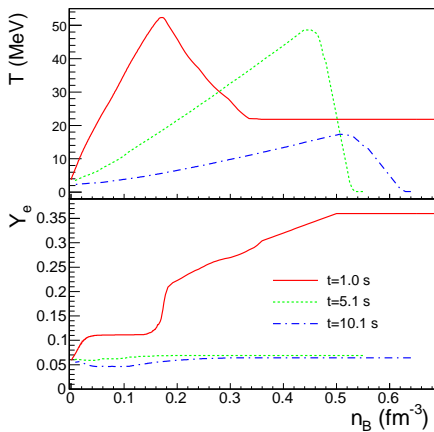


Fig. 25 $T(n_B)$ and $Y_e(n_B)$ relations used for the computation of hot star models at different instances in PNS evolution, as obtained by [193] for a star with a baryon mass of $M_B = 1.6M_\odot$ with the RG(SLy4) EoS.

202, 203, 204, 125, 205, 206, 207, 208, 209]. Profiles of entropy per baryon (or temperature) and electron/lepton fraction are thereby obtained either directly from numerical simulations at different evolution times or taken as constant with typical values.

As an application of the finite-temperature EoS discussed in the previous sections, we pursue in this direction and discuss the EoS dependence of the structure of a hot static star. As an indication, we assume constant profiles of S/A and Y_e . Three sets of values will be considered: $(S/A = 1, Y_e = 0.4)$, $(S/A = 2, Y_e = 0.2)$ and $(S/A = 1, Y_e = 0.1)$. Although over the considered time range, neutrinos are still trapped, we will not consider their contribution to the thermodynamic quantities here. The latter contribution is small and our qualitative discussion thus remains unaffected. Given the above profiles, we obtain static configurations of hot stars by solving the Tolman-Oppenheimer-Volkoff equations.

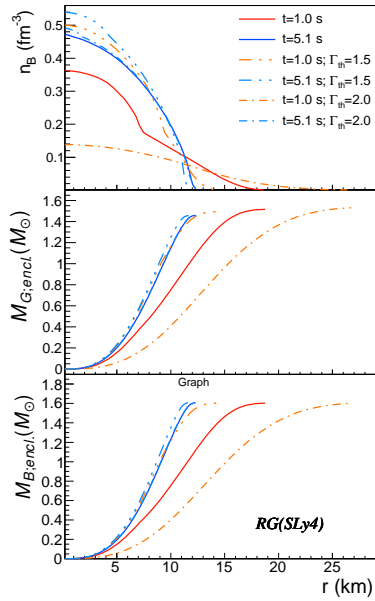


Fig. 26 Radial profiles of enclosed baryonic and gravitational masses and particle number density for a PNS with $M_B = 1.6M_\odot$ at $t = 1.0$ and 5.1 s. Exact results corresponding to RG(SLy4) are confronted with those obtained by the Γ -law, eq. (15), for $\Gamma_{th} = 1.5$ and 2.0 .

Obtained radial profiles of baryonic density and temperature, expressed in terms of enclosed baryonic mass, are plotted in fig. 24 for PNS with $M_B = 1.6M_\odot$ built upon various EoS models. Values of a few key global quantities that characterize the maximum mass configurations of hot PNS are listed in Table 5 for each EoS model and assumed thermodynamic conditions.

The predictions of different models vary widely. Temperature profiles reflect the density dependence of nucleon effective masses. LS220, for which the effective masses equal the bare masses and are thus higher than in all other models, provides the lowest temperatures. HS(DD2), SNSH(TM1e) and SHO(FSUgold2.1) provide similar particle number density profiles and, given that their effective masses are similar (see fig. 4), the temperature profiles are similar, too. For ($S/A = 1, Y_e = 0.1$) SRO(SLy4), SFHo and SRO(NRAPR) provide similar density profiles while $T(\text{SRO(SLy4)}) > T(\text{NRAPR}) > T(\text{SFHo})$; the first inequality can be explained by the fact that $m_{eff}(\text{NRAPR}) > m_{eff}(\text{SRO(SLy4)})$. For fixed values of S/A , isospin symmetric matter has lower temperatures than isospin asymmetric matter [209]. Isospin asymmetric matter allows for more massive configurations, with smaller radii, too. By comparing the configurations corresponding to ($S/A = 1, Y_e = 0.4$) and ($S/A = 2, Y_e = 0.2$) it comes out that during the early deleptonization phase, when PNS gets hotter, it expands and maximum baryonic and gravitational masses increase. During the late deleptonization phase, see ($S/A = 2, Y_e = 0.2$) and ($S/A = 1, Y_e = 0.1$), PNS shrinks.

The maximum baryon mass is an interesting quantity in the context of stability against collapse to a black hole during PNS and BNS merger evolution. In the absence of accretion, M_B is a conserved quantity during evolution, such that if it exceeds the maximum baryon mass of the cold β -equilibrated configuration, the star necessarily becomes unstable against collapse to a black hole at some point independently of the mechanism stabilising it temporarily [210]. According to Table 5 this is the case of SRO(KDE0v1), SRO(NRAPR), SRO(SkAPR), see also other examples in [209]. SRO(NRAPR) and SRO(SkAPR) have almost identical nucleon effective masses; very similar density dependencies of the symmetry energy; but different behaviors in the isoscalar channels with SRO(SkAPR) being stiffer than SRO(NRAPR). As a consequence, the radii of canonical NS and the maximum mass are slightly higher for the former. In addition, the smaller compressibility of SRO(SkAPR) leads to smaller central densities in the maximum mass neutron stars, such that it becomes more sensitive to thermal effects. Indeed fig. 24 and Table 5 show that for all considered thermodynamic conditions PNS built upon SRO(SkAPR) are more inflated than those built upon SRO(NRAPR). We note, too, that for extreme isospin asymmetries thermal energy is more effective in increasing M_G and M_B in SRO(SkAPR). Finally radial profiles of NS built upon SRO(APR) single out by a bump, due to the onset of the pion condensate.

The ability of the Γ -law to account for the structure of PNS is investigated in fig. 26, where radial profiles of baryonic density and enclosed baryonic and gravitational masses obtained using eq. (15) to account for pressure of hot matter are confronted with results taking into account the full temperature dependence of the EoS. Two different entropy per baryon and electron fraction profiles are employed, corresponding to two different post-bounce times from a simulation of PNS evolution [193], see fig. 25. The considered PNS has $M_B = 1.6M_\odot$ and the RG(SLy4) EoS model is employed, in agreement with the underlying simulation. Only the cases of $t = 1.0$ s and 5.1 s are illustrated. The results indicate that as long as stellar shells with $n_B \lesssim n_{sat}$ are hot as it is the case in the first seconds of evolution, eq. (15) does not provide a fair estimation of the exact results. Moreover, in some of the limiting cases, $\Gamma_{th} = 1.5$ and 2 encompassing the exact result, the domain they delineate is too broad to allow a satisfactory description. The performance of eq. (15) improves when the maximum of the temperature distribution moves in the innermost core and the temperature in the low density shells does not exceed 10 MeV, see the curves for $t = 5.1$ s. These results can be understood by considering that thermal effects are relatively more important in dilute matter than in dense matter, see fig. 9. To quantify the error of the Γ -law on global properties of hot PNS we specify the values of gravitational masses and radii provided by this method together with those obtained with the full temperature de-

pendent EoS: full EoS at $t=1.0$ s (5.1 s): $M_G = 1.51M_\odot$ ($1.45M_\odot$), $R = 18.8$ km (12.3 km); $\Gamma = 1.5$ at $t=1.0$ s (5.1 s): $M_G = 1.49M_\odot$ ($1.45M_\odot$), $R = 14.3$ km (11.6 km); $\Gamma = 2.0$ at $t=1.0$ s (5.1 s): $M_G = 1.53M_\odot$ ($1.45M_\odot$), $R = 27.0$ km (12.4 km). As can be seen, although at first sight the Γ -law reasonably well reproduces the star's properties and profiles at later times, quantitatively this is indeed the case only for the mass; radii, however are extremely sensitive to thermal effects, as noticed earlier, see e.g. [209, 18].

8 Summary and conclusions

We have reviewed the so-called “general purpose” equations of state available in tabular form on the COMPOSE data base. The assumptions entering the different models concerning the treatment of inhomogeneous matter, the effective interaction between baryons and the particle content have been discussed. Corresponding nuclear matter parameters and properties of cold, β -equilibrated neutron stars have been listed for all models together with existing constraints from observations and nuclear data.

We have then investigated in detail the properties of cold symmetric and pure neutron matter, including a discussion of the symmetry energy and the effective masses of nucleons within a selection of purely nucleonic models. At finite temperature we have shown the behavior of different thermodynamic quantities for the same models: thermal contributions to pressure and energy density, entropy per baryon, specific heats, sound speed, adiabatic and thermal indices. All considered quantities manifest strong sensitivity to the underlying EoS and a strong dependence on baryon number density, whereas for the considered ranges, temperature and electron fraction show less impact. For homogeneous matter, among the variables which characterize the effective interactions and the EoS, we confirm that thermal properties strongly depend on the nucleonic Landau (for non-relativistic models) and Dirac (for CDFT models) effective masses. The reason lies in the role these quantities play in the single particle energies. For non-relativistic models, where the kinetic energy strongly depends on the Landau effective mass, models with large values of $m_{eff;Landau}$ are characterized by large values of the thermal energy density and entropy per baryon.

Concerning inhomogeneous matter, differences in modelling – including the theoretical framework and the temperature and density dependence of the cluster surface energy – lead to significant differences in the various species abundances. The uncertainties in thermodynamic quantities entailed by cluster modelling are similar in magnitude to those associated to the effective interaction. The cluster energy density functionals accounting for in-medium and thermal effects are found to induce more important modifications.

The selected purely nucleonic models have been used to investigate the EoS-dependence of hot static stars with con-

stant entropy per baryon and electron fraction. The considered values correspond roughly to different instants of PNS evolution. Naturally, EoS models with smaller values of nucleon effective mass lead to hotter stars at a given entropy per baryon. Comparing two models having a similar density dependence of the effective mass, we have shown that the stiffer EoS is more sensitive to thermal effects. The reason is that the central densities inside the stars are lower.

Last but not least, we have compared the description of thermal effects via an analytic extension of the cold EoS with a Γ -law with the full solution from the finite temperature EoS. As expected from the fact that the thermal index Γ is strongly density dependent, the thermal contribution to pressure is not well reproduced by a Γ -law with constant value. Thus, this approximation to the full finite temperature EoS should be regarded with care in situations where thermal effects on the EoS are important, e.g. for the post merger BNS remnant, CCSN and the early PNS evolution. Here we should stress that thermal effects are relatively more important in dilute matter and that even for temperatures around 50 MeV, the suprasaturation matter is only moderately affected by the thermal contribution. Therefore, as we have seen, the later time evolution of a PNS, when the temperature maximum has moved to the central part, can be fairly described by such a Γ -law.

Acknowledgements The authors gratefully acknowledge discussions with Fiorella Burgio and Stefan Typel. We thank Aurélien Pascal for providing us with the profiles in fig. 25. We also thank the anonymous referee for constructive comments that significantly contributed to enhancing the manuscript's quality. A.R.R. and F.N. acknowledge support from a grant of the Ministry of Research, Innovation and Digitization, CNCS/CCCDI – UEFISCDI, Project No. PN-III-P4-ID-PCE-2020-0293, within PNCDI III. This work has been partially funded by the European COST Action CA16214 PHAROS “The multi-messenger physics and astrophysics of neutron stars”.

Data availability statement: This manuscript has no associated data as that all data are already available on the CompOSE site <https://compose.obspm.fr>.

Appendix A

References

1. J.A. Pons, S. Reddy, M. Prakash, J.M. Lattimer, J.A. Miralles, *Astrophys. J.* **513**(2), 780 (1999). DOI 10.1086/306889. URL <https://doi.org/10.1086/306889>
2. K. Sumiyoshi, S. Yamada, H. Suzuki, *Astrophys. J.* **667**(1), 382 (2007). DOI 10.1086/520876. URL <https://doi.org/10.1086/520876>
3. H.T. Janka, K. Langanke, A. Marek, G. Martinez-Pinedo, B. Mueller, *Phys. Rep.* **442**(1), 38 (2007). DOI <https://doi.org/10.1016/j.physrep.2007.02.002>. URL <http://www.sciencedirect.com/science/article/pii/S0370157307000> The Hans Bethe Centennial Volume 1906-2006
4. T. Fischer, S. Whitehouse, A. Mezzacappa, F.K. Thielemann, M. Liebendorfer, *Astronomy & Astrophysics* **499**, 1 (2009). DOI 10.1051/0004-6361/200811055

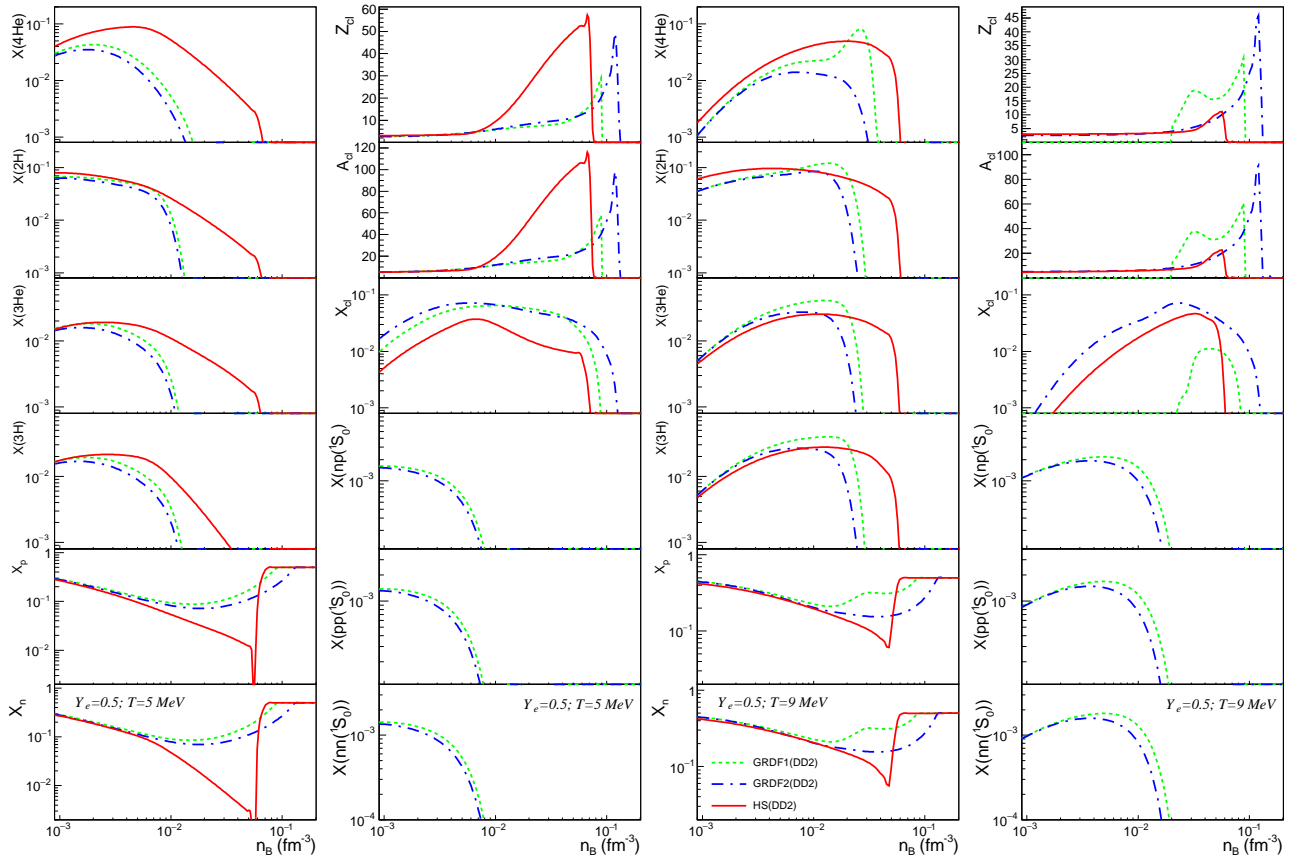


Fig. 27 Matter composition in terms of particle mass fractions and average mass and charge numbers of nuclei as predicted by HS(DD2), GRDF1(DD2) and GRDF2(DD2) for $T = 5$ MeV (first two columns) and $T = 9$ MeV (columns 3 and 4) and $Y_e = 0.5$.

5. M. Shibata, K. Taniguchi, *Living Rev.Rel.* **14**, 6 (2011). DOI 10.12942/lrr-2011-6
6. E. O'Connor, C.D. Ott, *Astrophys. J.* **730**, 70 (2011). DOI 10.1088/0004-637X/730/2/70
7. M. Hempel, T. Fischer, J. Schaffner-Bielich, M. Liebendörfer, *Astrophys. J.* **48**, 70 (2012). DOI 10.1088/0004-637X/748/1/70
8. A. Mezzacappa, E.J. Lentz, S.W. Bruenn, W.R. Hix, O.E.B. Messer, E. Endeve, J.M. Blondin, J.A. Harris, P. Marronetti, K.N. Yakunin, E.J. Lingerfelt, arXiv e-prints arXiv:1507.05680 (2015)
9. S. Rosswog, *Int. J. Mod. Phys. D* **24**, 1530012 (2015). DOI 10.1142/S0218271815300128
10. L. Baiotti, L. Rezzolla, *Rep.Prog. Phys.* **80**(9), 096901 (2017). DOI 10.1088/1361-6633/aa67bb
11. E.P. O'Connor, S.M. Couch, *Astrophys. J.* **865**(2), 81 (2018). DOI 10.3847/1538-4357/aadcf7
12. A. Burrows, D. Radice, D. Vartanyan, H. Nagakura, M.A. Skinner, J.C. Dolence, *Mon. Not. Royal Astr. Soc.* **491**(2), 2715 (2020). DOI 10.1093/mnras/stz3223
13. M. Ruiz, A. Tsokaros, S.L. Shapiro, *Phys. Rev. D* **101**(6), 064042 (2020). DOI 10.1103/PhysRevD.101.064042
14. H.T. Janka, *Ann. Rev. Nucl. Part. Sci.* **62**, 407 (2012). DOI 10.1146/annurev-nucl-102711-094901
15. A. Bauswein, H.T. Janka, K. Hebeler, A. Schwenk, *Phys. Rev. D* **86**, 063001 (2012). DOI 10.1103/PhysRevD.86.063001
16. S. Köppel, L. Bovard, L. Rezzolla, *The Astrophysical Journal* **872**(1), L16 (2019). DOI 10.3847/2041-8213/ab0210. URL <https://doi.org/10.3847/2041-8213/ab0210>
17. A. Bauswein, S. Blacker, V. Vijayan, N. Stergioulas, K. Chatziioannou, J.A. Clark, N.U.F. Bastian, D.B. Blaschke, M. Cierniak, T. Fischer, *Phys. Rev. Lett.* **125**, 141103 (2020). DOI 10.1103/PhysRevLett.125.141103. URL <https://link.aps.org/doi/10.1103/PhysRevLett.125.141103>
18. E. Preau, A. Pascal, J. Novak, M. Oertel, *Mon. Not. Roy. Astron. Soc.* **505**(1), 939 (2021). DOI 10.1093/mnras/stab1348
19. P.B. Demorest, T. Pennucci, S.M. Ransom, M.S.E. Roberts, J.W.T. Hessels, *Nature* **467**(7319), 1081 (2010). DOI 10.1038/nature09466
20. Z. Arzoumanian, et al., *Astrophys. J. Suppl.* **235**(2), 37 (2018). DOI 10.3847/1538-4365/aab5b0
21. J. Antoniadis, P.C.C. Freire, N. Wex, T.M. Tauris, R.S. Lynch, M.H. van Kerkwijk, M. Kramer, C. Bassa, V.S. Dhillon, T. Driebe, J.W.T. Hessels, V.M. Kaspi, V.I. Kondratiev, N. Langer, T.R. Marsh, M.A. McLaughlin, T.T. Pennucci, S.M. Ransom, I.H. Stairs, J. van Leeuwen, J.P.W. Verbiest, D.G. Whelan, *Science* **340**, 448 (2013). DOI 10.1126/science.1233232
22. H.T. Cromartie, et al., *Nature Astron.* **4**(1), 72 (2020). DOI 10.1038/s41550-019-0880-2
23. E. Fonseca, H.T. Cromartie, T.T. Pennucci, P.S. Ray, A.Y. Kirichenko, S.M. Ransom, P.B. Demorest, I.H. Stairs, Z. Arzoumanian, L. Guillemot, A. Parthasarathy, M. Kerr, I. Cognard, P.T. Baker, H. Blumer, P.R. Brook, M. DeCesar, T. Dolch, F.A. Dong, E.C. Ferrara, W. Fiore, N. Garver-Daniels, D.C. Good, R. Jennings, M.L. Jones, V.M. Kaspi, M.T. Lam, D.R. Lorimer, J. Luo, A. McEwen, J.W. McKee, M.A. McLaughlin, N. McMan, B.W. Meyers, A. Naidu, C. Ng, D.J. Nice, N. Pol, H.A. Radovan, B. Shapiro-Albert, C.M. Tan, S.P. Tendulkar, J.K. Swiggum, H.M. Wahl, W.W. Zhu, *The Astrophysical Journal Letters* **915**(1), L12 (2021). DOI 10.3847/2041-8213/ac03b8. URL <https://doi.org/10.3847/2041-8213/ac03b8>

24. R.W. Romani, D. Kandel, A.V. Filippenko, T.G. Brink, W. Zheng, *The Astrophysical Journal* **908**(2), L46 (2021). DOI 10.3847/2041-8213/abe2b4. URL <https://doi.org/10.3847/2041-8213/abe2b4>
25. S. Weissenborn, D. Chatterjee, J. Schaffner-Bielich, *Phys. Rev. C* **85**, 065802 (2012). DOI 10.1103/PhysRevC.85.065802
26. S. Weissenborn, D. Chatterjee, J. Schaffner-Bielich, *Nucl. Phys. A* **881**, 62 (2012). DOI 10.1016/j.nuclphysa.2012.02.012
27. L. Bonanno, A. Sedrakian, *Astron. Astrophys.* **539**, A16 (2012). DOI 10.1051/0004-6361/201117832. URL <http://adsabs.harvard.edu/abs/2012A%26A...539A...16B>
28. T. Miyatsu, M.K. Cheoun, K. Saito, *Phys. Rev. C* **88**, 015802 (2013). DOI 10.1103/PhysRevC.88.015802. URL <https://link.aps.org/doi/10.1103/PhysRevC.88.015802>
29. G. Colucci, A. Sedrakian, *Phys. Rev. C* **87**, 055806 (2013). DOI 10.1103/PhysRevC.87.055806. URL <https://link.aps.org/doi/10.1103/PhysRevC.87.055806>
30. M. Oertel, C. Providência, F. Gulminelli, A.R. Raduta, *J. Phys. G* **42**(7), 075202 (2015). DOI 10.1088/0954-3899/42/7/075202
31. D. Chatterjee, I. Vidaña, *Eur. Phys. J. A* **52**(2), 29 (2016). DOI 10.1140/epja/i2016-16029-x
32. M. Fortin, C. Providência, A.R. Raduta, F. Gulminelli, J.L. Zdunik, P. Haensel, M. Bejger, *Phys. Rev. C* **94**, 035804 (2016). DOI 10.1103/PhysRevC.94.035804. URL <https://link.aps.org/doi/10.1103/PhysRevC.94.035804>
33. M. Fortin, S.S. Avancini, C. Providência, I. Vidaña, *Phys. Rev. C* **95**(6), 065803 (2017). DOI 10.1103/PhysRevC.95.065803
34. J.J. Li, A. Sedrakian, F. Weber, *Phys. Lett. B* **783**, 234 (2018). DOI 10.1016/j.physletb.2018.06.051
35. A. Drago, A. Lavagno, G. Pagliara, D. Pigato, *Phys. Rev. C* **90**, 065809 (2014). DOI 10.1103/PhysRevC.90.065809. URL <https://link.aps.org/doi/10.1103/PhysRevC.90.065809>
36. B.J. Cai, F.J. Fattoyev, B.A. Li, W.G. Newton, *Phys. Rev. C* **92**, 015802 (2015). DOI 10.1103/PhysRevC.92.015802. URL <https://link.aps.org/doi/10.1103/PhysRevC.92.015802>
37. E. Kolomeitsev, K. Maslov, D. Voskresensky, *Nuclear Physics A* **961**, 106 (2017). DOI <https://doi.org/10.1016/j.nuclphysa.2017.02.004>. URL <http://www.sciencedirect.com/science/article/pii/S03759474171300295>
38. H.S. Sahoo, G. Mitra, R. Mishra, P.K. Panda, B.A. Li, *Phys. Rev. C* **98**, 045801 (2018). DOI 10.1103/PhysRevC.98.045801. URL <https://link.aps.org/doi/10.1103/PhysRevC.98.045801>
39. P. Ribes, A. Ramos, L. Tolos, C. Gonzalez-Boquera, M. Centelles, *ApJ* **883**, 168 (2019). DOI 10.3847/1538-4357/ab3a93
40. A.R. Raduta, *Phys. Lett. B* **814**, 136070 (2021). DOI 10.1016/j.physletb.2021.136070
41. T. Malik, S. Banik, D. Bandyopadhyay, *The European Physical Journal Special Topics* **230**, 561 (2021). DOI 10.1140/epjs/s11734-021-00006-2
42. V.B. Thapa, M. Sinha, J.J. Li, A. Sedrakian, *Phys. Rev. D* **103**, 063004 (2021). DOI 10.1103/PhysRevD.103.063004. URL <https://link.aps.org/doi/10.1103/PhysRevD.103.063004>
43. S. Weissenborn, I. Sagert, G. Pagliara, M. Hempel, J. Schaffner-Bielich, *The Astrophysical Journal Letters* **740**(1), L14 (2011). URL <http://stacks.iop.org/2041-8205/740/i=1/a=L14>
44. J.L. Zdunik, P. Haensel, *Astron. Astrophys.* **551**, A61 (2013). DOI 10.1051/0004-6361/201220697
45. M.G. Alford, S. Han, M. Prakash, *Phys. Rev. D* **88**, 083013 (2013). DOI 10.1103/PhysRevD.88.083013. URL <https://link.aps.org/doi/10.1103/PhysRevD.88.083013>
46. D. Alvarez-Castillo, A. Ayriyan, S. Benic, D. Blaschke, H. Grigorian, S. Typel, *Eur. Phys. J. A* **52**(3), 69 (2016). DOI 10.1140/epja/i2016-16069-2
47. M.A.R. Kaltentborn, N.U.F. Bastian, D.B. Blaschke, *Phys. Rev. D* **96**, 056024 (2017). DOI 10.1103/PhysRevD.96.056024. URL <https://link.aps.org/doi/10.1103/PhysRevD.96.056024>
48. G. Montaña, L. Tolós, M. Hanuske, L. Rezzolla, *Phys. Rev. D* **99**, 103009 (2019). DOI 10.1103/PhysRevD.99.103009. URL <https://link.aps.org/doi/10.1103/PhysRevD.99.103009>
49. K. Otto, M. Oertel, B.J. Schaefer, *Phys. Rev. D* **101**(10), 103021 (2020). DOI 10.1103/PhysRevD.101.103021
50. K. Otto, M. Oertel, B.J. Schaefer, *Eur. Phys. J. ST* **229**(22-23), 3629 (2020). DOI 10.1140/epjst/e2020-000155-y
51. B.P. Abbott, et al., *Phys. Rev. Lett.* **119**, 161101 (2017). DOI 10.1103/PhysRevLett.119.161101. URL <https://link.aps.org/doi/10.1103/PhysRevLett.119.161101>
52. B.P. Abbott, et al., *The Astrophysical Journal Letters* **848**(2), L12 (2017). DOI 10.3847/2041-8213/aa91c9
53. B. Abbott, et al., *Phys. Rev. X* **9**(1), 011001 (2019). DOI 10.1103/PhysRevX.9.011001
54. M.C. Miller, et al., *ApJ Lett.* **887**, L24 (2019). DOI 10.3847/2041-8213/ab50c5
55. T.E. Riley, et al., *ApJ Lett.* **887**, L21 (2019). DOI 10.3847/2041-8213/ab481c
56. M.C. Miller, F.K. Lamb, A.J. Dittmann, S. Bogdanov, Z. Arzoumanian, K.C. Gendreau, S. Guillot, W.C.G. Ho, J.M. Lattimer, M. Loewenstein, S.M. Morsink, P.S. Ray, M.T. Wolff, C.L. Baker, T. Cazeau, S. Manthripragada, C.B. Markwardt, T. Okajima, S. Pollard, I. Cognard, H.T. Cromartie, E. Fonseca, L. Guillemot, M. Kerr, A. Parthasarathy, T.T. Pennucci, S. Ransom, I. Stairs, *The Astrophysical Journal Letters* **918**(2), L28 (2021). DOI 10.3847/2041-8213/ac089b. URL <https://doi.org/10.3847/2041-8213/ac089b>
57. T.E. Riley, A.L. Watts, P.S. Ray, S. Bogdanov, S. Guillot, S.M. Morsink, A.V. Bilous, Z. Arzoumanian, D. Choudhury, J.S. Deneva, K.C. Gendreau, A.K. Harding, W.C.G. Ho, J.M. Lattimer, M. Loewenstein, R.M. Ludlam, C.B. Markwardt, T. Okajima, C. Prescod-Weinstein, R.A. Remillard, M.T. Wolff, E. Fonseca, H.T. Cromartie, M. Kerr, T.T. Pennucci, A. Parthasarathy, S. Ransom, I. Stairs, L. Guillemot, I. Cognard, *The Astrophysical Journal Letters* **918**(2), L27 (2021). DOI 10.3847/2041-8213/ac0a81. URL <https://doi.org/10.3847/2041-8213/ac0a81>
58. G. Raaijmakers, S.K. Greif, K. Hebeler, T. Hinderer, S. Nissanke, T.E. Riley, A.L. Watts, J.M. Lattimer, W.C.G. Ho, *The Astrophysical Journal Letters* **918**(2), L29 (2021). DOI 10.3847/2041-8213/ac089a. URL <https://doi.org/10.3847/2041-8213/ac089a>
59. B. Margalit, B.D. Metzger, *Astrophys. J. Lett.* **850**(2), L19 (2017). DOI 10.3847/2041-8213/aa991c
60. M. Ruiz, S.L. Shapiro, A. Tsokaros, *Phys. Rev. D* **97**(2), 021501 (2018). DOI 10.1103/PhysRevD.97.021501
61. L. Rezzolla, E.R. Most, L.R. Weih, *The Astrophysical Journal* **852**(2), L25 (2018). DOI 10.3847/2041-8213/aaa401. URL <http://dx.doi.org/10.3847/2041-8213/aaa401>
62. M. Shibata, E. Zhou, K. Kiuchi, S. Fujibayashi, *Phys. Rev. D* **100**(2), 023015 (2019). DOI 10.1103/PhysRevD.100.023015
63. S. Khadkikar, A.R. Raduta, M. Oertel, A. Sedrakian, *Phys. Rev. C* **103**, 055811 (2021). DOI 10.1103/PhysRevC.103.055811. URL <https://link.aps.org/doi/10.1103/PhysRevC.103.055811>
64. J. Margueron, R. Hoffmann Casali, F. Gulminelli, *Phys. Rev. C* **97**(2), 025806 (2018). DOI 10.1103/PhysRevC.97.025806
65. J.J. Li, A. Sedrakian, *Phys. Rev. C* **100**(1), 015809 (2019). DOI 10.1103/PhysRevC.100.015809
66. S. Traversi, P. Char, G. Pagliara, *Astrophys. J.* **897**, 165 (2020). DOI 10.3847/1538-4357/ab99c1
67. C. Constantinou, B. Muccioli, M. Prakash, J.M. Lattimer, *Phys. Rev. C* **89**, 065802 (2014). DOI 10.1103/PhysRevC.89.065802. URL <https://link.aps.org/doi/10.1103/PhysRevC.89.065802>
68. C. Constantinou, B. Muccioli, M. Prakash, J.M. Lattimer, *Phys. Rev. C* **92**, 025801 (2015).

- DOI 10.1103/PhysRevC.92.025801. URL <https://link.aps.org/doi/10.1103/PhysRevC.92.025801>
69. A.S. Schneider, L.F. Roberts, C.D. Ott, E. O'Connor, Phys. Rev. C **100**, 055802 (2019). DOI 10.1103/PhysRevC.100.055802. URL <https://link.aps.org/doi/10.1103/PhysRevC.100.055802>
70. A. Schneider, E. O'Connor, E. Granqvist, A. Betranhandy, S. Couch, Astrophys. J. **894**(1), 4 (2020). DOI 10.3847/1538-4357/ab8308
71. H. Yasin, S. Schäfer, A. Arcones, A. Schwenk, Phys. Rev. Lett. **124**, 092701 (2020). DOI 10.1103/PhysRevLett.124.092701. URL <https://link.aps.org/doi/10.1103/PhysRevLett.124.092701>
72. C.A. Raithel, V. Paschalidis, F. Özel, Phys. Rev. D **104**, 063016 (2021). DOI 10.1103/PhysRevD.104.063016. URL <https://link.aps.org/doi/10.1103/PhysRevD.104.063016>
73. O.E. Andersen, S. Zha, A. da Silva Schneider, A. Betranhandy, S.M. Couch, E.P. O'Connor, arXiv e-prints arXiv:2106.09734 (2021). URL <https://arxiv.org/abs/2106.09734>
74. S. Typel, M. Oertel, T. Klähn, Phys. Part. Nucl. **46**(4), 633 (2015). DOI 10.1134/S1063779615040061
75. K. Hotokezaka, K. Kiuchi, K. Kyutoku, T. Muranushi, Y.i. Sekiguchi, M. Shibata, K. Taniguchi, Phys. Rev. D **88**, 044026 (2013). DOI 10.1103/PhysRevD.88.044026. URL <https://link.aps.org/doi/10.1103/PhysRevD.88.044026>
76. A. Bauswein, H.T. Janka, R. Oechslin, Phys. Rev. D **82**, 084043 (2010). DOI 10.1103/PhysRevD.82.084043. URL <https://link.aps.org/doi/10.1103/PhysRevD.82.084043>
77. A. Endrizzi, D. Logoteta, B. Giacomazzo, I. Bombaci, W. Kastaun, R. Ciolfi, Phys. Rev. D **98**, 043015 (2018). DOI 10.1103/PhysRevD.98.043015. URL <https://link.aps.org/doi/10.1103/PhysRevD.98.043015>
78. G. Camelio, T. Dietrich, M. Marques, S. Rosswog, Phys. Rev. D **100**(12), 123001 (2019). DOI 10.1103/PhysRevD.100.123001
79. M. Oertel, M. Hempel, T. Klähn, S. Typel, Rev. Mod. Phys. **89**(1), 015007 (2017). DOI 10.1103/RevModPhys.89.015007
80. G. Fiorella Burgio, A.F. Fantina, Astrophys. Space Sci. Libr. **457**, 255 (2018). DOI 10.1007/978-3-319-97616-7_6
81. M. Dutra, O. Lourenço, J.S. Sá Martins, A. Delfino, J.R. Stone, P.D. Stevenson, Phys. Rev. C **85**, 035201 (2012). DOI 10.1103/PhysRevC.85.035201. URL <https://link.aps.org/doi/10.1103/PhysRevC.85.035201>
82. E. Chabanat, P. Bonche, P. Haensel, J. Meyer, R. Schaeffer, Nuclear Physics A **635**(1), 231 (1998). DOI [https://doi.org/10.1016/S0375-9474\(98\)00180-8](https://doi.org/10.1016/S0375-9474(98)00180-8). URL <https://www.sciencedirect.com/science/article/pii/S0375947498001808>
83. M. Dutra, O. Lourenço, S.S. Avancini, B.V. Carlson, A. Delfino, D.P. Menezes, C. Providencia, S. Typel, J.R. Stone, Phys. Rev. C **90**(5), 055203 (2014). DOI 10.1103/PhysRevC.90.055203
84. V. Dexheimer, S. Schramm, The Astrophysical Journal **683**(2), 943 (2008). DOI 10.1086/589735. URL <https://doi.org/10.1086/589735>
85. V. Dexheimer, Publications of the Astronomical Society of Australia **34** (2017). DOI 10.1017/pasa.2017.61. URL <http://dx.doi.org/10.1017/pasa.2017.61>
86. A. Akmal, V.R. Pandharipande, D.G. Ravenhall, Phys. Rev. C **58**, 1804 (1998). DOI 10.1103/PhysRevC.58.1804. URL <https://link.aps.org/doi/10.1103/PhysRevC.58.1804>
87. A. Akmal, V.R. Pandharipande, Phys. Rev. C **56**, 2261 (1997). DOI 10.1103/PhysRevC.56.2261. URL <https://link.aps.org/doi/10.1103/PhysRevC.56.2261>
88. R.B. Wiringa, V.G.J. Stoks, R. Schiavilla, Phys. Rev. C **51**, 38 (1995). DOI 10.1103/PhysRevC.51.38. URL <https://link.aps.org/doi/10.1103/PhysRevC.51.38>
89. J. Carlson, V.R. Pandharipande, R.B. Wiringa, Nucl. Phys. A **401**, 59 (1983). DOI 10.1016/0375-9474(83)90336-6
90. B.S. Pudliner, V.R. Pandharipande, J. Carlson, R.B. Wiringa, Phys. Rev. Lett. **74**, 4396 (1995). DOI 10.1103/PhysRevLett.74.4396. URL <https://link.aps.org/doi/10.1103/PhysRevLett.74.4396>
91. H. Kanzawa, K. Oyamatsu, K. Sumiyoshi, M. Takano, Nuclear Physics A **791**(1), 232 (2007). DOI <https://doi.org/10.1016/j.nuclphysa.2007.01.098>. URL <https://www.sciencedirect.com/science/article/pii/S0375947407001098>
92. H. Togashi, K. Nakazato, Y. Takehara, S. Yamamuro, H. Suzuki, M. Takano, Nuclear Physics A **961**, 78 (2017). DOI <https://doi.org/10.1016/j.nuclphysa.2017.02.010>. URL <https://www.sciencedirect.com/science/article/pii/S0375947417300100>
93. A. Burrows, J.M. Lattimer, Astrophys. J. **285**, 294 (1984). DOI 10.1086/162505
94. W.R. Hix, O.E.B. Messer, A. Mezzacappa, M. Liebendoerfer, J. Sampaio, K. Langanke, D.J. Dean, G. Martinez-Pinedo, Phys. Rev. Lett. **91**, 201102 (2003). DOI 10.1103/PhysRevLett.91.201102
95. C. Sullivan, E. O'Connor, R.G.T. Zegers, T. Grubb, S.M. Austin, Astrophys. J. **816**(1), 44 (2016). DOI 10.3847/0004-637X/816/1/44
96. A. Pascal, S. Giraud, A.F. Fantina, F. Gulminelli, J. Novak, M. Oertel, A.R. Raduta, Phys. Rev. C **101**(1), 015803 (2020). DOI 10.1103/PhysRevC.101.015803
97. J.M. Lattimer, D.F. Swesty, Nucl. Phys. A **535**(2), 331 (1991). DOI 10.1016/0375-9474(91)90452-C
98. M. Oertel, A.F. Fantina, J. Novak, Phys. Rev. C **85**, 055806 (2012). DOI 10.1103/PhysRevC.85.055806. URL <https://link.aps.org/doi/10.1103/PhysRevC.85.055806>
99. B. Peres, M. Oertel, J. Novak, Phys. Rev. D **87**(4), 043006 (2013). DOI 10.1103/PhysRevD.87.043006
100. A.S. Schneider, L.F. Roberts, C.D. Ott, Phys. Rev. C **96**, 065802 (2017). DOI 10.1103/PhysRevC.96.065802. URL <https://link.aps.org/doi/10.1103/PhysRevC.96.065802>
101. A.S. Schneider, C. Constantinou, B. Muccioli, M. Prakash, Phys. Rev. C **100**(2), 025803 (2019). DOI 10.1103/PhysRevC.100.025803
102. H. Shen, H. Toki, K. Oyamatsu, K. Sumiyoshi, Progress of Theoretical Physics **100**(5), 1013 (1998). DOI 10.1143/PTP.100.1013. URL <https://doi.org/10.1143/PTP.100.1013>
103. H. Shen, H. Toki, K. Oyamatsu, K. Sumiyoshi, Nuclear Physics A **637**(3), 435 (1998). DOI [https://doi.org/10.1016/S0375-9474\(98\)00236-X](https://doi.org/10.1016/S0375-9474(98)00236-X). URL <https://www.sciencedirect.com/science/article/pii/S037594749800236X>
104. Y. Sugahara, H. Toki, Nuclear Physics A **579**(3), 557 (1994). DOI [https://doi.org/10.1016/0375-9474\(94\)90923-7](https://doi.org/10.1016/0375-9474(94)90923-7). URL <https://www.sciencedirect.com/science/article/pii/0375947494909237>
105. H. Shen, F. Ji, J. Hu, K. Sumiyoshi, Astrophys. J. **891**, 148 (2020). DOI 10.3847/1538-4357/ab72fd
106. K. Sumiyoshi, K. Nakazato, H. Suzuki, J. Hu, H. Shen, Astrophys. J. **887**, 110 (2019). DOI 10.3847/1538-4357/ab5443
107. C. Ishizuka, A. Ohnishi, K. Tsubakihara, K. Sumiyoshi, S. Yamada, Journal of Physics G: Nuclear and Particle Physics **35**(8), 085201 (2008). DOI 10.1088/0954-3899/35/8/085201. URL <https://doi.org/10.1088/0954-3899/35/8/085201>
108. I. Sagert, T. Fischer, M. Hempel, G. Pagliara, J. Schaffner-Bielich, A. Mezzacappa, F.K. Thielemann, M. Liebendörfer, Phys. Rev. Lett. **102**, 081101 (2009). DOI 10.1103/PhysRevLett.102.081101. URL <https://link.aps.org/doi/10.1103/PhysRevLett.102.081101>
109. I. Sagert, T. Fischer, M. Hempel, G. Pagliara, J. Schaffner-Bielich, F.K. Thielemann, M. Liebendörfer, Journal of Physics G: Nuclear and Particle Physics **37**(9), 094064 (2010). DOI 10.1088/0954-3899/37/9/094064. URL <https://doi.org/10.1088/0954-3899/37/9/094064>

110. T. Fischer, I. Sagert, G. Pagliara, M. Hempel, J. Schaffner-Bielich, T. Rauscher, F.K. Thielemann, R. Kappeli, G. Martinez-Pinedo, M. Liebendorfer, *Astrophys. J. Suppl.* **194**, 39 (2011). DOI 10.1088/0067-0049/194/2/39
111. S. Furusawa, S. Yamada, K. Sumiyoshi, H. Suzuki, *Astrophys. J.* **738**, 178 (2011). DOI 10.1088/0004-637X/738/2/178
112. S. Furusawa, K. Sumiyoshi, S. Yamada, H. Suzuki, *Astrophys. J.* **772**, 95 (2013). DOI 10.1088/0004-637X/772/2/95
113. S. Furusawa, K. Sumiyoshi, S. Yamada, H. Suzuki, *Nucl. Phys. A* **957**, 188 (2017). DOI 10.1016/j.nuclphysa.2016.09.002
114. S. Furusawa, H. Togashi, H. Nagakura, K. Sumiyoshi, S. Yamada, H. Suzuki, M. Takano, *Journal of Physics G: Nuclear and Particle Physics* **44**(9), 094001 (2017). DOI 10.1088/1361-6471/aa7f35. URL <https://doi.org/10.1088/1361-6471/aa7f35>
115. M. Wang, G. Audi, A.H. Wapstra, F.G. Kondev, M. MacCormick, X. Xu, B. Pfeiffer, *Chin. Phys. C* **36**(12), 1603 (2012). DOI 10.1088/1674-1137/36/12/003
116. S. Typel, G. Röpke, T. Klähn, D. Blaschke, H.H. Wolter, *Phys. Rev. C* **81**, 015803 (2010). DOI 10.1103/PhysRevC.81.015803. URL <https://link.aps.org/doi/10.1103/PhysRevC.81.015803>
117. G. Shen, C.J. Horowitz, S. Teige, *Phys. Rev. C* **82**, 015806 (2010). DOI 10.1103/PhysRevC.82.015806. URL <https://link.aps.org/doi/10.1103/PhysRevC.82.015806>
118. G. Shen, C.J. Horowitz, S. Teige, *Phys. Rev. C* **82**, 045802 (2010). DOI 10.1103/PhysRevC.82.045802. URL <https://link.aps.org/doi/10.1103/PhysRevC.82.045802>
119. G. Shen, C.J. Horowitz, S. Teige, *Phys. Rev. C* **83**, 035802 (2011). DOI 10.1103/PhysRevC.83.035802. URL <https://link.aps.org/doi/10.1103/PhysRevC.83.035802>
120. G. Shen, C.J. Horowitz, E. O'Connor, *Phys. Rev. C* **83**, 065808 (2011). DOI 10.1103/PhysRevC.83.065808. URL <https://link.aps.org/doi/10.1103/PhysRevC.83.065808>
121. G.A. Lalazissis, J. König, P. Ring, *Phys. Rev. C* **55**, 540 (1997). DOI 10.1103/PhysRevC.55.540. URL <https://link.aps.org/doi/10.1103/PhysRevC.55.540>
122. B.G. Todd-Rutel, J. Piekarewicz, *Phys. Rev. Lett.* **95**, 122501 (2005). DOI 10.1103/PhysRevLett.95.122501. URL <https://link.aps.org/doi/10.1103/PhysRevLett.95.122501>
123. M. Hempel, J. Schaffner-Bielich, *Nucl. Phys. A* **837**, 210 (2010). DOI 10.1016/j.nuclphysa.2010.02.010
124. S. Banik, M. Hempel, D. Bandyopadhyay, *The Astrophysical Journal Supplement Series* **214**(2), 22 (2014). DOI 10.1088/0067-0049/214/2/22. URL <https://doi.org/10.1088/0067-0049/214/2/22>
125. M. Marques, M. Oertel, M. Hempel, J. Novak, *Phys. Rev. C* **96**, 045806 (2017). DOI 10.1103/PhysRevC.96.045806. URL <https://link.aps.org/doi/10.1103/PhysRevC.96.045806>
126. M. Fortin, M. Oertel, C. Providência, *Publ. Astron. Soc. Austral.* **35**, 44 (2018). DOI 10.1017/pasa.2018.32
127. N.U.F. Bastian, *Phys. Rev. D* **103**, 023001 (2021). DOI 10.1103/PhysRevD.103.023001. URL <https://link.aps.org/doi/10.1103/PhysRevD.103.023001>
128. G. Röpke, *Phys. Rev. C* **79**, 014002 (2009). DOI 10.1103/PhysRevC.79.014002. URL <https://link.aps.org/doi/10.1103/PhysRevC.79.014002>
129. S. Typel, *Journal of Physics G: Nuclear and Particle Physics* **45**(11), 114001 (2018). DOI 10.1088/1361-6471/aadea5. URL <https://doi.org/10.1088/1361-6471/aadea5>
130. F. Gulminelli, A.R. Raduta, *Phys. Rev. C* **92**(5), 055803 (2015). DOI 10.1103/PhysRevC.92.055803
131. A.R. Raduta, F. Gulminelli, *Nucl. Phys. A* **983**, 252 (2019). DOI 10.1016/j.nuclphysa.2018.11.003
132. P. Danielewicz, J. Lee, *Nuclear Physics A* **818**(1), 36 (2009). DOI <https://doi.org/10.1016/j.nuclphysa.2008.11.007>. URL <https://www.sciencedirect.com/science/article/pii/S0375947408007926>
133. J. Duflo, A. Zuker, *Phys. Rev. C* **52**, R23 (1995). DOI 10.1103/PhysRevC.52.R23. URL <https://link.aps.org/doi/10.1103/PhysRevC.52.R23>
134. J. Negele, D. Vautherin, *Nuclear Physics A* **207**(2), 298 (1973). DOI [https://doi.org/10.1016/0375-9474\(73\)90349-7](https://doi.org/10.1016/0375-9474(73)90349-7). URL <https://www.sciencedirect.com/science/article/pii/0375947473903497>
135. P. Haensel, J.L. Zdunik, J. Dobaczewski, *Astronomy and Astrophysics* **222**(1-2), 353 (1989)
136. V. Dexheimer, R. Negreiros, S. Schramm, *Phys. Rev. C* **92**, 012801 (2015). DOI 10.1103/PhysRevC.92.012801. URL <https://link.aps.org/doi/10.1103/PhysRevC.92.012801>
137. P. Moller, J.R. Nix, W.D. Myers, W.J. Swiatecki, *Atom. Data Nucl. Data Tabl.* **59**, 185 (1995). DOI 10.1006/adnd.1995.1002
138. G. Lalazissis, S. Raman, P. Ring, *Atomic Data and Nuclear Data Tables* **71**(1), 1 (1999). DOI <https://doi.org/10.1006/adnd.1998.0795>. URL <https://www.sciencedirect.com/science/article/pii/S0092640X9890007>
139. L. Geng, H. Toki, J. Meng, *Progress of Theoretical Physics* **113**(4), 785 (2005). DOI 10.1143/PTP.113.785. URL <https://doi.org/10.1143/PTP.113.785>
140. G. Audi, A.H. Wapstra, C. Thibault, *Nucl. Phys. A* **729**(1), 337 (2003). DOI 10.1016/j.nuclphysa.2003.11.003
141. X. Roca-Maza, J. Piekarewicz, *Phys. Rev. C* **78**, 025807 (2008). DOI 10.1103/PhysRevC.78.025807. URL <https://link.aps.org/doi/10.1103/PhysRevC.78.025807>
142. A.W. Steiner, M. Hempel, T. Fischer, *The Astrophysical Journal* **774**(1), 17 (2013). DOI 10.1088/0004-637x/774/1/17. URL <https://doi.org/10.1088/0004-637x/774/1/17>
143. M. Wang, G. Audi, F.G. Kondev, W. Huang, S. Naimi, X. Xu, *Chinese Physics C* **41**(3), 030003 (2017). DOI 10.1088/1674-1137/41/3/030003. URL <https://doi.org/10.1088/1674-1137/41/3/030003>
144. A. Bauswein, N.U.F. Bastian, D.B. Blaschke, K. Chatziioannou, J.A. Clark, T. Fischer, M. Oertel, *Phys. Rev. Lett.* **122**, 061102 (2019). DOI 10.1103/PhysRevLett.122.061102. URL <https://link.aps.org/doi/10.1103/PhysRevLett.122.061102>
145. J. Margueron, R. Hoffmann Casali, F. Gulminelli, *Phys. Rev. C* **97**(2), 025805 (2018). DOI 10.1103/PhysRevC.97.025805
146. E. Khan, J. Margueron, *Phys. Rev. Lett.* **109**, 092501 (2012). DOI 10.1103/PhysRevLett.109.092501
147. Lattimer, James M., Steiner, Andrew W., *Eur. Phys. J. A* **50**(2), 40 (2014). DOI 10.1140/epja/i2014-14040-y. URL <https://doi.org/10.1140/epja/i2014-14040-y>
148. B.A. Li, B.J. Cai, W.J. Xie, N.B. Zhang, *Universe* **7**(6) (2021). DOI 10.3390/universe7060182. URL <https://www.mdpi.com/2218-1997/7/6/182>
149. B.T. Reed, F.J. Fattoyev, C.J. Horowitz, J. Piekarewicz, *Phys. Rev. Lett.* **126**, 172503 (2021). DOI 10.1103/PhysRevLett.126.172503. URL <https://link.aps.org/doi/10.1103/PhysRevLett.126.172503>
150. Shlomo, S., Kolomietz, V. M., Cold, G., *Eur. Phys. J. A* **30**(1), 23 (2006). DOI 10.1140/epja/i2006-10100-3. URL <https://doi.org/10.1140/epja/i2006-10100-3>
151. B.K. Agrawal, S. Shlomo, V.K. Au, *Phys. Rev. C* **72**, 014310 (2005). DOI 10.1103/PhysRevC.72.014310. URL <https://link.aps.org/doi/10.1103/PhysRevC.72.014310>
152. L.G. Cao, U. Lombardo, C.W. Shen, N.V. Giai, *Phys. Rev. C* **73**, 014313 (2006). DOI 10.1103/PhysRevC.73.014313. URL <https://link.aps.org/doi/10.1103/PhysRevC.73.014313>
153. A. Steiner, M. Prakash, J. Lattimer, P. Ellis, *Physics Reports* **411**(6), 325 (2005). DOI <https://doi.org/10.1016/j.physrep.2005.02.004>. URL <https://www.sciencedirect.com/science/article/pii/S0370157305001001>
154. S.S. Bao, J.N. Hu, Z.W. Zhang, H. Shen, *Phys. Rev. C* **90**, 045802 (2014). DOI 10.1103/PhysRevC.90.045802. URL <https://link.aps.org/doi/10.1103/PhysRevC.90.045802>

155. H. Toki, D. Hirata, Y. Sugahara, K. Sumiyoshi, I. Tanihata, *Nuclear Physics A* **588**(1), c357 (1995). DOI [https://doi.org/10.1016/0375-9474\(95\)00161-S](https://doi.org/10.1016/0375-9474(95)00161-S). URL <https://www.sciencedirect.com/science/article/pii/S037594749500161S>. Proceedings of the Fifth International Symposium on Physics of Unstable Nuclei
156. F.J. Fattoyev, C.J. Horowitz, J. Piekarewicz, G. Shen, *Phys. Rev. C* **82**, 055803 (2010). DOI [10.1103/PhysRevC.82.055803](https://doi.org/10.1103/PhysRevC.82.055803). URL <https://link.aps.org/doi/10.1103/PhysRevC.82.055803>
157. J. Piekarewicz, M. Centelles, *Phys. Rev. C* **79**, 054311 (2009). DOI [10.1103/PhysRevC.79.054311](https://doi.org/10.1103/PhysRevC.79.054311). URL <https://link.aps.org/doi/10.1103/PhysRevC.79.054311>
158. L.W. Chen, B.J. Cai, C.M. Ko, B.A. Li, C. Shen, J. Xu, *Phys. Rev. C* **80**, 014322 (2009). DOI [10.1103/PhysRevC.80.014322](https://doi.org/10.1103/PhysRevC.80.014322). URL <https://link.aps.org/doi/10.1103/PhysRevC.80.014322>
159. S. Typel. private com.
160. C. Drischler, K. Hebeler, A. Schwenk, *Phys. Rev. C* **93**(5), 054314 (2016). DOI [10.1103/PhysRevC.93.054314](https://doi.org/10.1103/PhysRevC.93.054314)
161. Raduta, Ad. R., Aymard, F., Gulminelli, F., *Eur. Phys. J. A* **50**(2), 24 (2014). DOI [10.1140/epja/i2014-14024-y](https://doi.org/10.1140/epja/i2014-14024-y). URL <https://doi.org/10.1140/epja/i2014-14024-y>
162. Typel, S., Wolter, H. H., Röpke, G., Blaschke, D., *Eur. Phys. J. A* **50**(2), 17 (2014). DOI [10.1140/epja/i2014-14017-x](https://doi.org/10.1140/epja/i2014-14017-x). URL <https://doi.org/10.1140/epja/i2014-14017-x>
163. J.M. Lattimer, M. Prakash, *The Astrophysical Journal* **550**(1), 426 (2001). DOI [10.1086/319702](https://doi.org/10.1086/319702). URL <https://doi.org/10.1086/319702>
164. J. Hu, S. Bao, Y. Zhang, K. Nakazato, K. Sumiyoshi, H. Shen, *PTEP* **2020**(4), 043D01 (2020). DOI [10.1093/ptep/ptaa016](https://doi.org/10.1093/ptep/ptaa016)
165. T. Malik, B.K. Agrawal, C. Providência, J.N. De, *Phys. Rev. C* **102**(5), 052801 (2020). DOI [10.1103/PhysRevC.102.052801](https://doi.org/10.1103/PhysRevC.102.052801)
166. B.A. Li, M. Magno, *Phys. Rev. C* **102**(4), 045807 (2020). DOI [10.1103/PhysRevC.102.045807](https://doi.org/10.1103/PhysRevC.102.045807)
167. M. Fortin, A.R. Raduta, S. Avancini, C. Providência, *Phys. Rev. D* **103**(8), 083004 (2021). DOI [10.1103/PhysRevD.103.083004](https://doi.org/10.1103/PhysRevD.103.083004)
168. B.A. Li, B.J. Cai, L.W. Chen, J. Xu, *Prog. Part. Nucl. Phys.* **99**, 29 (2018). DOI [10.1016/j.pnpnp.2018.01.001](https://doi.org/10.1016/j.pnpnp.2018.01.001)
169. M. Jaminon, C. Mahaux, *Phys. Rev. C* **40**, 354 (1989). DOI [10.1103/PhysRevC.40.354](https://doi.org/10.1103/PhysRevC.40.354). URL <https://link.aps.org/doi/10.1103/PhysRevC.40.354>
170. F. Sammarruca, W. Barredo, P. Krastev, *Phys. Rev. C* **71**, 064306 (2005). DOI [10.1103/PhysRevC.71.064306](https://doi.org/10.1103/PhysRevC.71.064306). URL <https://link.aps.org/doi/10.1103/PhysRevC.71.064306>
171. E.N.E.v. Dalen, C. Fuchs, A. Faessler, *Phys. Rev. C* **72**, 065803 (2005). DOI [10.1103/PhysRevC.72.065803](https://doi.org/10.1103/PhysRevC.72.065803). URL <https://link.aps.org/doi/10.1103/PhysRevC.72.065803>
172. M. Baldo, G.F. Burgio, H.J. Schulze, G. Taranto, *Phys. Rev. C* **89**, 048801 (2014). DOI [10.1103/PhysRevC.89.048801](https://doi.org/10.1103/PhysRevC.89.048801). URL <https://link.aps.org/doi/10.1103/PhysRevC.89.048801>
173. X.L. Shang, A. Li, Z.Q. Miao, G.F. Burgio, H.J. Schulze, *Phys. Rev. C* **101**, 065801 (2020). DOI [10.1103/PhysRevC.101.065801](https://doi.org/10.1103/PhysRevC.101.065801). URL <https://link.aps.org/doi/10.1103/PhysRevC.101.065801>
174. L.W. Chen, C.M. Ko, B.A. Li, *Phys. Rev. C* **76**, 054316 (2007). DOI [10.1103/PhysRevC.76.054316](https://doi.org/10.1103/PhysRevC.76.054316). URL <https://link.aps.org/doi/10.1103/PhysRevC.76.054316>
175. R. Somasundaram, C. Drischler, I. Tews, J. Margueron, *Phys. Rev. C* **103**, 045803 (2021). DOI [10.1103/PhysRevC.103.045803](https://doi.org/10.1103/PhysRevC.103.045803). URL <https://link.aps.org/doi/10.1103/PhysRevC.103.045803>
176. J. Chen, J. Clark, R. Davé, V. Khodel, *Nuclear Physics A* **555**(1), 59 (1993). DOI [https://doi.org/10.1016/0375-9474\(93\)90314-N](https://doi.org/10.1016/0375-9474(93)90314-N). URL <https://www.sciencedirect.com/science/article/pii/S037594749390314N>
177. D.G. Yakovlev, A.D. Kaminker, O.Y. Gnedin, P. Haensel, *Phys. Rept.* **354**, 1 (2001). DOI [10.1016/S0370-1573\(00\)00131-9](https://doi.org/10.1016/S0370-1573(00)00131-9)
178. D.A. Baiko, P. Haensel, D.G. Yakovlev, *Astronomy & Astrophysics* **374**(1), 151 (2001). DOI [10.1051/0004-6361:20010621](https://doi.org/10.1051/0004-6361:20010621). URL <https://doi.org/10.1051/0004-6361:20010621>
179. D.G. Yakovlev, C. Pethick, *Annual Review of Astronomy and Astrophysics* **42**(1), 169 (2004). DOI [10.1146/annurev.astro.42.053102.134013](https://doi.org/10.1146/annurev.astro.42.053102.134013). URL <https://doi.org/10.1146/annurev.astro.42.053102.134013>
180. C.A. Raithel, F. Ozel, D. Psaltis, *Astrophys. J.* **875**(1), 12 (2019). DOI [10.3847/1538-4357/ab08ea](https://doi.org/10.3847/1538-4357/ab08ea)
181. A. Carbone, A. Schwenk, *Phys. Rev. C* **100**, 025805 (2019). DOI [10.1103/PhysRevC.100.025805](https://doi.org/10.1103/PhysRevC.100.025805). URL <https://link.aps.org/doi/10.1103/PhysRevC.100.025805>
182. C. Ducoin, P. Chomaz, F. Gulminelli, *Nucl. Phys. A* **789**, 403 (2007). DOI [10.1016/j.nuclphysa.2007.03.006](https://doi.org/10.1016/j.nuclphysa.2007.03.006)
183. T. Fischer, N.U. Bastian, D. Blaschke, M. Cierniak, M. Hempel, T. Klähn, G. Martínez-Pinedo, W.G. Newton, G. Röpke, S. Typel, *Publ. Astron. Soc. Austral.* **34**, 67 (2017). DOI [10.1017/pasa.2017.63](https://doi.org/10.1017/pasa.2017.63)
184. A. Yudin, M. Hempel, S. Blinnikov, D. Nadyozhin, I. Panov, *Mon. Not. Roy. Astron. Soc.* **483**(4), 5426 (2019). DOI [10.1093/mnras/sty3468](https://doi.org/10.1093/mnras/sty3468)
185. A.R. Raduta, F. Gulminelli, M. Oertel, *Phys. Rev. C* **93**(2), 025803 (2016). DOI [10.1103/PhysRevC.93.025803](https://doi.org/10.1103/PhysRevC.93.025803)
186. A. Juodagalvis, K. Langanke, W. Hix, G. Martínez-Pinedo, J. Sampaio, *Nuclear Physics A* **848**(3), 454 (2010). DOI [10.1016/j.nuclphysa.2010.09.012](https://doi.org/10.1016/j.nuclphysa.2010.09.012). URL <https://www.sciencedirect.com/science/article/pii/S0375947410009012>
187. J. Lattimer, C. Pethick, D. Ravenhall, D. Lamb, *Nuclear Physics A* **432**(3), 646 (1985). DOI [10.1016/0375-9474\(85\)90006-5](https://doi.org/10.1016/0375-9474(85)90006-5). URL <https://www.sciencedirect.com/science/article/pii/S0375947485900065>
188. M. Terasawa, K. Sumiyoshi, T. Kajino, I. Tanihata, G.J. Mathews, K. Langanke, *Nucl. Phys. A* **688**, 581 (2001). DOI [10.1016/S0375-9474\(01\)00795-3](https://doi.org/10.1016/S0375-9474(01)00795-3)
189. A. Arcones, G. Martínez-Pinedo, E. O'Connor, A. Schwenk, H.T. Janka, C.J. Horowitz, K. Langanke, *Phys. Rev. C* **78**, 015806 (2008). DOI [10.1103/PhysRevC.78.015806](https://doi.org/10.1103/PhysRevC.78.015806)
190. L. Ou, Z. Li, Y. Zhang, M. Liu, *Phys. Lett. B* **697**, 246 (2011). DOI [10.1016/j.physletb.2011.01.062](https://doi.org/10.1016/j.physletb.2011.01.062)
191. L.F. Roberts, S. Reddy, G. Shen, *Phys. Rev. C* **86**(6), 065803 (2012). DOI [10.1103/PhysRevC.86.065803](https://doi.org/10.1103/PhysRevC.86.065803)
192. K. Nakazato, H. Suzuki, *Astrophys. J.* **878**(1), 25 (2019). DOI [10.3847/1538-4357/ab1d4b](https://doi.org/10.3847/1538-4357/ab1d4b)
193. A. Pascal. Modélisation de l'évolution d'une proto-étoile à neutrons. Thèse de doctorat à l'Université Paris Sciences et Lettres (2021)
194. E.R. Most, C.A. Raithel, arXiv e-prints arXiv:2107.06804 (2021)
195. M. Prakash, I. Bombaci, M. Prakash, P.J. Ellis, J.M. Lattimer, R. Knorren, *Phys. Rep.* **280**(1), 1 (1997). DOI [10.1016/S0370-1573\(96\)00023-3](https://doi.org/10.1016/S0370-1573(96)00023-3). URL <http://www.sciencedirect.com/science/article/pii/S0370157396000233>
196. L. Villain, J.A. Pons, P. Cerda-Duran, E.ourgoulhon, *Astron. Astrophys.* **418**, 283 (2004). DOI [10.1051/0004-6361:20035619](https://doi.org/10.1051/0004-6361:20035619)
197. L.F. Roberts, *Astrophys. J.* **755**, 126 (2012). DOI [10.1088/0004-637X/755/2/126](https://doi.org/10.1088/0004-637X/755/2/126)
198. K. Sumiyoshi, J.M. Ibáñez, J.V. Romero, *Astron. Astrophys. Suppl. Ser.* **134**(1), 39 (1999). DOI [10.1051/aas:1999123](https://doi.org/10.1051/aas:1999123). URL <https://doi.org/10.1051/aas:1999123>
199. K. Strobel, C. Schaab, M.K. Weigel, *Astron. Astrophys.* **350**, 497 (1999)
200. O.E. Nicotra, M. Baldo, G.F. Burgio, H.J. Schulze, *Phys. Rev. D* **74**, 123001 (2006). DOI [10.1103/PhysRevD.74.123001](https://doi.org/10.1103/PhysRevD.74.123001)
201. A. Li, X.R. Zhou, G.F. Burgio, H.J. Schulze, *Phys. Rev. C* **81**, 025803 (2010). DOI [10.1103/PhysRevC.81.025803](https://doi.org/10.1103/PhysRevC.81.025803)
202. G.F. Burgio, H.J. Schulze, *Astron. Astrophys.* **518**, A17 (2010). DOI [10.1051/0004-6361/201014308](https://doi.org/10.1051/0004-6361/201014308)

203. G. Martinon, A. Maselli, L. Gualtieri, V. Ferrari, *Phys. Rev. D* **90**, 064026 (2014). DOI 10.1103/PhysRevD.90.064026. URL <https://link.aps.org/doi/10.1103/PhysRevD.90.064026>
204. G. Camelió, L. Gualtieri, J.A. Pons, V. Ferrari, *Phys. Rev. D* **94**(2), 024008 (2016). DOI 10.1103/PhysRevD.94.024008
205. J.J. Lu, Z.H. Li, G.F. Burgio, A. Figura, H.J. Schulze, *Phys. Rev. C* **100**, 054335 (2019). DOI 10.1103/PhysRevC.100.054335. URL <https://link.aps.org/doi/10.1103/PhysRevC.100.054335>
206. J. Roark, X. Du, C. Constantinou, V. Dexheimer, A.W. Steiner, J.R. Stone, *Monthly Notices of the Royal Astronomical Society* **486**(4), 5441 (2019). DOI 10.1093/mnras/stz1240. URL <https://doi.org/10.1093/mnras/stz1240>
207. S.S. Lenka, P. Char, S. Banik, *Journal of Physics G: Nuclear and Particle Physics* **46**(10), 105201 (2019). DOI 10.1088/1361-6471/ab36a2
208. K.P. Nunna, S. Banik, D. Chatterjee, *Astrophys. J.* **896**(2), 109 (2020). DOI 10.3847/1538-4357/ab8f2c
209. A.R. Raduta, M. Oertel, A. Sedrakian, *Mon. Not. Roy. Astron. Soc.* **499**(1), 914 (2020). DOI 10.1093/mnras/staa2491
210. I. Bombaci, *Astronomy and Astrophysics* **305**, 871 (1996)